Dust In The Galaxy

Investigation Of The X-ray Halo Around GRB 031203
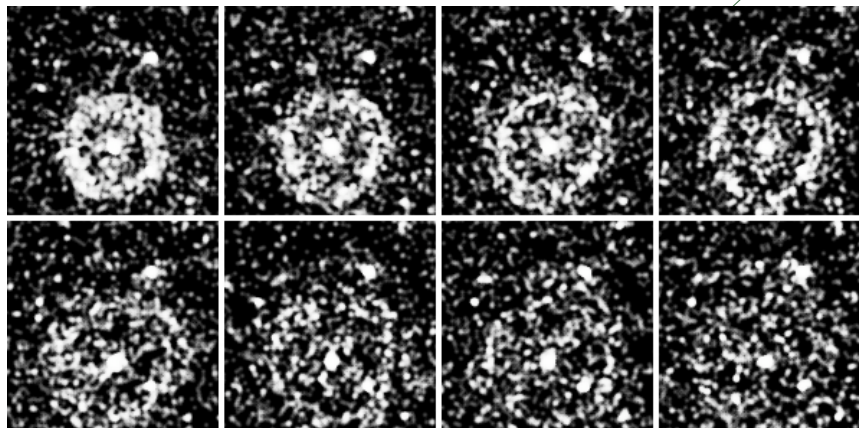
Master Thesis

by

Rosina Pisecka Hein Bertelsen

Dark Cosmology Centre

Niels Bohr Institute

Copenhagen University

4th November 2009

Supervisor: Darach Watson

Co-supervisor: Anja C. Andersen

Abstract

In this master thesis dust in the Galaxy is explored.

This is done by the analysis of XMM-Newton observations of the X-ray afterglow of GRB 031203, which reveals a time evolving halo around the afterglow. The evolving halo is believed to be caused by the scattering of the X-ray emission from the afterglow off dust resident in our own Galaxy. By the analysis of the halo light, information about the dust causing the scattering is revealed.

For the analysis the XMM-Newton SAS package and the XSPEC programme are used.

The analysis reveals that the halo actually consists of two rings, presumably caused by two individual dust slabs. By the use of different methods, through the analysis, I find results firmly substantiating the claim that the halo light is in fact caused by the scattering, of the afterglow emission, off dust. I find that the two dust slabs are located at $\approx 870\ pc$ and $\approx 1400\ pc$. The results are confirmed through the use of different methods. I find that the dust slabs are two thin sheets of dust. The two sheets can be expected to be part of the GUM Nebula, which is within the line of sight to the GRB.

Through analysis of the spectral data an absorbing column of $n_H \approx 8 - 9 \cdot 10^{21}\ cm^{-2}$ is found for the line of sight to the GRB. This is significantly above the galactic value in that direction, and the residual can be expected to be caused by absorption in the host galaxy of the GRB. Photon indices for the afterglow and halo respectively are found to be $\Gamma \approx 2$ and $\Gamma \approx 3$, revealing that the halo spectrum is significantly steeper than the afterglow spectrum.

Acknowledgement

Contents

1. Introduction

1.1. Project description

In between the stars in our Galaxy there are large regions filled with dust. This dust is usually from the size of several molecules (≈ 50) up to several microns. This dust is important to study for several reasons; for example it is important for the formation process of stars and planets.

When observing the sky the dust mostly acts to obscure the light coming to us from distant stars and galaxies. Optical light for example will be obscured. But if the lightwaves are shorter, as for example X-ray light which has a wavelength of 0.01-10 nm (energy range of 0.12-120 keV), the light will be scattered at small angles when travelling through dust. When light from a distant X-ray source (for example a gamma-ray burst) travels through dust slabs it can by scattering result in an X-ray halo around the source. From the radial density distribution of this halo it is possible to get the properties and location of the dust.

In this project investigations of the dust in the Galaxy will be done by the use of X-ray data from the X-ray Multi Mirror Mission; XMM-Newton. It holds three X-ray telescopes and uses three European Photon Imaging Cameras (EPIC) which are sensitive over the energy range 0.15-15 keV. Since the Earth's atmosphere blocks out all X-rays, the telescopes are placed in space.

Through this thesis X-ray data of the afterglow from the gamma-ray burst GRB 031203 will be retrieved from the XMM-Newton Science Archive. This data reveals a dust scattered X-ray halo around the afterglow. The data will be analysed using the XMM-Newton Science Analysis System (SAS). SAS is a software package developed especially for the analysis of data from the XMM-Newton mission. Also parts of the HEAsoft package, developed by NASA, is used. This analysis will reveal details of the scattering dust slabs.

1.2. Cosmic Dust

Cosmic dust is small grains composed of tiny solid particles, with sizes ranging from about a hundred molecules to 0.01 mm in size. Dust is mostly found within galaxies but does have a wide range of environments. Dust can for example be found in comets, around stars, in galactic nuclei or in large molecular clouds. Since dust is not luminous we do not observe it directly with optical telescopes but only through the effects it has on the visual light or movement of luminous objects.

As astronomy has developed, the role of cosmic dust has changed through time. Once dust was merely considered something that obscured or blocked our view when doing observations. Dust was only investigated superficially in the amount needed for calculating the extinction[1], and otherwise not really considered.

Today the importance of studying dust for its own sake has become evident. Exploration of dust was first truly embarked on with the Hubble Space Telescope, since infrared light, which is what dust emits, is heavily absorbed by the atmosphere of the Earth.

1.2.1. Importance of Dust

Dust is a vital ingredient in our universe as we know it. Without it our universe would be dark and dull, since dust participates in the creation of almost anything we see on the night sky. Thereby dust is on several accounts important for our existence in the universe. First of all the formation of the stars take place in large gas and dust clouds and it seems that the presence of dust may act to catalyse the collapse of proto-stars (Whittet 1992). During this formation proto-planetary disks of dust may also result in a planetary system forming instead of just a lonely star. Dust grains may also be responsible for driving the outflows in stars that leads to mass-loss which may ultimately determine the fate of a star during the late evolution. These outflows contribute to the enrichment of heavier elements to the interstellar me-

---

[1] The term extinction covers the collected effect of absorption of light and scattering of light.

dium (ISM). The heavier elements are important for the diversity in planets and the emergence of biology. So in trying to understand our universe better, exploring the nature of dust is a necessary part.

1.2.2. Correcting for Dust

Off course it is still also very important to know dust better in order to correct our observations better. There can be a very large diversity in distribution and geometry of dust. This means that a general correction for extinction may not always suffice. This is especially relevant when looking at distant galaxies. Therefore it can be a huge advantage knowing more specifically where dust in our Galaxy is located, as in, where do we have larger concentrations of dust than average and what is the extinction when looking in this particular direction? Of course when looking in the directions within the galactic disk the probability of dust being in the line of sight is larger than when looking perpendicularly to the disk out of the Galaxy.

Today great efforts are put towards mapping the dust in our Galaxy, but there is still much to explore. By now we have locations for many large dust clouds in our Galaxy. These are obtained either from infrared observations of the emission from the dust or from observations of the scattering of other light sources by the dust. The dust in our Galaxy is mainly confined to the disk, and the concentration is greater towards the centre, especially when approaching star formation areas.

The term, dust grains, covers a wide range of species and compositions, it is not well known what dust is made of, although most of the dust in the universe is expected to be of carbonaceous or silicate species. This is based on the known abundance of elements in the universe and which of these can actually condense to dust.

1.2.3. Formation of Dust

The research on how dust is created is still an unclosed chapter. Today a general outline of the mechanism exists, but the details are still un-

certain. When stars reach their final stages they may exhibit mass loss. This mass loss happens mostly in cool high luminosity stars, red giants, super giants and particularly AGB (asymptotic giant branch) stars. In the stellar winds the conditions are right for the slow build up that the formation of dust requires. The formation process involves the formation of small stable molecule clusters which then grow to macroscopic sizes. In these stellar outflows, matter which is initially hot expands and cools on the way out. Going outward the atoms grow to molecules and then finally, at distances where the temperature is well below 1500 K, the atoms and molecules combine to clusters that grow to dust grains. The formation process requires time-scales slow enough for the clusters to build up before the atoms are too far apart. This fact makes the stellar winds an ideal place for dust formation. Another dust formation sight may be supernovae (SNe).

1.2.4. Dust - Light Interaction

How dust interacts with radiation depends on the cross-section of the grains and the wavelength of the light. The dust causes extinction, by either scattering or absorbing the interacting light. Having established that examining dust is necessary, finding that there seems to be dust lying between an object on the sky and our eyes can be a positive thing. This gives us the opportunity to analyse the geometry and nature of the dust lying in the way, of course depending on how much we know about the original light source. When the light is absorbed the observations will not reveal anything in particular about the dust, besides maybe the fact that it is there. If we, on the other hand, look in the infrared energy range we will see the presence of the dust. This happens because the dust is heated by the photons being absorbed, causing the dust to emit blackbody radiation. When looking for example at optical images of the Galaxy, see Figure 1, the areas in the mid region of the disk appear dark. Looking instead at the same image in the infrared we see the areas appearing dark in optical images, instead looking bright from

the emission by dust which has absorbed the optical light. The infrared emission gives the observer an opportunity to explore the spectrum of the dust. The spectrum will have absorption-lines revealing some of the elements in the dust.
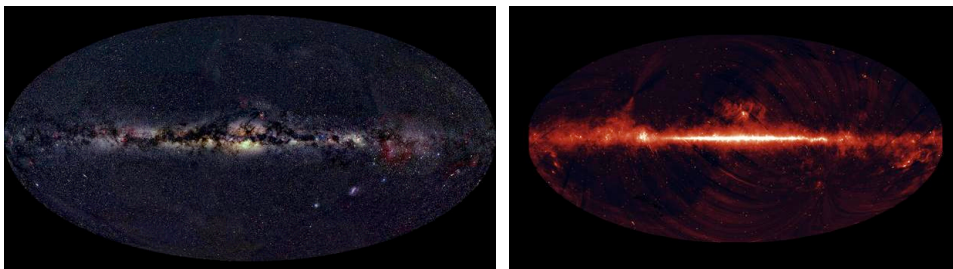
Figure 1. Right; optical image of the Milky Way, from COSMOS (2009), left; infrared image of the Milky Way, from Newscientist (2009). The dusty parts of the Galaxy that are dark and unseen in the optical image, shows up in the infrared.

If the object emits light of X-ray wavelengths the light might be scattered in a haze around the object, see Figure 2. This happens through grazing incidents, and will be discussed in Section 2.1. From looking at the spectra it will be possible to deduce a grain size and possibly a composition. If the object has some evolution in time it is even better. For a fading object the result will be an evolving ring instead of a haze, and we can derive the distance and size of the dust medium blocking our view, see Section 2.3. The only real time evolving X-ray sources known at this point are the fading X-ray afterglows of gamma-ray bursts (GRBs) and X-ray repeaters. The fact that X-ray afterglows appear where no actual X-ray source was present before, and then fade and disappear, make them a uniquely valuable tool in dust exploration. This is still a very new discovery, so not many GRB afterglow halos have yet been discovered and explored, see Section 1.7. It is only with more recent X-ray telescopes; XMM-Newton, Swift, Integral and Chandra, see Section 1.4 that long observations of X-ray afterglows starting shortly after the GRB itself, has become available. Of course the GRBs themselves are still a fairly new topic, which has not yet been fully uncovered. The first sign of GRBs was observed accidentally in 1967 by the American Vela satellites (Hjorth et al. 2005).
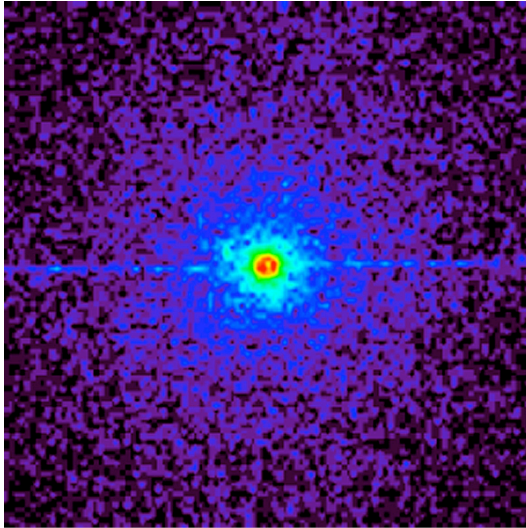
Figure 2. Chandra-image of the scattered X-ray halo around Cygnus X-3, from NASA's home page (2009a).

1.3. Gamma-Ray Bursts

A gamma-ray burst is defined as a highly luminous flash of gamma rays usually residing in distant galaxies. In fact they are the most luminous types of objects on the sky. If an event like this was to take place in our own Galaxy the effects would be devastating (Hjorth et al. 2005). The bursts can last from milliseconds to just under one hour. The GRB is associated with an afterglow, emitting light of X-ray, optical and radio frequencies, for some time after the burst itself. The X-ray emission is the first and most luminous part of the afterglow which is believed to begin already during the GRB itself. It lasts from a few hours to a few days and is the shortest part of the afterglow. The last parts of the afterglow is characterised by optical emission and then radio emission[2]. It is believed that these afterglow emissions can be extrapolated back in time to the GRB event itself, so that prompt emission also exists in the X-ray, optical and radio energy range (Piran 2004).

A GRB is named according to the date that we see it on our night sky; GRB yymmdd. If more than one GRB is seen in one day, they get letters attached to the name according to the order they appear: a, b, c and so on.

---

[2] The radio emission can in some cases last up to several years.

At first the GRB phenomenon was a mystery. Not expecting a distant source to be this luminous they were assumed to take place in our own Galaxy. The fact that GRBs are rather uniformly distributed on the sky revealed that they were not events taking place in our own Galaxy,[3] but much farther from our location in the universe.

Gamma-ray bursts can be divided into two subgroups according to the duration of the burst. A group of long bursts with a T90[4] duration over 2 seconds and a group of short bursts with T90 less than 2 seconds (Piran 2004). The long bursts seem to be most frequent.
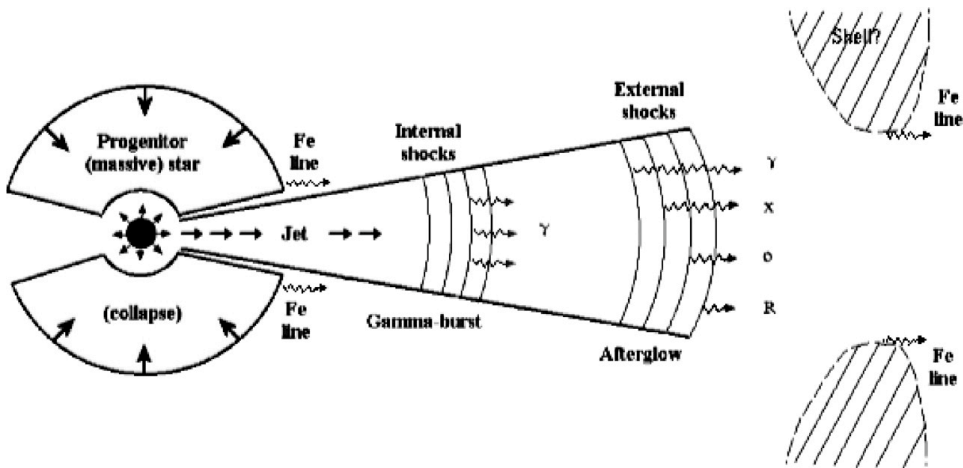
Figure 3. Image taken from Mészáros (2002), showing a schematic view of the burst mechanism. The GRB itself is caused by internal shocks, whereas the afterglow is caused by external shocks.

1.3.1. Precursors

The origin of the bursts are still uncertain but for the long bursts the current accepted theory is that they are connected to the death of massive stars, linking the GRBs to a rare group of SNe. The burst occurs when energy is transported via jets in the direction of our line

---

[3] Since the Galaxy is not uniform but has a disk with larger concentration of stars, events taking place in our own Galaxy should have a higher concentration in the disk. This would mean that the events should be concentrated towards a specific region of the sky.

[4] The T90 duration is defined as the time interval during which 90% of the background subtracted counts are observed, starting when 5% of the background subtracted counts are observed (Piran 2004).

of sight (Piran 2004). See Figure 3, for a schematic view of the burst. This explains why the GRBs are so luminous; huge amounts of energy is focused in beams. If it were not for the fact that they are so luminous, meaning that we can see them across huge distances, they would probably be rare because the beam has to be within our line of sight in order for us to observe the GRB. The furthest known GRB so far, GRB 090423, was found at a redshift of $z = 8.2$ (Tanvir et al. 2009). The closest so far was found at $z = 0.0085$, corresponding to a distance of $\approx 35\ Mpc$, still very far from our Galaxy (Tinney et al. 1998).

For the short bursts one proposed origin is the merging of two neutron stars.

If the bursts are in fact beamed then the total amount of energy released is of the order $\approx 10^{51} ergs$. This size of energy release, in the short time-scale that a GRB spans, must involve a compact object. This supports the link to star death.

1.3.2. Burst Mechanism

The currently accepted theory explaining GRBs is called the fireball model (Piran 2004). This model agrees overall with observations. According to the model GRBs are caused by the release of an enormous amount of energy into a small volume. The burst itself arises when the kinetic energy in ultra-relativistic flows are dissipated internally by collisions of the material within the flows. The afterglow arises when the flow is slowed down by external shocks; collisions with the surrounding matter. This means that the afterglow flux can not be extrapolated back to fit the GRB flux, since the two emissions are caused by different effects. On the other hand it can be extrapolated back to begin immediately after the burst itself as a separate prompt emission, as mentioned above. The non-connection between the burst itself and the afterglow is confirmed by observations.

Synchrotron radiation is proposed as an engine for both the GRB and the afterglow, although only the afterglow connection has been suitably

supported by observations (Piran 2004). Synchrotron radiation is connected to electrons moving with relativistic speeds, spiralling around a magnetic field[5], see Figure 4. The electrons radiate photons with an energy governed by the radius of the circle. The energies are commonly in the radio regime but can expand to X-ray and beyond, for example in a highly energetic blast like a gamma-ray burst. A synchrotron spectrum typically has a power-law shape, due to the fact that the particle energies have power-law distribution (NASA 2009).
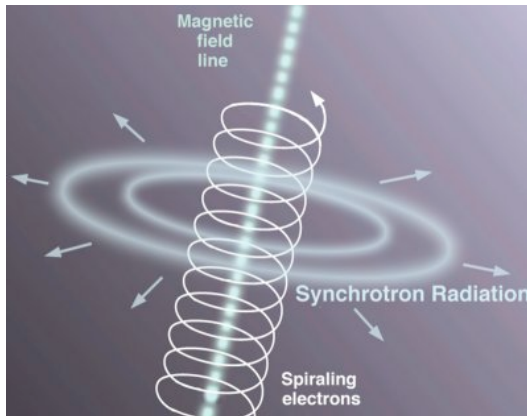
Figure 4. Schematic image showing electrons moving in a magnetic field causing them to emit synchrotron radiation, from Astronomyonline (2009).

For the case of the afterglow, the material ejected by the GRB is pushed through surrounding interstellar medium, where it collides with gas and dust. This collision causes the electrons in the medium to be accelerated to the above mentioned relativistic energies. The energy of these electrons will then have a power-law distribution ; $N(E) \propto E^{-p}$ (van Paradijs, J. and Bleeker, J. A. M. 1999) where $N(E)$ is the number of photons at the energy E and p is the powerlaw index. This means that the radiation from these electrons and thereby the afterglow spectra and light curve, will also have a power-law distribution.

1.3.3. GRB Hosts

The hosts of the GRBs are distant galaxies. Because of the linking of GRBs to stellar deaths, a proportionality between star formation rate and GRB rate is expected and is consistent with the observed peak flux

---

[5] The non-relativistic equivalent is called cyclotron radiation.

distribution of GRBs. A number of hosts have been identified and they all share the common feature that they seem to be bluer than average, implying that they contain an abundant number of young stars. Also, the star formation rate per unit luminosity in these galaxies has been shown to be quite substantial. So GRBs do seem to occur where massive stars are born and die, in actively star forming galaxies (van Paradijs et al. 2000).

1.4. X-rays - Use and Detection

X-rays cover an energy range, from soft X-rays $0.12 - 12keV$, to hard X-rays $12 - 120keV$. Looking at the electromagnetic spectrum they are located in the higher energy end, just above optical and UV light and just below gamma rays. In everyday life, X-rays are widely used in medicine, when the bones in our bodies are photographed by use of X-rays. This can be done because X-rays are energetic enough to penetrate the skin and muscles of our bodies but not the harder bones.

The atmosphere of our planet is not very dense but is about 100-120 km wide. This means that the effect on an X-ray photon moving through it would be comparable to that of moving through 5 meters of concrete (Chandra's home page 2009). This means that all X-rays are effectively prevented from reaching the surface of the Earth; fortunate for our health but unfortunate for X-ray astronomers, since this means that any good X-ray observations have to be moved outside, or to the outer regions of the atmosphere. This fact caused X-ray astronomy to have a rather slow start, since astronomers had to wait for the development of technology. Another fact that has slowed down the development of X-ray astronomy is the difficulties in the engineering of the optics necessary (van Paradijs, J. and Bleeker, J. A. M. 1999). X-ray telescopes require much more complicated engineering than optical telescopes do.

The first astronomical X-ray source detected was actually by coincidence. It was accidentally scanned during the flight of a sounding rocket

in 1962[6]. In the first observational era of X-ray astronomy, 1962-1970, the observations were done from rockets or balloons, moving to heights where the destructive earth atmosphere was thinner. This put constraints on the observation times and it was not until 1970 where the first successful X-ray satellite, Uhuru, was launched that the X-ray sky could be efficiently explored. The Uhuru mission resulted in the first all sky survey, where 339 sources of 2-6 keV were located, most being 10.000 times fainter than Sco X-1.

The instruments on these satellites were only detectors and did not produce images since there were no real focusing. They only gave an approximate position on the sky. The first satellite-borne imaging X-ray telescope was on board the Einstein Observatory, launched in 1978. After two and a half years of orbiting it had revealed several thousand X-ray sources. The resolution of Einstein was 2" over a field of view (FOV) of 1° (G. W. Fraser 1989).

Today huge improvements have been reached for the field of X-ray astronomy. The present day orbiting X-ray telescopes include XMM-Newton (1999), Chandra (1999), Integral (1995) and SWIFT (2004). These provide better resolution and larger FOVs and are adapted for different purposes. Chandra has a very high sensitivity, 0.5" spatial resolution, but a not so large FOV. XMM on the other hand has greater collecting area but less resolution, for specifications see Section 1.5. The two satellites SWIFT and Integral are especially designed for GRB observations, so they cover much more than just X-ray energies.

The ability X-rays have, to be scattered off dust by grazing incidents, elaborated in Section 2.1, provides us with a very practical tool. We get the opportunity to indirectly observe the dust which is otherwise invisible to us. This, among other light-dust interaction effects, has lead to the mapping of a large fraction of the dust in our Galaxy, as described in Section 1.2. Because of this, when doing observations in for example the optical range, where we loose a lot of light because of absorption by dust, we can properly correct our observational data.

---

[6] The source was named Sco X-1 since it was located in the constellation of Scorpius.

1.5. The XMM-Newton Satellite

XMM stands for X-ray Multi-Mirror, since the satellite's three telescopes each have 58 mirrors. The XMM-Newton satellite was launched by ESA in 1999, into a highly elliptical orbit, displayed in Figure 6, see Figure 5 for an image of the satellite. The purpose of the satellite was to detect and study celestial X-ray sources from space, outside the X-ray shielded environment caused by the Earth-atmosphere. It carries three high throughput X-ray telescopes and an optical monitor. The telescopes are equipped with three EPIC, European Photon Imaging Cameras, and two RGS, Reflection Grating Spectrometers. The data used in this thesis are from the EPIC cameras.

Figure 5. Image of the XMM-Newton satellite taken from the XMM home page.

The EPIC cameras consist of two MOS, Metal Oxide Semi-conductor CCD arrays, these receive light from the telescopes where the light is also diverted to the RGS detectors, so only $\approx 44\%$ of the incoming flux reaches the MOS cameras. Besides the two MOS cameras there is also one PN camera, which receives an unobstructed beam from the last
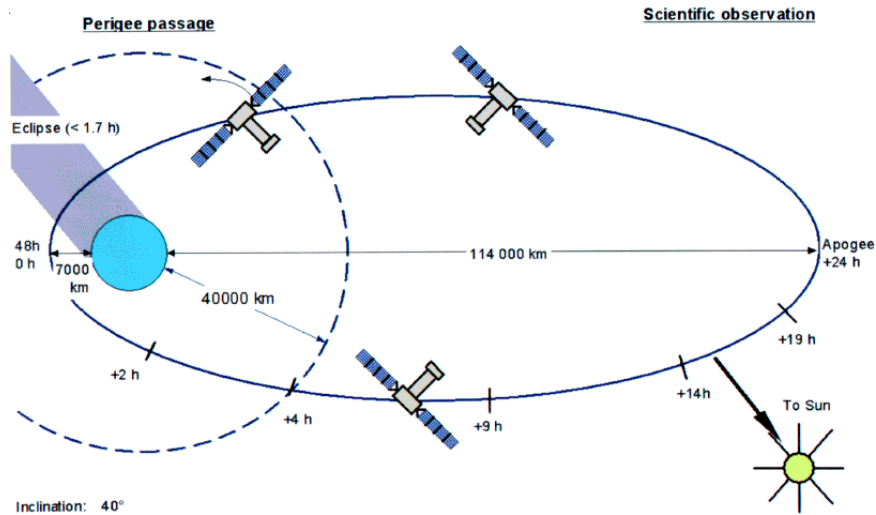
Figure 6. The orbit of the XMM-satellite, image taken from NASA's home page (2009b).

X-ray telescope. The PN camera relies on p-n junctions. These EPIC cameras provide the means to perform extremely sensitive imaging observations.

The cameras have a field of view of 30', in the energy range 0.15 keV to 15 keV, and a point spread function for the PN of 6", FWHM, and for the MOS of 5", FWHM. They operate in photon counting mode and produce event lists. An event list is a table with one entry line per received photon count, listing the associated properties. This includes the position, the arrival time and the energy connected to the event. The two camera types on board the XMM are fundamentally different and follow different concepts (The XMM Home Page 2009). The geometry of the CCDs are different, see Figure 7. The net effective area of the telescope mirrors depend on the energy of the incoming light. This dependency is slightly different for the the two cameras, PN and MOS (see the plot of net effective area versus energy in Figure 8). For the MOS the usable energy range is 200-12000 eV, whereas for the PN it is 200-15000 eV. The pixel sizes are 4.1" for the PN and 1.1" for the MOS. The PN camera has an equivalent angular resolving capability for a single photon of 3.3".

Comparison of focal plane organisation of EPIC MOS and pn cameras

30 arc min
diameter circles

EPIC MOS
7 CCDs each 10.9 x 10.9 arcminutes

EPIC pn
12 CCDs each 13.6 x 4.4 arcmin
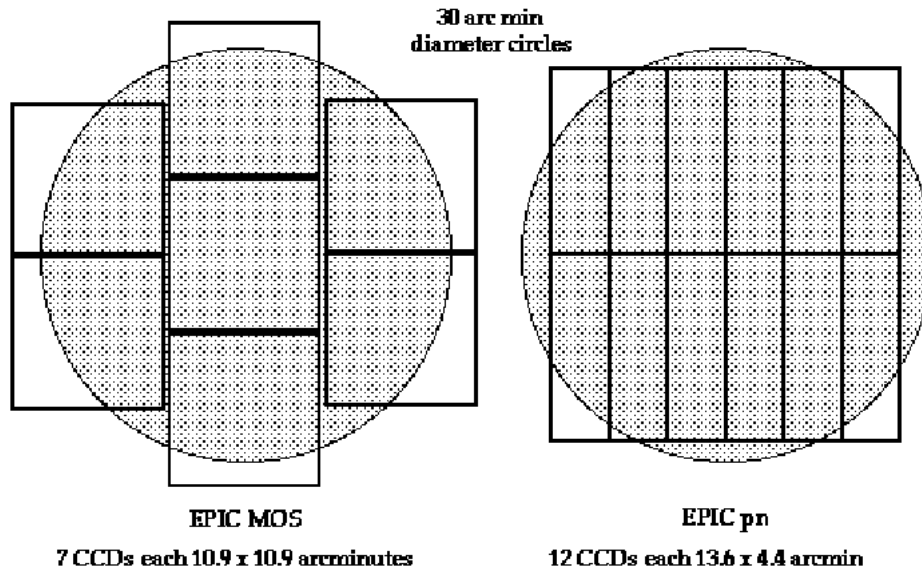
Figure 7. Image, taken from XMM-Newton Users' Handbook (2003), displaying the ccd-layout of the two camera types aboard XMM. The two MOS-type cameras are the same but rotated 90°, relative to each other. The gaps on the MOS geometry are not actual gaps, the MOS CCDs overlap each other so that one CCD is placed slightly behind the other.

The instruments can be used in imaging, timing or burst mode. The data used in this thesis is in imaging mode. The data from the XMM observations are arranged in Observation Data Files, ODF. These can not immediately be used for analysis but has to be calibrated first. The files necessary for the calibrations are provided with the ODF. For the calibration and the scientific analysis the software package, SAS, is available.

1.6. SAS and Other Computational Tools

The XMM-Newton Science Analysis System, SAS, is a package of tasks, scripts and libraries, designed specifically for the preparation and analysis of the observational products from the XMM-Newton satellite. The capabilities of SAS involve both the calibration and the following scientific analysis. There are SAS tasks to produce the calibrated event files which can be used for the scientific analysis. The scientific
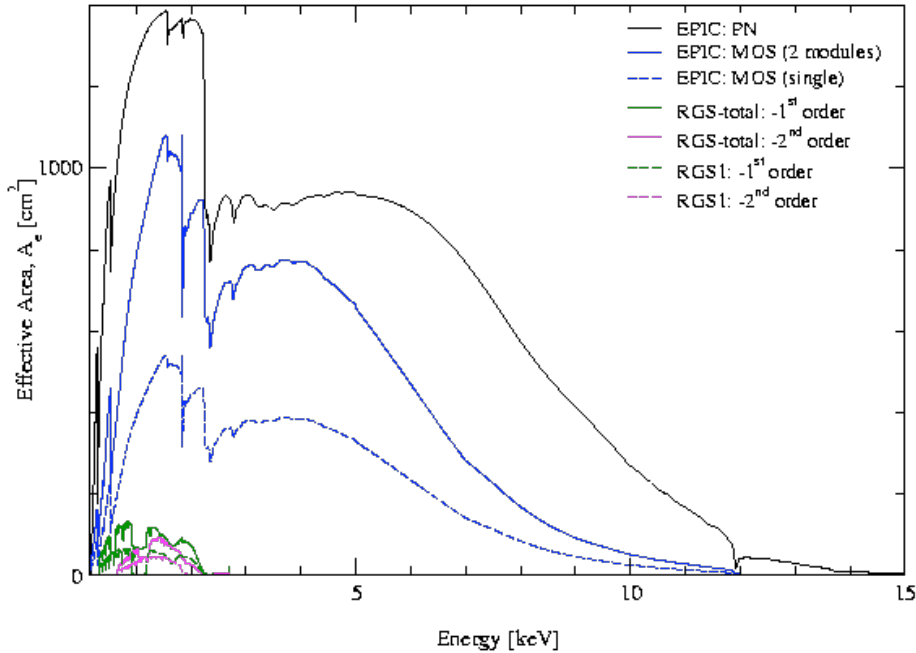
Figure 8. The net effective area of the XMM-telescope mirrors combined with the response characteristics of the instruments, taken from the XMM-Newton Users' Handbook (2003).

analysis possible with SAS, includes the extraction of images, light curves, spectra, histograms and instrument response matrices. All the SAS products are compatible with the most commonly used analysis packages. The SAS package does not include tools for spectral analysis. Here the XSPEC software was used. Some, for this analysis advantageous tasks, were also not available in the SAS package and the FTOOLS software were therefore also used in the analysis. FTOOLS is a general package of software, developed by NASA, to manipulate fits files. For writing scripts, with more particular model fitting or more advanced binning, the IDL programming language was used. The scripts I produced for this thesis can be seen in Appendix A.

For the calibration of the ODF, the SAS tasks *emproc* and *epproc* were used. These tasks produce calibrated photon event files for the

MOS and the PN cameras respectively, by processing the contents of the ODF.

For the extraction of images, spectra, light curves and simply filtering event lists the SAS task *evselect* can be used. When using this task one chooses which type of products the outcome should be, by setting either; *withimageset*, *withrateset*, *withspectrumset* or *withfilteredset = yes*. One can then, by setting the relevant parameters belonging to this task, choose the columns, the binning, the ranges and the filtering, to be used. The first thing to do after the calibration by the tasks, *emproc* and *epproc*, should be to clean up the raw data by filtering it. The filtering can involve restricting the pattern values used, setting the flag values, limiting the energy ranges, removing bad time intervals and filtering out unwanted light-sources. The pattern values of an event describe whether it was a single-, double-, triple-pixel event or higher, see Figure 9. Events covering many pixels will typically be caused by cosmic rays and they will need to be filtered out in any scientific analysis. The flag value of an event describes the conditions of the pixels involved, for example hot pixels or pixels outside of the field of view. For a scientific analysis flag=0 should be used.

For the creation of response matrices, the SAS tasks *rmfgen* and *arfgen*, creating respectively, a Redistribution Matrix File (RMF), and an Ancillary Response File (ARF) are available. The matrix created by *rmfgen* describes the response of the MOS or PN as a function of energy. It can be used together with the spectrum and the ARF, when doing spectral fitting in, for example, XSPEC. The task *arfgen* retrieves calibration information, does corrections for instrumental factors according to user specifications and formats the output so that it can be used by for example XSPEC.

For most of the photometrical analysis SAS provides everything needed, with a few exceptions. For the creation of new columns, by performing math on the existing columns the FTOOLS task *fcalc* can be used. For generating tables of data, that can be read into for example an IDL-programme, the FTOOLS task *fdump* can be used. Also
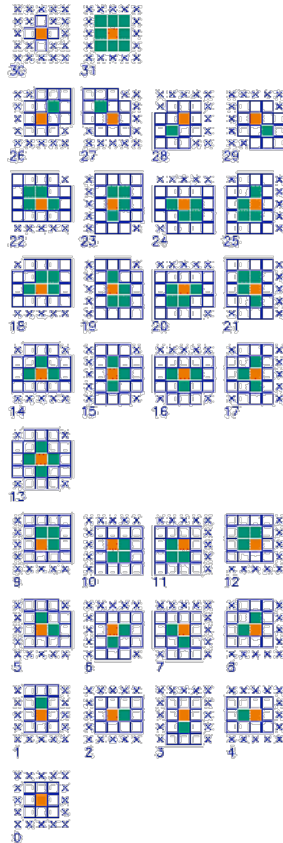
Figure 9. Different pattern types are shown, image from the 'XMM Users Handbook'

the event files from XMM are not particularly ordered, for ordering a fits file the FTOOLS task $fsort$ can be used. This task rearranges an input fits file according to the numerical order of a chosen column.

For the spectral analysis the first thing to do is to group the spectra with the background spectra and the response matrices. For this the FTOOLS task $grppha$ can be used. Here the spectra is also binned according to preferations. When the spectra are readily grouped the XSPEC software can be used to plot and fit an X-ray spectra according to the preferred model.

XSPEC is a spectral-fitting programme for X-ray spectra. It is instrument independent and can therefore be used on data from any detector. Several different models are available for the fitting. One type of model, included in the software is a photo-electric absorbed power-law, which is the expected model for a GRB afterglow spectrum, to be explained in Section 2.2. After the fitting, the model can be plotted together with

the data. The XSPEC commands also include *steppar*, which holds the possibility, for a user-defined number of steps and step-sizes, to calculate the chi-squared, χ^2, values for a parameter of choice, in the used model. The result can then be visualised by use of the command *plot contour* which maps how χ^2 varies with the parameter.

1.7. Literature

In this thesis the object treated is GRB 031203, which is a long duration gamma-ray burst. On the subject of this GRB there exists a number of papers. The subject of the thesis is the dust scattered X-ray halo that surrounds the GRB, or more precisely, surrounds the afterglow. To my knowledge there only exist three papers on this subject; Vaughan et al. (2004), Tiengo & Mereghetti (2006), Watson et al. (2006). The methods for the detection and quantisation of the dust scattered halo, around GRB 031203, used in this thesis, are inspired by these papers. To this date there have only been discovered 5 of these dust scattered halos around gamma-ray burst afterglows; GRB 031203, GRB 050713A, GRB 050724, GRB 061019 and GRB 070129, see Figure 10. GRB 031203 was the first to be found. On the subject of these halos there exist 5 papers,Vaughan et al. (2004), Watson et al. (2006), Vaughan et al. (2006), Tiengo & Mereghetti (2006) and Vianello et al. (2007). For the four last of the five GRBs there are SWIFT satellite observations, but there are only XMM-Newton observations available for the two first; GRB 031203 and GRB 050713A. The data from SWIFT observations are much less resolved than the XMM observational data. Therefore an in-depth detailed analysis is better obtained by use of XMM observations. GRB 031203 is the clearest most resolved halo discovered until now, as we see from a comparison between the four halos displayed in Figure 10 and the one for GRB 031203 in Figure 16.
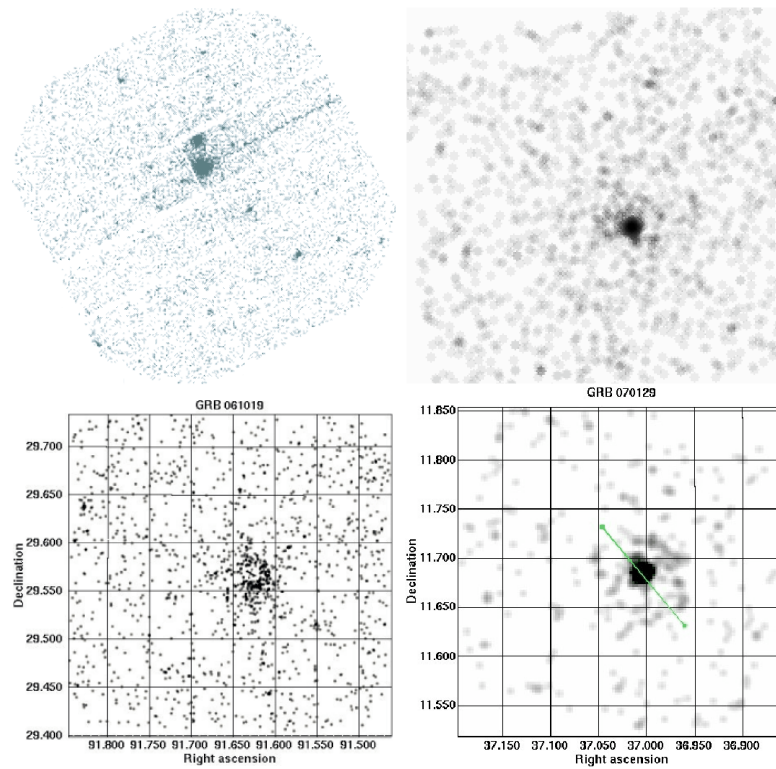
Figure 10. Images of the latest four afterglows showing indications of a scattered halo around
them. Upper left: GRB 050713A, covering an energy range of 0.5-2 keV, from Tiengo & Mereghetti
(2006). Upper right: Image of the afterglow of GRB 050724, covering an energy range of 0.8-2.2
keV, produced by Mike Alexandersen. Lower left: Image of GRB 061019, covering an energy range
of 0.2-4 keV, from Vianello et al. (2007). Lower right: Image of GRB 070129, covering an energy
range of 0.2-4 keV, from Vianello et al. (2007).

Ê

2. Theory

2.1. Small Angle Scattering off Dust

According to the law of refraction, when light travels through the vacuum of space and encounters matter of some type, whether it is transmitted or reflected depends on the index of refraction of the material in question. The refractive index for a material will be different for different wavelengths.

The light will encounter the matter at some angle. We can then define a critical angle, θ_c, above which all of the light will be reflected. The critical angle can be written as;

$$\theta_c = arcsin\left(\frac{n_1}{n_2}\right), \tag{1}$$

(Guenther, R. D. 1990). The critical angle is illustrated in Figure 11. Here n_1 is the refractive index of the medium the light comes from, in this case vacuum, and n_2 is the refractive index of the material the light is incident on. For vacuum the refractive index is 1, at all wavelengths. Below this critical angle the light will only be partly reflected and the rest will be transmitted, the smaller the incident angle, the larger will the transmitted fraction of the light will be. When the light is only partly reflected the intensity of the reflected light will of course be lower than when it is fully reflected, and the effects will thereby be more difficult to spot. So it is only light that grazes the particle, hitting it with a certain angle, close to or above the critical angle that will be scattered significantly to display a visual effect. The equation for the critical angle only has a solution when $n_2 \leq n_1$. When this requirement is not fulfilled there will therefore be no critical angle, making full reflection impossible.

The law of refraction applies only when the size of the scattering medium is significantly larger than the wavelength of the light approach-

$$\theta_i = \theta_r$$

transmission +
reflection

full reflection

Vacuum

incident light

reflected light

θ_c

θ_i θ_r

n_1

n_2

Dust grain
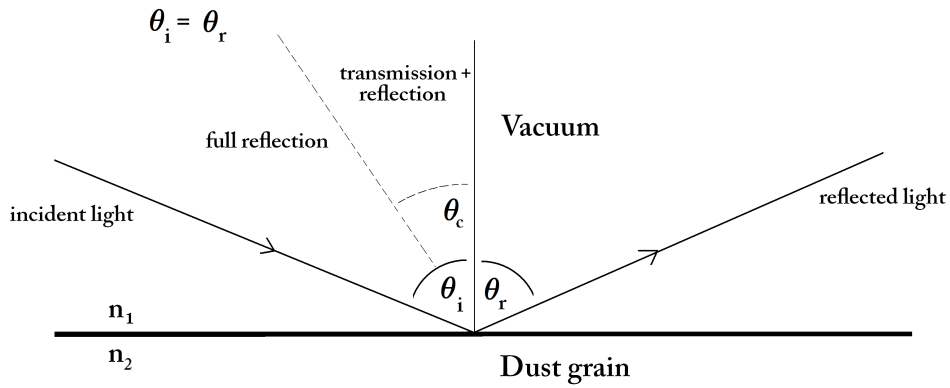
Figure 11. Diagram showing how the critical angle, determining whether there will be full reflection or part reflection part transmission, is defined. The critical angle is measured from the normal to the surface-plane. The angle of the reflected light is the same as the angle of the incident light.

ing it. When this is not the case other types of scattering come into play. Here the light is scattered more diffusely in all directions, not giving as clear visual effects in observations. For a typical dust grain the size is around a few hundred nanometers (Vaughan et al. 2004). This means that, for scattering off dust, the law does not apply for light in the range from radio to long wavelength-UV. Light in the range from short wavelength-UV (around 10 nm) to gamma radiation should be able to either scatter or be transmitted, according to Equation 1, when encountering dust.

Refractive index, n

1

0

Infrared   Visible   Ultraviolet   X-ray
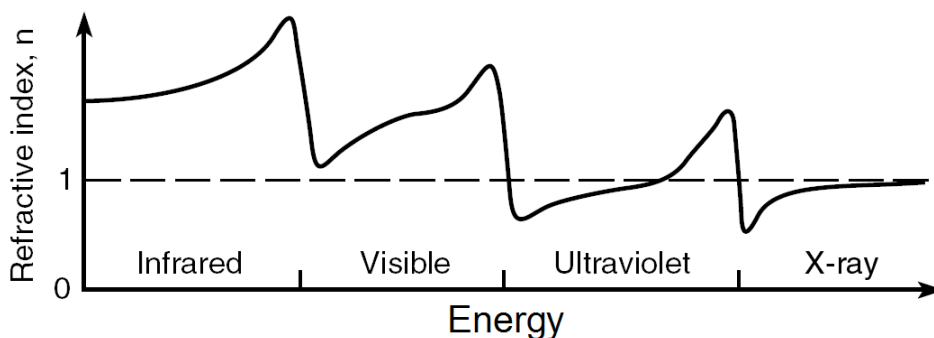
Energy

Figure 12. Plot of the refractive index as a function of the wavelength of the incident light, from Attwood (2007)

In Figure 12 a general plot of the refractive index, n, versus the energy of the incident light can be seen. We see that the refractive index for

any medium is above one for light less energetic than UV-light. Since vacuum only has a refractive index of one, θ_c will not be defined for these wavelengths and thereby there will never be total reflection, but as mentioned, when looking at dust for these wavelengths, this type of scattering is not applicable. For UV-light the lower energy end is the only part that has a critical angle, but for this range of the UV-light encountering dust, the law of refraction is also not applicable.

For X-rays and gamma-rays the refractive index is always below one. For gamma-rays and hard X-rays, the refractive index is very close to one. The critical angle will be so large that the light that is fully scattered, is within large angles to the normal of the surface meaning that they only graze the particle. The path of the reflected photons are thereby too close to the path of the non-scattered light to be distinguished. The light that is scattered at large enough angles to be distinguished is only partly reflected (the rest transmitted) and therefore is too diffuse to be clearly seen.

For soft X-rays the critical angle is slightly smaller and therefore the light can be fully reflected while grazing the dust at large enough angles to be distinguished from the non-scattered light. We will see the light scattered around the source at differing angles adding up to a haze of X-ray light around the source fading out at larger radii, see Figure 2. This type of scattering through small angles, relative to the surface[7] or grazing incidents, is the physical mechanism responsible for the phenomenon of the GRB X-ray afterglow haloes.

2.2. Observational Products of GRB Afterglows

When looking at any set of observational data, a GRB will be quite easily identified. In images the GRBs will most often appear as the

---

[7] In our above convention, these small angles correspond to large angles relative to the surface-normal.

brightest source in the frame, even though it might as well also be the most distant source. The same thing applies for the afterglows of the GRBs. The GRB will be visible as a bright source in an image covering gamma ray wavelengths. The X-ray afterglow will, shortly after the GRB itself, be visible as a bright source in an image covering X-ray wavelengths.[8]

The light curves from GRB afterglows, representing how the flux evolves in time, have power-law shape.

$$F(E) = F_0 \cdot t^{-p} \tag{2}$$

Here F is the flux, E is the energy and p is the powerlaw index. As explained in Section 1.3 the light curve acts like this because the emission is caused by synchrotron radiation which has a power-law shape. The shape of the light curve is not always as simple as just a power-law. There will in some cases be breaks in the power-law, where the power-law index changes. This is thought to be caused by either the density profile of surrounding material or the beaming. Examples of afterglow light curves can be seen in Figure 13.

The synchrotron radiation nature of the afterglow also causes the spectrum, representing how the flux depends on the energy, to have a power-law shape. The spectrum for the afterglow emission can be written as;

$$F(E) \propto E^{-\Gamma} \tag{3}$$

Where Γ is the photon index of the power-law. Since the light from the afterglow travels through dust and gas on its way to the observer, the actual observed spectrum will be an absorbed power-law;

$$F = e^{-n_H \sigma(E)} \cdot E^{-\Gamma} \cdot k_n \tag{4}$$

Here n_H is the absorbing column, which represents how many particles there are in a column from the observer to the source, of one cm^2

---

[8] Following this an optical and then a radio afterglow will be visible when looking at images in these wavelength ranges.

cross-section, $\sigma(E)$ is the cross-section for absorption by the particles and k_n is a normalisation constant. Since the cross-section $\sigma(E)$ has a dependency on the energy, the absorbing affects the various energy ranges differently. The lower energy ranges are mostly affected, since these have the highest cross-sections. The absorption will be added up for the entire path of the afterglow light through the universe but will mostly consist of the absorption in our own Galaxy and also partly from the GRB host galaxy. If the observed spectrum is fitted to an absorbed power-law, the absorbing column, n_H, can be found. Since we have estimated values for the absorbing column in our Galaxy for different directions, the absorbing column of the GRB host galaxy can be estimated from the afterglow spectrum. Examples of spectra from GRB afterglows can be seen in Figure 14.
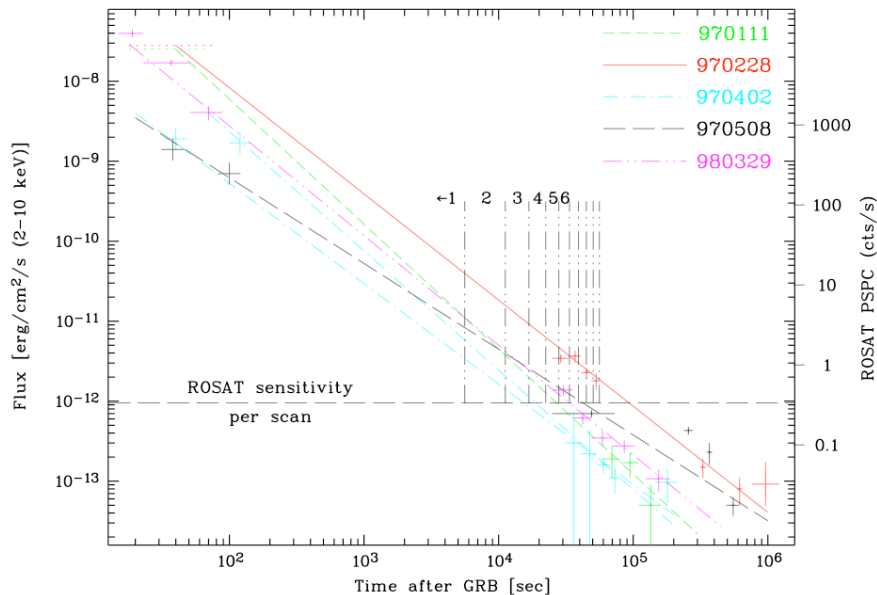
Figure 13. Examples of GRB afterglow light curves from a ROSAT survey, by Greiner et al. (1999)
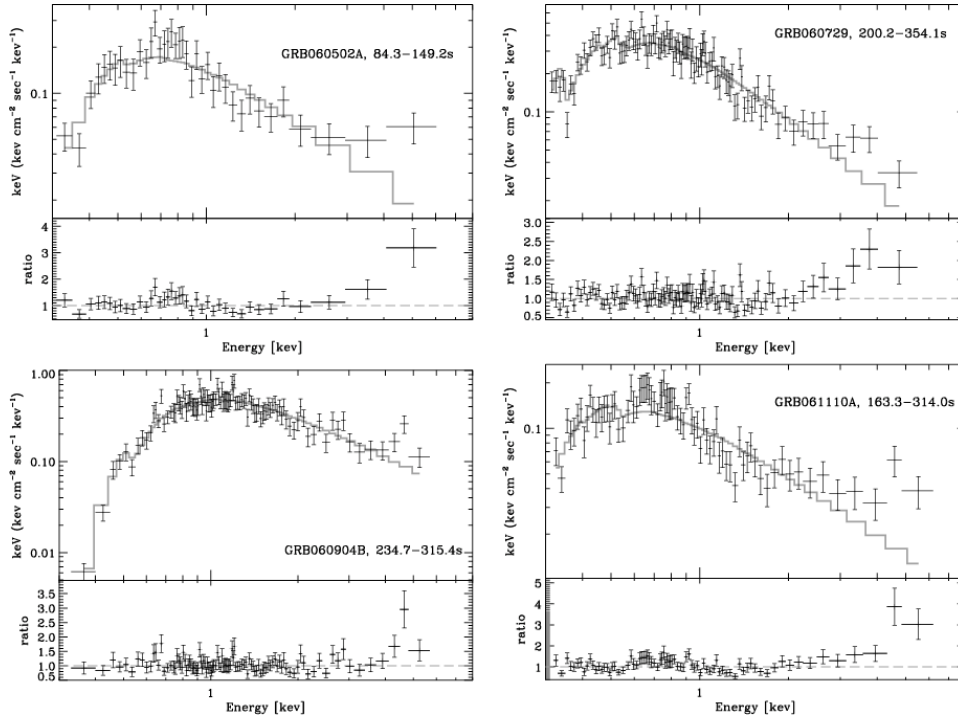
Figure 14. Examples of GRB afterglow spectra, from Moretti et al. (2008). Here we clearly see the absorption effect and it is clear that lower energy ranges of the spectra are more affected by the absorption.

2.3. Methods - The effects of scattering on observational products of afterglows

As the X-ray light emitted by the fading afterglow of the GRB is scattered by intervening dust, a particular phenomenon arises; a distinct ring around the GRB appears in observations. This phenomenon was first spotted in 2003 from observations of GRB 031203 (Vaughan et al. 2004). Since then a few other GRB halos have been spotted, listed in Section 1.7. This ring is not present in the gamma ray range nor in later afterglow stages of optical or radio emission. This fact is linked to the special relationship between X-ray light and dust, explained in Section 2.1. The phenomenon of X-ray halos in general was not a new concept. A large number of both theoretical and observational papers have been published on the subject of halos around X-ray sources (Mauche & Gorenstein 1986).

The ring around a GRB afterglow grows. This happens because the afterglow is not a constant source. The variability of the afterglow arises because it takes the photons a certain time to reach our telescopes, and the time it takes depends on the distance it travels. Photons that are scattered to larger angles, i.e. we see them further from the GRB centre, arrive later, because they have to travel farther, see Figure 15. Permanent sources will just have scattered photons from all angles at once since the light radiates through all scattering angles at all times. Off course the halo or haze of scattered light will, for both permanent and non-permanent sources, fade when moving from the source outward. Light scattered at larger angles will get more and more diffuse because it is spread over a larger and larger area.

The fact that afterglows fade in time and thereby causes these expanding rings gives us the opportunity, which is not possible from constant X-ray sources, to estimate the distance to the scattering dust from the time evolution of the halo.
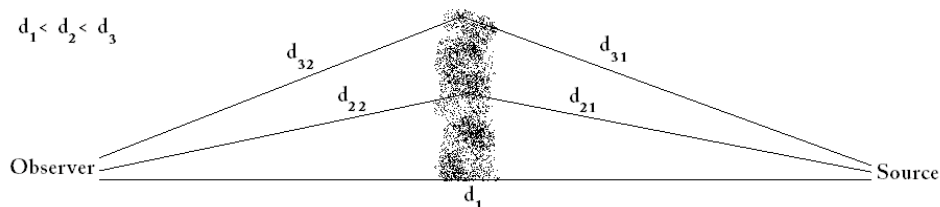
Figure 15. We see light travelling from a source through some intervening dust. Some of the light travels un-scattered through, whereas some is scattered at small angles and some scattered at greater angles. Here we have that $d_2 = d_{21} + d_{22}$ and $d_3 = d_{31} + d_{32}$. We see that light scattered at larger angles have a longer way to travel, and will thereby arrive later.

X-ray light from any source, be it constant or fading, scattering on dust, will have an imprint of the dust characteristics in its spectrum. By fitting the X-ray spectra it is possible to derive the size and composition of the dust. In this case it is probably better to have constant X-ray sources since this will mean that more data is available.

In this thesis an investigation and analysis of a halo around GRB 031203, caused by the scattering of an interfering dust medium, is performed. This analysis enables the characteristics of the interfering dust

to be derived. Throughout Section 2.3 the theory of the equations and methods used, is presented.

2.3.1. Visualising Halos Around GRB Afterglows

When the light from a source is scattered by intervening dust, it is diverged by a certain angle governed by the geometry of the dust and the energy of the light. This causes a multitude of scattering angles to arise. When looking at the object, this will be visualised as a halo or a haze around the source. For the fading light of an X-ray afterglow, this will be a distinct ring growing in time.

The most simple way to recognise if a halo is in fact present is of course to make an image from the observations and see what it looks like. If the afterglow light is in fact scattered by an intervening medium of dust, we will see a bright source surrounded by a fuzzy ring. The afterglow will not be represented by a point and the ring will not just be a thin circle. The point spread function of the instrument doing the observation makes the afterglow appear as a small disk and the ring width is also extended. Other effects causing the thickness of the ring is the time span of the observation and the thickness of the dust medium doing the scattering.

If a halo is faint, it can be difficult to spot just by looking at an image since the background noise can look almost as bright as the halo. It can be an advantage to divide the observations into energy intervals and see if any features show up in one of the separate intervals and then use this interval for further analysis.

When the light travels through the dust, some of the light will travel unscattered through and the rest will be scattered through differing angles. The un-scattered light will of course arrive first, hereafter the light that was scattered to small angles and later the light that was scattered to larger angles, see Figure 15. The first arriving light will be closest to the afterglow and the later will be further from it.[9] The

---

[9] There will not be a maximum scattering angle, the light will just get more and more diffuse and unrecognisable.

effect of this can be shown if we instead of just putting the entire observation into one image, divide the observation into time intervals. If this is done the halo should then be seen as a ring that grows through the time intervals. This type of visualisation of the time evolution was done by Vaughan et al. (2004), see Figure 16. Of course this type of time interval images, can only be done for X-ray halos that are properly resolved. If the halo is only vaguely seen on the total time image, it will probably not be possible to see the growth or maybe even to see the presence in time-divided intervals.
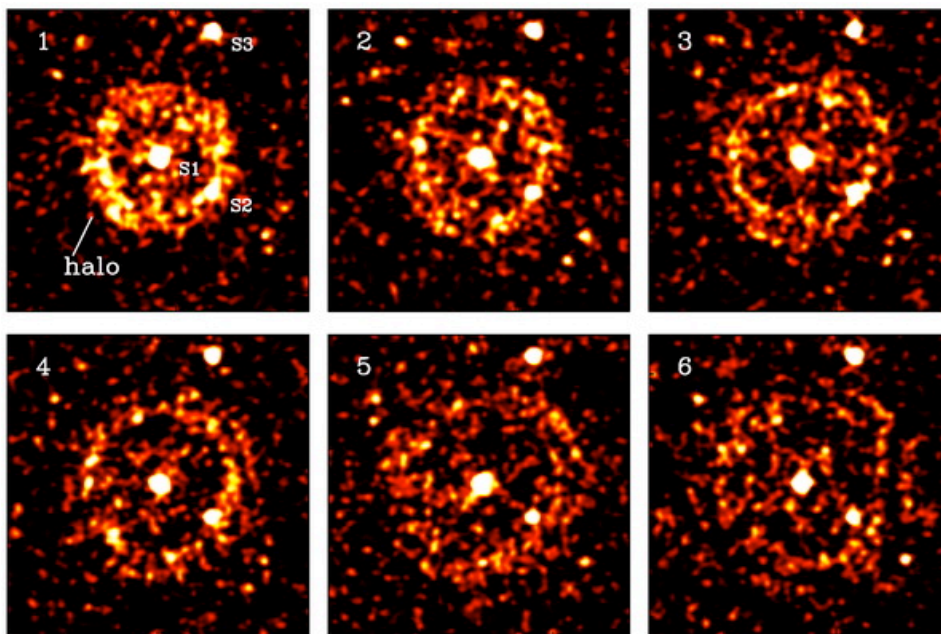
Figure 16. Image by Vaughan et al. (2004), showing the growth of the halo around the afterglow belonging to GRB 031203. The energy interval used here is 0.7-2.5 keV. The data used is the combined MOS camera data. The six images show subsequent time intervals of the observation.

When an image is made, we typically take the x and y coordinate and then make a two dimensional histogram showing the counts at each coordinate set. Instead of this standard type of image another kind of image, also showing the sources in the observation, can be made, see Figure 17. From the x- and y-coordinate the distance relative to some centre can be found. Naming this distance, θ; $\theta^2 = (x - x_c)^2 + (y - y_c)^2$, where (x_c, y_c) is the coordinates of the centre, an image with time

instead of x and θ^2 instead of y can be made. If this centre, defining θ, is placed at the afterglow location, the growing size of the halo through time will of course mean that θ^2 grows through time. The result will be that this type of image will show a inclining line for growing sources, like GRB halos. A source that is constant will of course have a constant θ and θ^2-value and thereby be represented as a horizontal line. This type of dynamical image was done by Tiengo & Mereghetti (2006), and is displayed in Figure 17. The effect of this is basically that the three dimensions of the observations; two spatial and one time dimension, are reduced to two and can therefore all be included in one image. The advantage of this is that haloes or rings around the central source, which are not well resolved, will be much more clear. This is because all the counts at each θ-value are added up to represent one point. In this way the halo stands out more from the background. The reason for choosing θ^2 and not θ is to get an even background. For a plot with θ on the y-axis an even background would look darker and darker with increasing θ since the ring, the counts are added up from, gets bigger. For θ^2 this is not the case, and the darkness of the background will therefore be even.

This growth can also be visualised in a more quantitative way. Instead of making an image from the θ^2 dependency with time, the observation can be divided into time intervals, as discussed above, and for each time interval a counts versus θ plot can be made, if the counts are binned in some way. If there are not too many other sources disturbing the picture, the ring around an afterglow should appear as a peak located at some θ. This peak should be expected to move outward through the plots representing the different time intervals. From these plots the location of the halo ring at different times can be found and a plot of halo-size versus time can be made. This was done by Vaughan et al. (2004), see Figures 18 and 19. The relationship between halo-size and time can then be fitted to a suitable function, to be elaborated in the following sections.
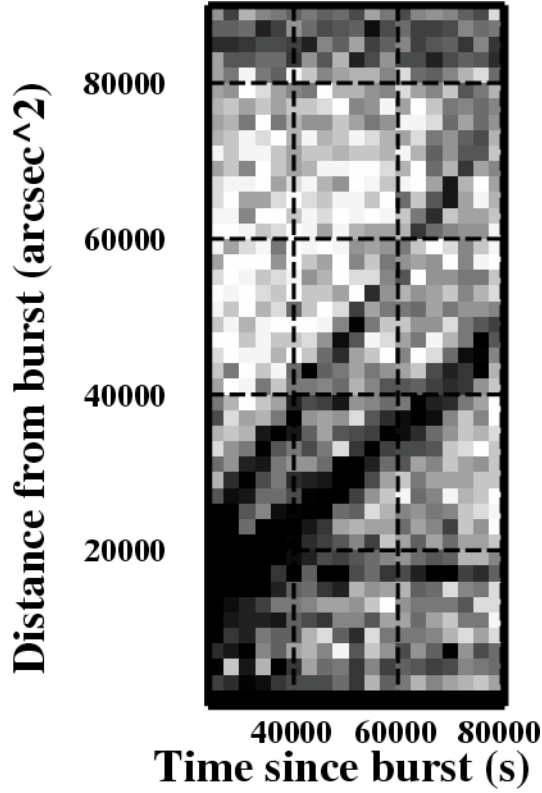
Figure 17. Dynamical image of GRB 031203, from Tiengo & Mereghetti (2006). The energy interval used here is 1-2 keV, the pattern values are 0-4 and the data is from the PN camera.

2.3.2. Equations Linking the Distance of the Dust with the Scattering Angle, θ

We consider a dust slab at a distance d_d, that scatters the light emitted from a source at a distance d_s. The scattering angle is given by θ, see Figure 20. The time delay of a photon scattered through the angle θ will be;

$$t_d = \frac{((h + h') - d_s)}{c} \tag{5}$$

Here c is the velocity of light and $h + h'$ denotes the detour that the scattered photon takes. If the dust resides in our own Galaxy, and the source is at cosmological distances then $h' \approx d_s - d_d$ and we thereby get;

$$t_d = \frac{(h - d_d)}{c} = \frac{\frac{d_d}{cos\theta} - d_d}{c} \tag{6}$$
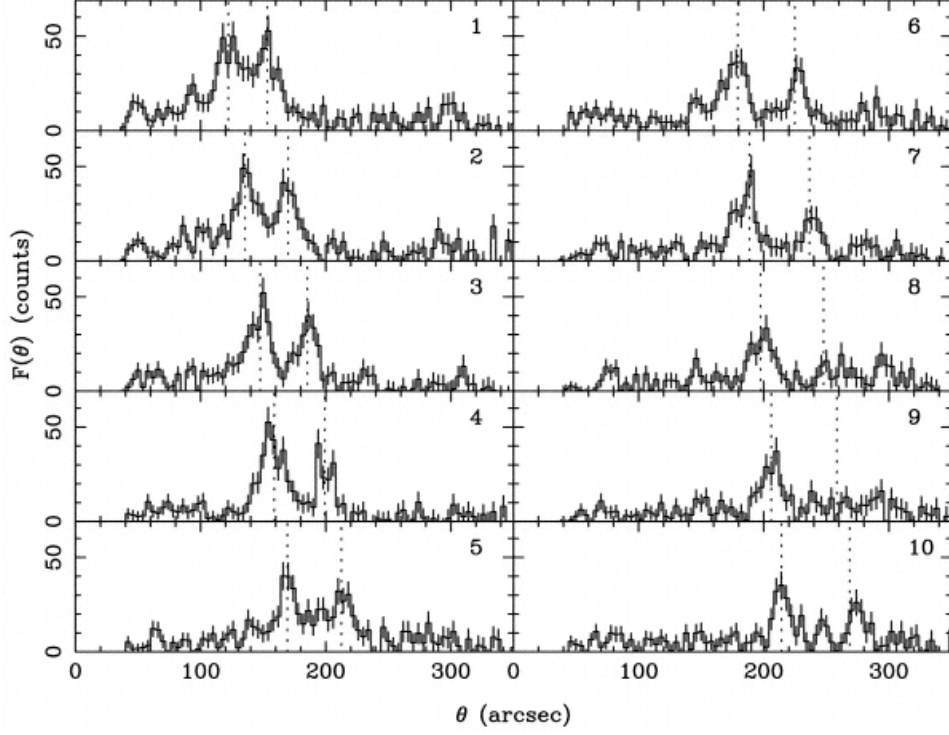
Figure 18. Plots of counts versus θ for ten consecutive time intervals of the afterglow halo for GRB 031203, by Vaughan et al. (2004). The dotted lines represent the peak locations. The energy interval used here is 0.7-2.5 keV. The data used is the combined MOS camera data.

Since the scattering angle considered is very small we have that $cos\theta \approx 1 - \frac{\theta^2}{2}$, which then yields;

$$t_d = \frac{d_d \left(\frac{1}{1 - \frac{\theta^2}{2}} - 1 \right)}{c} = \frac{d_d}{c} \frac{\frac{\theta^2}{2}}{1 - \frac{\theta^2}{2}} = \frac{d_d}{c} \frac{\theta^2}{2 - \theta^2} \tag{7}$$

Since θ is very small $2 - \theta^2 \approx 2$,

$$t_d = \frac{d_d}{c} \frac{\theta^2}{2} \tag{8}$$

So the distance to the dust that scatters the light as a function of theta, can be written;

$$d_d = \frac{2ct_d}{\theta^2} \tag{9}$$
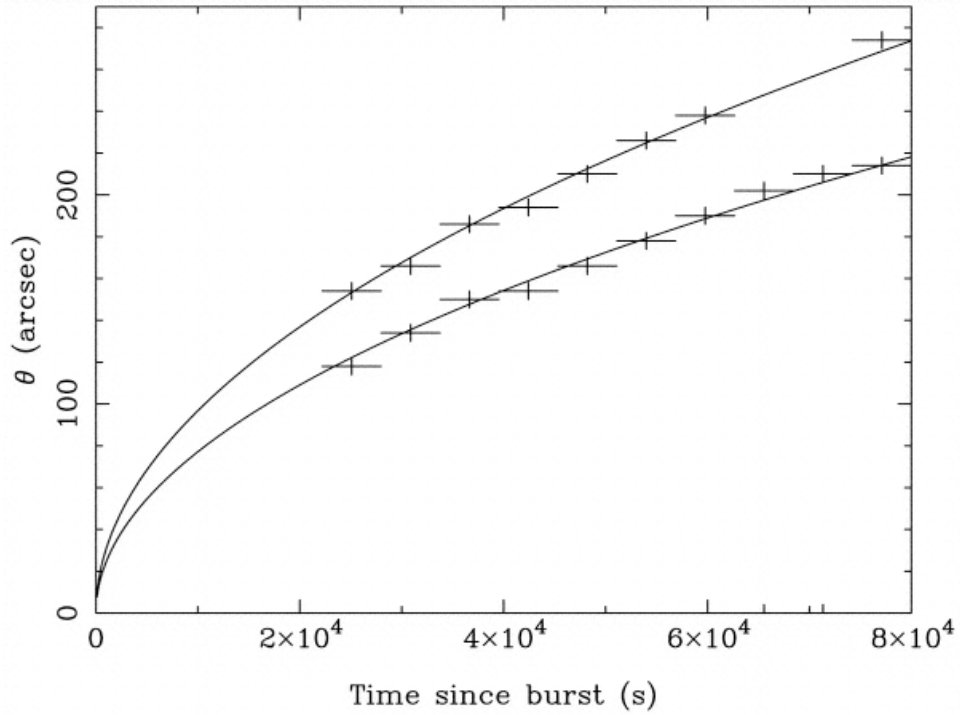
Figure 19. Plots of θ versus time for the two rings around the afterglow of GRB 031203, derived from Figure 18, by Vaughan et al. (2004).

If we look at how the halo evolves in time; θ as a function of time, which is an observable evolution, the implications from the above equation are;

$$\theta = \sqrt{\frac{2c}{d_d}} \cdot t^{1/2} = const \cdot t^{1/2} \tag{10}$$

So the halo grows as a power-law in time with a power-law index of $1/2$.
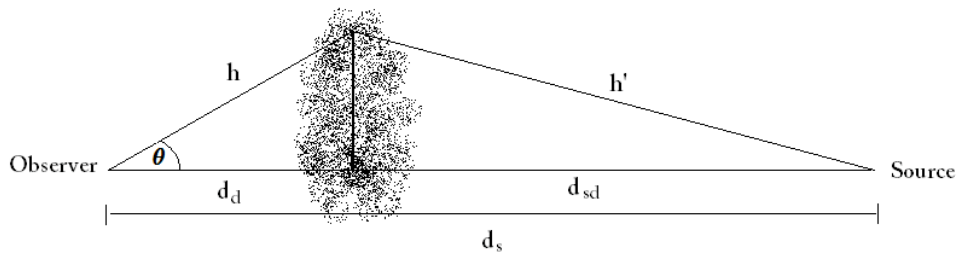
Figure 20. Diagram showing the geometry of the scattering of light from a source by intervening dust. The angle is greatly enhanced for illustrative purposes.

2.3.3. Estimating the Distance by Fitting the Photometrical Data

We look at an evenly illuminated CCD and define a radial coordinate, θ, relative to some centre. Moving from $\theta = 0$ to higher $\theta - values$ the total number of counts at each θ will grow, if we have a constant bin size for the $\theta - bins$. This is of course because the circumference of the circle where θ has equivalent values grows for θ growing. If we define that the bins should be such a size that there is an equal number of counts in each bin, the bin size, $\delta\theta$, must be inversely proportional to θ.[10]

If we look at the distance in Equation 9 we see that d_d goes as θ^{-2} so starting at $\theta = 0$ and moving outward we will get counts that are scattered from closer and closer distance. Equation 9 actually only applies to photons that originally come from the central source that θ is defined by, but just for the sake of the argument we can apply the equation to the case of the evenly illuminated CCD discussed above. Since d_d is proportional to θ^{-2}, the number of counts detected at each θ can be described as a function of this distance, d_d, representing where the photon was scattered if it originally came from a central source.

If we wish to make a plot of this dependency, we will have to bin the counts in some way. We denote the bin size δd. Keeping the earlier notion that we want an even number of counts in each bin, we have that the quantity counts/δd should be proportional to $1/\delta d$. The quantity δd can from Equation 9 be written as,

$$\delta d \propto \theta^{-3}\delta\theta \propto \theta^{-4} \propto d^2, \tag{11}$$

since we have $\delta\theta \propto \frac{1}{\theta}$ and $d \propto \theta^{-2}$. This means that counts/δd will be proportional to d^{-2}. The dependency of counts/δd as a function of distance will be a power-law with a power-law index of -2.

Instead of an evenly illuminated CCD we consider the case of having one source at some angle from the centre, θ. The effect of this source

---

[10] $number\ of\ counts\ \propto 2\pi\theta \cdot \delta\theta$, if number of counts is to be constant then $\theta \propto \delta\theta^{-1}$

on our counts/δd versus distance relationship depends on the time behaviour of the source. From Equation 9 we see that the distance is proportional to the time. This means that the effect of a source that does not change through time will be smeared across the power-law, since the time coordinate changes while the θ-coordinate does not. For a source whose θ-value depends on the time, according to the proportionality, $\theta^2 \propto$ time, which is the case for the halo, the smearing will be cancelled and a peak will be added to the power-law. As mentioned before, because of the instrumental point spread function a point source will not appear as a point source, so according to the point spread function the peaks will be Lorentzians and not just one point peaks.

Since the distance in Equation 9 represents the distance to where the photon was scattered from, the x-location of the Lorentz peaks, in a plot of counts/δd versus distance, will represent the distance to whatever the photons scattered off.

A ring growing as $\theta \propto t^{1/2}$, would appear as a peak in the above described plot if we were to place $\theta = 0$ in the centre of the ring. If the ring is the optical effect of the scattering of light from a GRB afterglow through a medium of dust, the distance to this dust will be evident from a counts/δd versus distance plot. A plot like this was done by Tiengo & Mereghetti (2006) and can be seen in Figure 21.

One of the parameters governing the Lorentzian is the Half Width Half Maximum, HWHM, representing the width of the peak which as mentioned is mainly caused by the point spread function. But if the source, be it the optical effect of scattering or an actual source, is extended, it can also contribute to this width. For the image of a halo caused by dust scattering, as mentioned in Section 2.3.1, the width of the ring is caused by the point spread function, the time span of the observation, and also the depth or thickness of the dust slab doing the scattering. The width caused by time is cancelled in the counts/δd versus distance relationship, but the depth will contribute to the HWHM. When fitting this type of function to observations of a dust scattered halo, a good rule of thumb is that if the peak is much

wider than predicted by the point spread function alone, then we can derive some minimum of depth of the dust slab doing the scattering.

If other sources than the GRB afterglow are present, they will be smeared, as discussed above. This smearing, if it is asymmetrical, might affect the power-law behaviour so that the discussed power-law index will deviate from the above found value of -2.

If we integrate over the full Lorentzian (from zero to infinity), we will get the net number of counts in the peak. If there are only a few halo counts in the fitted Lorentzian, it can be questionable whether the peak does actually represent a dust medium, causing scattering of light, or it is just random noise looking like a peak. So integrating the fitted Lorentzian is a good way to check the credibility of the results.
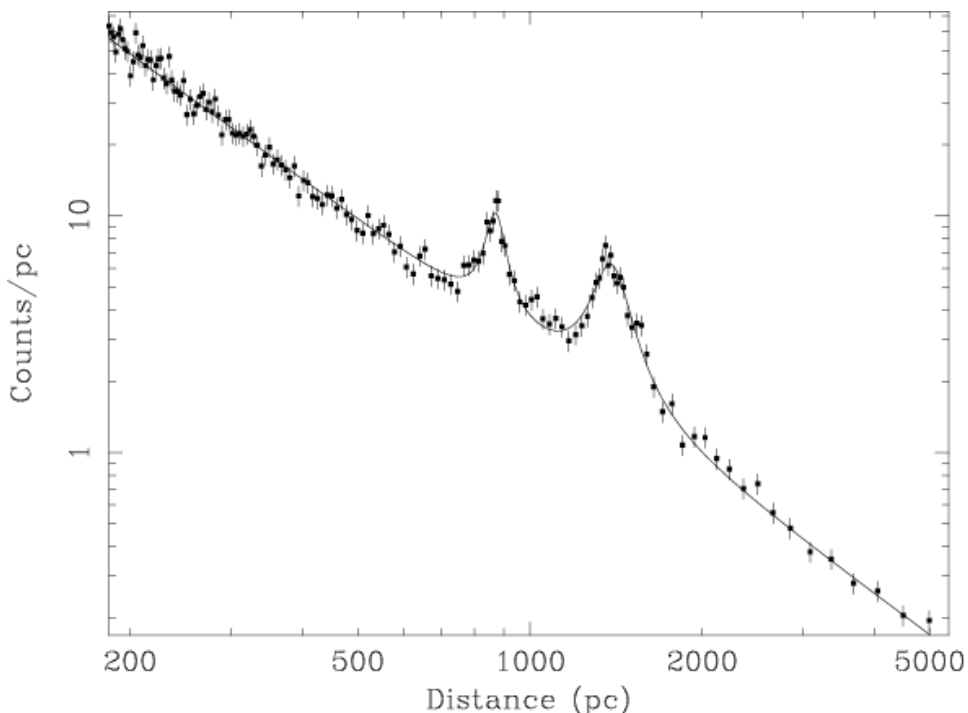
Figure 21. Plot showing counts/pc versus distance for the data from the afterglow of GRB 031203, by Tiengo & Mereghetti (2006). The energy interval used here is 1-2 keV. The pattern values included in the filtered data are 0-4.

Now we look again at the radial plots displayed in Figure 18. As discussed in Section 2.3.1, in a plot of counts versus θ a ring centred at $\theta = 0$ will constitute a peak at some θ-value. If the ring grows, the

peak will be stretched, but if the observation is divided into shorter time intervals the stretching will be avoided and will instead cause peaks at different θ-values for each time interval. For later times the θ-value for the peak will be larger. Collecting these θ-values for different times it will be possible to plot a θ versus time relationship, as done in Figure 19. According to Equation 10, θ should be proportional to $t^{1/2}$ with the proportionality constant $k = 2c \cdot d_d^{-1/2}$. Fitting the θ versus time relationship to a power-law with power-law index 0.5 will reveal the proportionality constant and thereby also the distance to the scattering dust.

2.3.4. Spectral Fitting

Each event in an observation will besides coordinates and a time of arrival also have a connected energy. If we bin the counts from the total time of the observation in some way, it is possible to make a plot of counts, or normalised counts, versus energy. This is the spectrum of the observed light. As explained in Section 2.2, the emission from a GRB afterglow behaves as a power-law, and because it travels through dust and gas in the universe there will be some absorption. The observed spectrum will thereby be a photo-electric absorbed power-law, see Equation 4. The absorption of the light from the afterglow by dust and gas happens not only in the slabs causing the scattering, but in all of the path of the light through the universe. The absorbing effect on the spectra is governed by two parameters, the absorbing column, n_H, and the cross-section for absorption, $\sigma(E)$, which is a function depending on the energy of the photon.

To investigate the effect of dust scattering on the afterglow emission, spectra can be extracted separately from the halo and the afterglow area respectively. In this way the two spectra can be compared.

If these observed spectra is fitted according to the model spectrum of a photo-electric absorbed power-law, the absorbing column and the photon indices can be derived. Since the halo expands through time

the scattered light seen in the halo will get more and more diffuse, see Figure 16. This means that spectral data for the halo from the last parts of the observations might not be very reliable. The actual halo counts will be too thinly distributed relative to the background. To prevent the quality of the halo spectrum to be affected by this, it can be a good idea to only use the events from earlier parts of the observation, where the halo was more well defined.

Since the light from both the afterglow and the dust-scattered halo travel through the same path, the absorbing column should be the same for the two. If this applies for the observed spectra, the afterglow- and the halo-spectrum can be fitted simultaneously while locking the absorbing column to be the same for the two. This will mean that there is more data to estimate the absorbing column from, and the basis for the fitted absorbing column will be better.

To illustrate the effect of the dust scattering on the afterglow emission, a common plot of the halo-photons spectrum and the afterglow-photons spectrum can be made. The spectral fitting described above was done by Vaughan et al. (2004) and is displayed in Figure 22.

In a plot like this it is evident that the scattered halo has a spectrum that is steeper than the afterglow spectrum. This means that the photon index of the power-law is higher for the halo spectrum than the un-scattered afterglow spectrum. This is connected to the efficiency of the scattering which is dependent on the energy of the light being scattered. As explained in Section 2.1, the critical angle determining when light is totally reflected (scattered) or partly reflected (scattered) and partly transmitted (unscattered) depends on the energy of the light. We see from Figure 12 that for X-rays the lower energy end has lower refraction index than the higher end, which leads to larger critical angles for the higher energy end. This means that for the high energy end, much fewer X-rays will be incident on the dust with an angle higher than θ_c, relative to the dust surface normal, and therefore full reflection will be more rare. So looking again at the spectrum for the halo, the light will be scattered more efficiently at lower energies
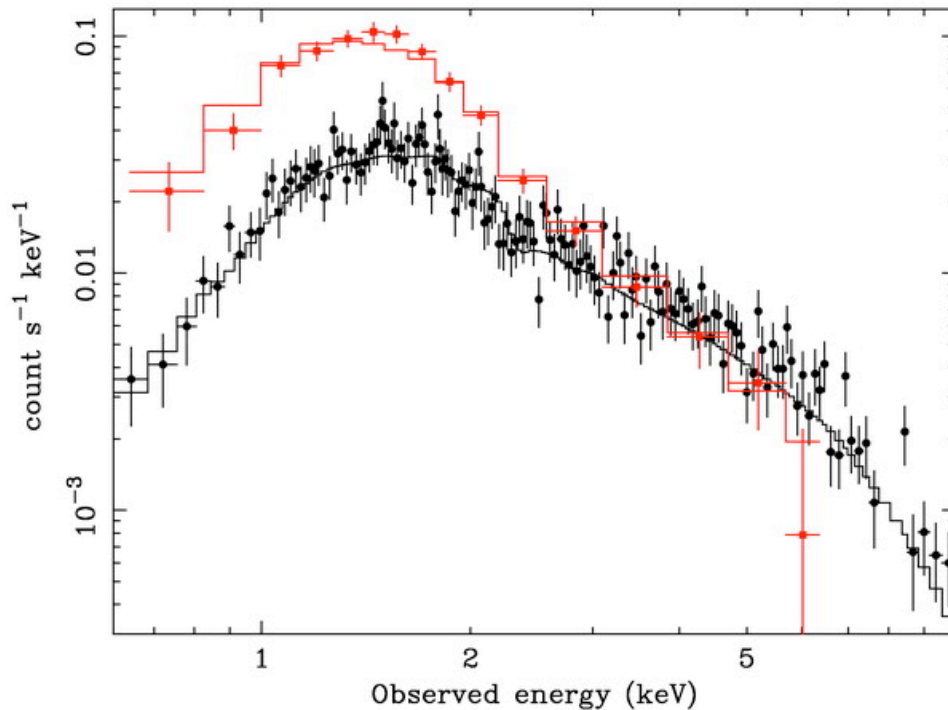
Figure 22. From PN data of GRB 031203, the halo-spectrum (red) and the afterglow spectrum (black), by Vaughan et al. (2004)

and less efficiently at higher, causing the halo spectrum to have lower intensity than the original emission in the high energy end and closer to the same intensity in the low energy end, thereby making the spectrum steeper. In the spectrum in Figure 22 it also looks like the intensity of the halo spectrum is greater than the afterglow spectrum. This is only because the halo spectrum is extracted from a larger area.

2.3.5. Size of the Dust Grains

If time resolved data for the evolution of a dust scattered halo is available, then the flux versus time dependency is given. Knowing also how the halo grows through time, we have the θ versus time dependency. These two relationships together gives us how the scattered flux falls of with radius, $F(\theta)$. This relationship depends on the size of the largest grains, a_{max}, in the grain size distribution. The differential scattering cross-section also depends on the grain size. This makes it possible to

fit the differential scattering cross-section to this observed halo flux as a function of scattering angle, thereby finding a_{max}. The fit can be performed by the use of the differential and total scattering cross-sections of the Rayleigh-Ganz approximation for a spherical particle a, given by Mauche & Gorenstein (1986).

Some grain size distribution will have to be assumed for the fitting, be it single size or a power-law distribution. This is beyond the scope of this thesis, but a fit to the halo flux observed with the XMM satellite for GRB 031203 was done by Watson et al. (2006), who using a power-law distribution of $a^{-3.5}$ found an $a_{max} = 0.50 \pm 0.03 \mu m$. This value corresponds to the generally accepted norm for dust grain sizes.

3. Data and Results

3.1. Observations

The first data set used in this report is of the afterglow of the gamma ray burst GRB 031203. The Observational Data Files (ODF) was retrieved from the $XMM-Newton\ Science\ Archive$. The burst was detected by the Imager on board the INTEGRAL satellite on December 3, 2003 at 22:01:28 UT. It was found to be a single peaked burst spanning $30s$ and with a peak flux of $1.3 \cdot 10^7 ergs \cdot s^{-1}$ in the $20-200keV$ band. The XMM-Newton observational data used in this report spanning $58ks$ was started December 4, 2003 at 04:09:29 UT (Vaughan et al. 2004), 22081 s after the detection of the GRB. The afterglow was observed on axis in full frame mode with all three European Photon Imaging Camera (EPIC) instruments (MOS1, MOS2, PN). It was found to be centred at $R.A. = 08^h 02^m 30^s.19$, $decl. = -39°51'04''.0$ (Vaughan et al. 2004). The data used consists of event lists from the three cameras.

A second observation of the afterglow was coincidentally made by the XMM-Newton satellite on December 6, 2003 spanning $54ks$. In this observation another source was centred, so the afterglow of GRB 031203 was close to the CCD edge. This data is used in an attempt to improve my background corrections.

I did the processing and following analysis of the data by use of the XMM-Newton Science Analysis System, the FTOOLS software package, the XSPEC fitting programme (described in Section 1.6) and some IDL programming.

I prepared the data from all three EPIC cameras using the SAS chains producing calibrated event lists.

3.1.1. Filtering the data

The data I used for all later analysis was first filtered using the SAS task *evselect*. A basic filtering must at least be done otherwise the data

will be contaminated with irrelevant events, and the actual sources will be crowded by these. To exemplify this, I made an image from the unfiltered MOS1 event list. The image can be seen in Figure 23. The GRB afterglow is visible but the supposed halo can barely be seen.
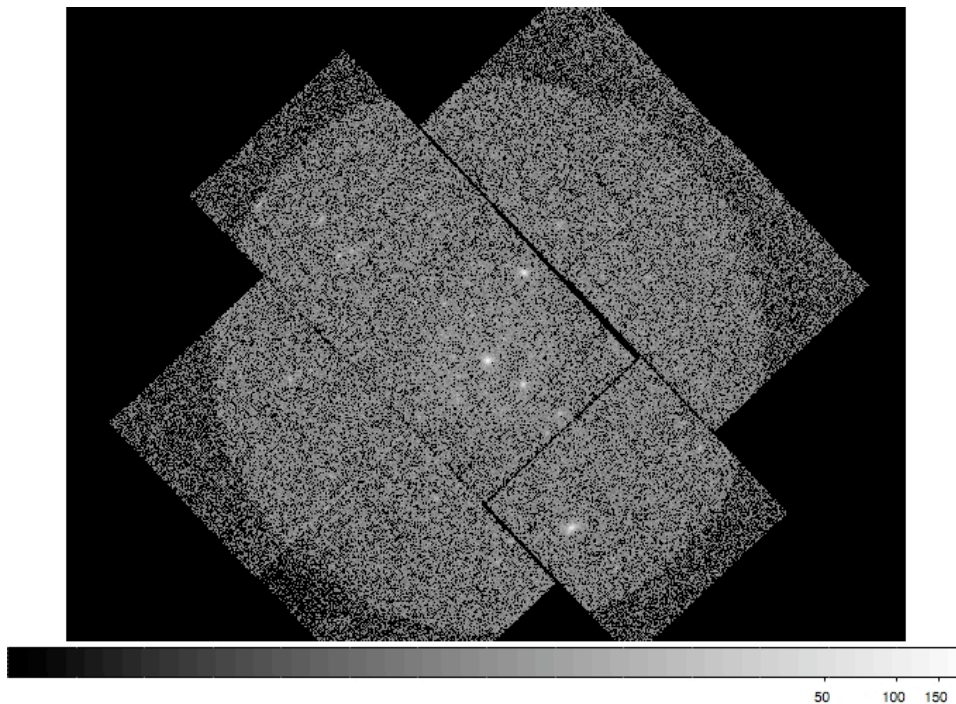
Figure 23. Image from the unfiltered MOS1 event list, the GRB itself is visible but the halo is quite difficult to see. It is clear that filtering is needed.

The basic filtering expression used for the MOS-data was as follows;

$$(Pattern <= 12)\&\&(Pi\ in\ [200:12000])\&\&(Flag == 0) \tag{12}$$

This corresponds to only choosing events with pattern in the range 0 to 12, see fig. 9, with energies in the range from $0.2keV$ to $12keV$ and with a flag value of 0. The pattern values 0 to 12 should exclude irrelevant events caused by cosmic rays and still allow events with overflow caused by high energies, or photons hitting in between pixels, to be included. These pattern values include single, double, triple and quadruple events. The energy range chosen is simply the area where the MOS camera detection is useful, see Figure 8. Using flag=0 means that pixels that are flagged as bad (this was explained in Section 1.5) are not included in the filtered event file.

Equivalently the filtering expression for the PN-data was;

$$(Pattern <= 12)\&\&(Pi\ in\ [200:15000])\&\&(Flag == 0) \tag{13}$$

As above the energy range chosen is the area where the PN camera detection is useful. Using the SAS task *evselect* I produced light curves for the filtered MOS1-, MOS2- and PN-data. This was done to check for irregularities. The flux as a function of time should be approximately constant. If any major disturbances appears in a light curve the corresponding times should be filtered out as bad time intervals. In Figures 24, 25 and 26, the light curves from the MOS1, MOS2 and PN respectively, can be seen. Looking at the light curves we see that they are essentially constant, except from a few anomalies that should not affect the bigger picture[11]. So for the further analysis I chose to use the whole time intervals.

3.2. Photometrical Analysis

First the event files from the two MOS cameras where combined using the task *merge*. This task merges the event list from two exposures. The exposures should preferably be taken in the same mode by the same instrument and it can be necessary to re-project the coordinates to a mean reference point. Even though the event lists are essentially from two different instruments, the two MOS cameras are equivalent and the exposure time and coordinates are the same, so they should be safe to merge without re-projecting the coordinates, and the product should be reliable to use in a photometrical analysis. The merging of these two data sets means that I have a larger data set to found my analysis on, making erroneous data points less significant.

---

[11]   We also see that the rate is higher for the PN light curve than for the two MOS light curves. This is in accordance with the fact that the PN camera receives an unobstructed beam, whereas the MOS cameras receive only 44% of the light from the telescopes, as stated in Section 1.5.

Figure 24. Plot of number of counts per second as a function of time, from the filtered MOS1-data. Containing events in the energy range 0.2-12keV, with pattern values up to 12 and with flag value 0. The bin size is 100 s. The time shown on the x-axis is seconds passed since the beginning of the observation.

3.2.1. Energy ranges

In the further photometrical analysis I was working with two event lists, the filtered and merged MOS event list and the filtered PN event list. Both event files where divided into energy intervals of 1000 eV. For each of these intervals an image was made in order to make comparisons between energy intervals so that the intervals, where the halo is most evident, could be chosen.

The halo seemed to be most apparent in the energy interval from 1000 eV to 2000 eV (second from the left in the top panel of the figures), see Figures 27 and 28.

The energy interval of 2000 eV to 3000 eV had a slight hint of a halo, so this was split in two halves 2000 eV to 2500 eV and 2500 eV to

Figure 25. Plot of number of counts per second as a function of time, from the filtered MOS2-data. Containing events in the energy range 0.2-12keV, with pattern values up to 12 and with flag value 0. The bin size is 100 s. The time shown on the x-axis is seconds passed since the beginning of the observation.

3000 eV. Images were made comparing the two intervals and the first interval, 2000-2500 eV, did show a halo present, see Figures 29 and 30.

The interval of 0 to 1000 eV did not show any real signs of a halo but since it is just below the interval where the halo is seen, I divided the upper part, 500ev-1000ev, into five intervals just to see if this would reveal any clearer features. It did not, see Figures 31 and 32.

So in the following photometrical analysis event lists filtered to only contain events that lie within the energy range $1000eV - 2500eV$ were used.

3.2.2. Counts Versus θ

A nice way to illustrate the growth of an expanding X-ray halo is to divide the data into time slots and then for each time slot make an
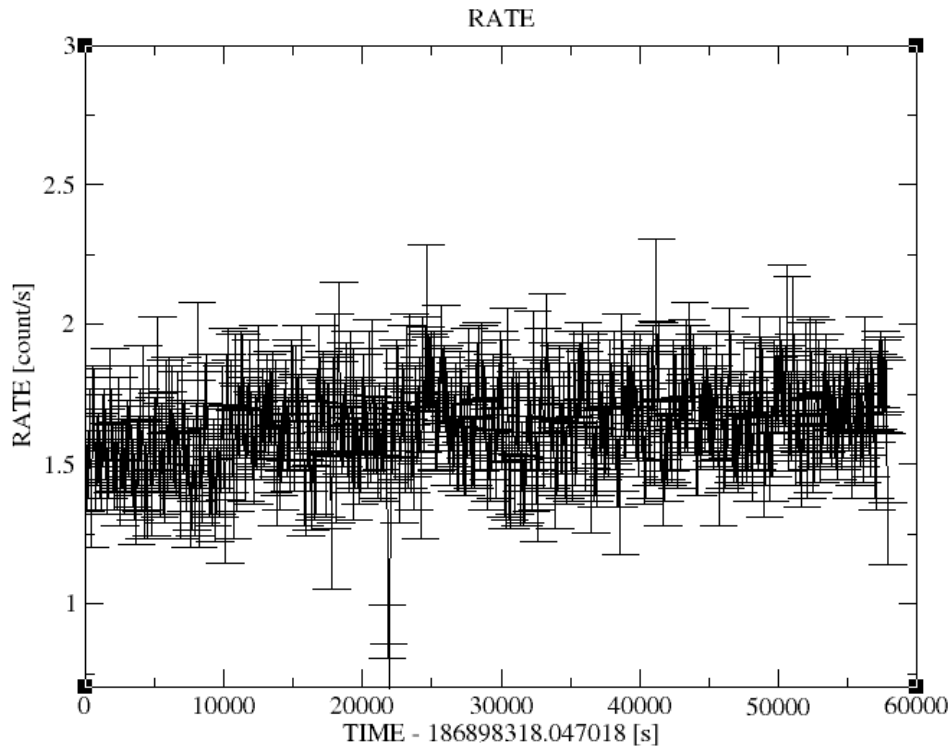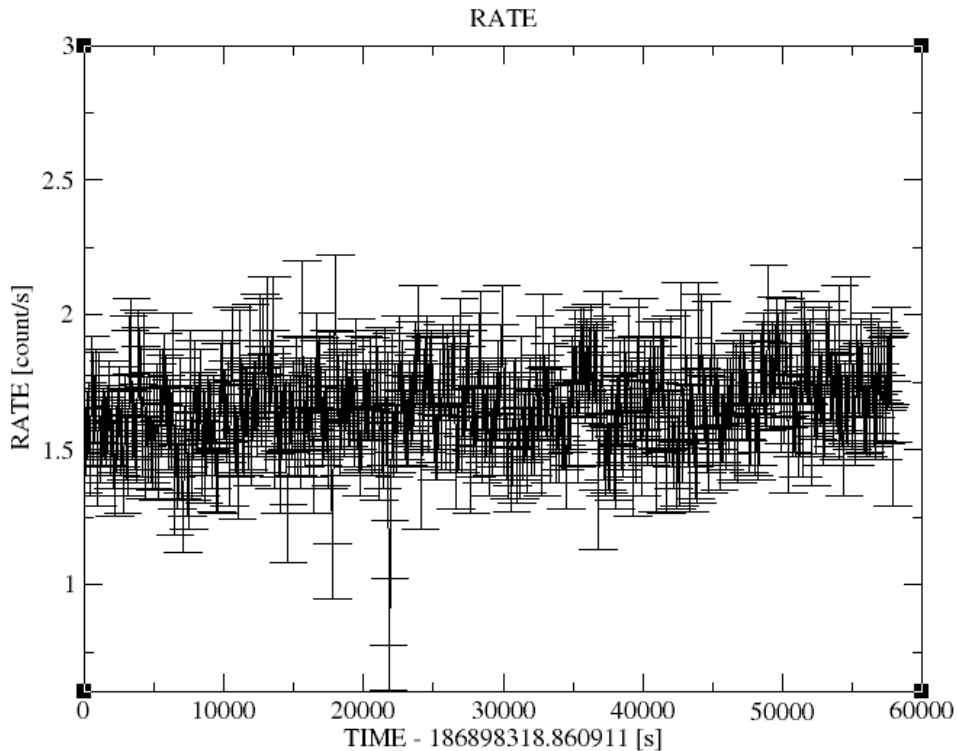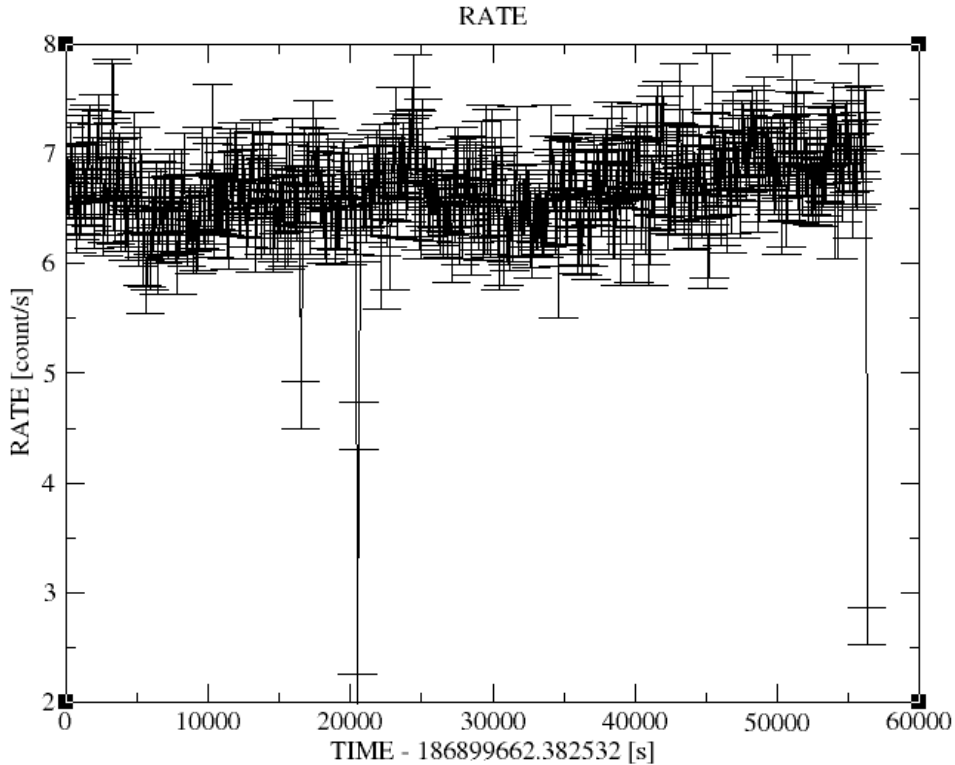
Figure 26. Plot of number of counts per second as a function of time, from the filtered PN-data. Containing events in the energy range 0.2-15keV, with pattern values up to 12 and with flag value 0. The bin size is 100 s. The time shown on the x-axis is seconds passed since the beginning of the observation.

image of the area around the GRB afterglow, as explained in Section 2.3.1. First an image was made, covering the total time, from the two filtered event lists in order to see in which areas the halo was located and if any bright sources were in the halo area, see fig 33. The image revealed that three bright sources were in the halo area. The GRB afterglow and two other point sources. The coordinates found for these three sources, given in sky coordinates, used in all filtering from here on was (26035.930,23654.984) for the GRB centre and (28232,22142) and (28319,29015) for the two other point sources.

The event files were then area filtered in order to get event files containing only events supposedly correlated with the halo. For this, the SAS task *evselect* was used with the filter-expression;

((x,y) in circle(26035.930,23654.984,7000))&&

Figure 27. Image produced from filtered (pattern up to 12 and flag=0) and merged MOS1 and 2 event lists divided into ten energy intervals spanning from $200eV$ to $12000eV$. $(200 - 1000eV, 1000 - 2000eV, 2000 - 3000eV$ and so on) The image binning was 600x600 bins. The image is smoothed using a Gaussian kernel. The halo is clearly most evident in the interval $1000eV$ to $2000eV$.

!((x,y) in circle(26035.930,23654.984,800))&&

!((x,y) in circle(28232,22142,800))&&

!((x,y) in circle(28319,29015,800))

The first line specifies a circle centred at the GRB with a radius of 350" which should include the entire growing halo. The second specifies that a circle centred at the GRB with radius of 40" containing the afterglow should be excluded. The last two specifies that circles centred at the two bright sources in the halo area with radii of 40" should be excluded. An area filtered event file covering an annulus centred at the GRB position, with an inner radius of 350" and an outer radius of 400", were also made for the purpose of applying background corrections to the data.
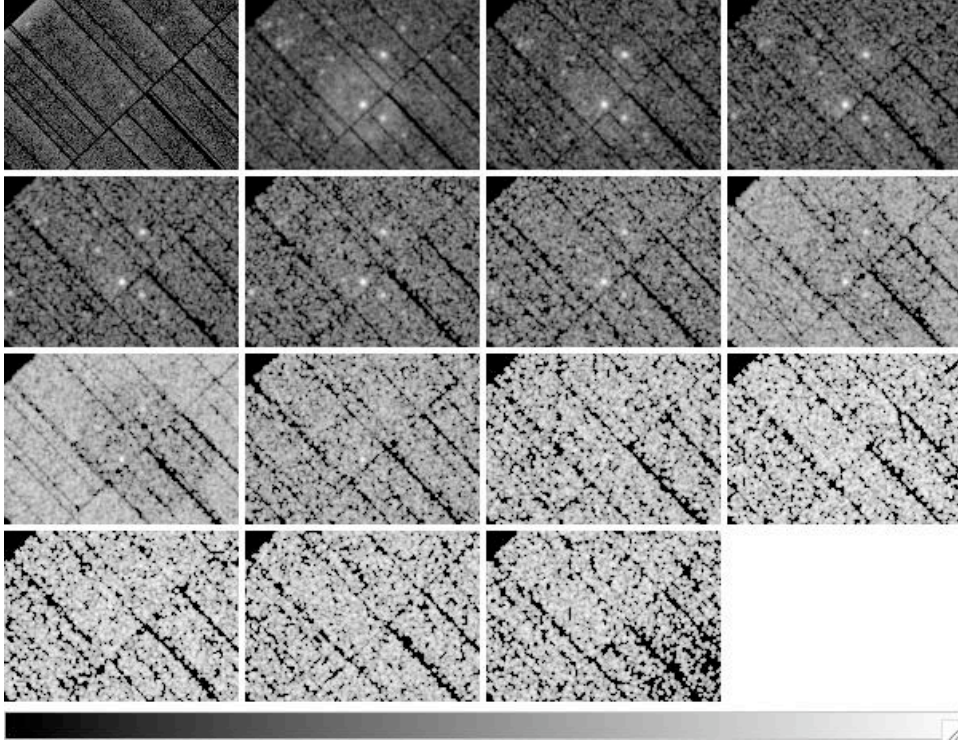
Figure 28. Image produced from filtered (pattern up to 12 and flag=0) PN event list divided into ten energy intervals spanning from $200eV$ to $12000eV$ $(200 - 1000eV, 1000 - 2000eV, 2000 - 3000eV$ and so on). The image binning was 600x600 bins. The image is smoothed using a Gaussian kernel. The halo is clearly most evident in the interval $1000eV$ to $2000eV$.

The area-filtered halo event files were divided into ten subsequent time intervals of $5780s$. For each of these ten intervals, images were made, so as to visualise the growth of the halo, see Figures 34 and 35. In these images we clearly see how the halo grows with time.

My next aim was to get ten subsequent time plots of counts versus θ, showing how the halo evolves through time, as described in Section 2.3.1. Here θ is the angle, measured across the sky, from the position of an event to the centre of the GRB. One way to do this type of plot, is to generate a new column using the FTOOLS task $fcalc$ with the following mathematical expression:

$$\theta^2(arcsec) = (X - X_B)^2 + (Y - Y_B)^2 \qquad (14)$$

Here X and Y are the coordinates of each event and X_B and Y_B are the coordinates for the burst centre. From this column, by the use of

Figure 29. Image produced from the filtered (pattern up to 12 and flag=0) PN event list using the energy interval $2000eV$ to $3000eV$ divided into two halves. The image binning was 600x600 bins. The image is smoothed using a Gaussian kernel. As can be seen, the first of the two halves does show a halo present.

the SAS task *evselect*, I then produced a histogram of counts versus θ with a user-specified binning. This was done for all ten time slots and the events were binned in 3" bins. This was the bin size which gave the most clear plots. From the sample background I made a corresponding histogram and a linear function was fitted to this data in order to get an observationally based model background. This model background was then subtracted from the halo counts and the results could be evaluated. I was not quite satisfied with the resolution of these plots, since the peaks did not stand out clear enough. I spent some time trying different binnings, filtering and background corrections in order to improve clarity of the plots. Using smaller bins the peaks were to flat, if I used larger bins only a few data points would be present in a peak, making it unreliable.

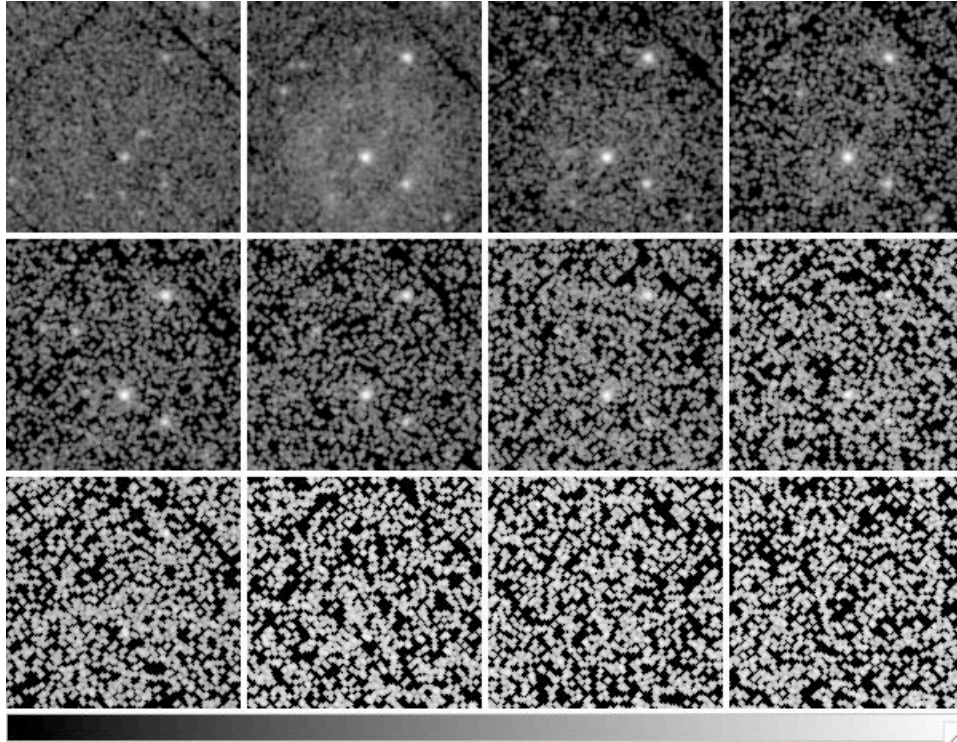**Figure 30.** Image produced from filtered (pattern up to 12 and flag=0) and merged MOS1 and 2 event lists using the energy interval $2000eV$ to $3000eV$ divided into two halves. The image binning was 600x600 bins. The image is smoothed using a Gaussian kernel. As can be seen, the first of the two halves does show a halo present.

As a possible improvement of the plots, I got the idea to use the second observations of the afterglow for an alternative background correction. An image made from a filtered event file clearly shows that the halo has disappeared. We still see the presence of the afterglow and the two other bright sources, although they look a lot dimmer, see Figure 36. Histograms were made in the same way as for the halo, meaning that they were derived from an annulus of inner radius 350" and outer radius 400" with the bright sources cut out. Doing it this way, it did not matter that the sources were dimmer than before. The area used for background is very near the edge of the CCD. This might give some lower values of the background counts at outer radii. Using the FTOOLS task $fdump$ it is possible to write an arbitrary column in the event files into a data file. Using $fdump$, both the halo histogram and the new background histogram was converted into data files
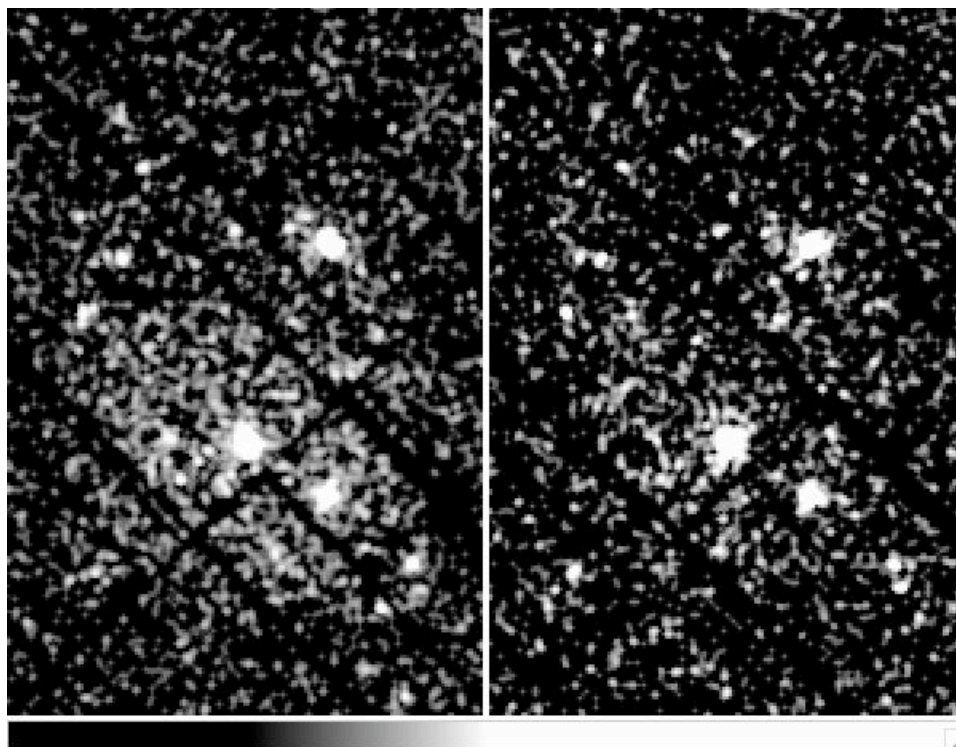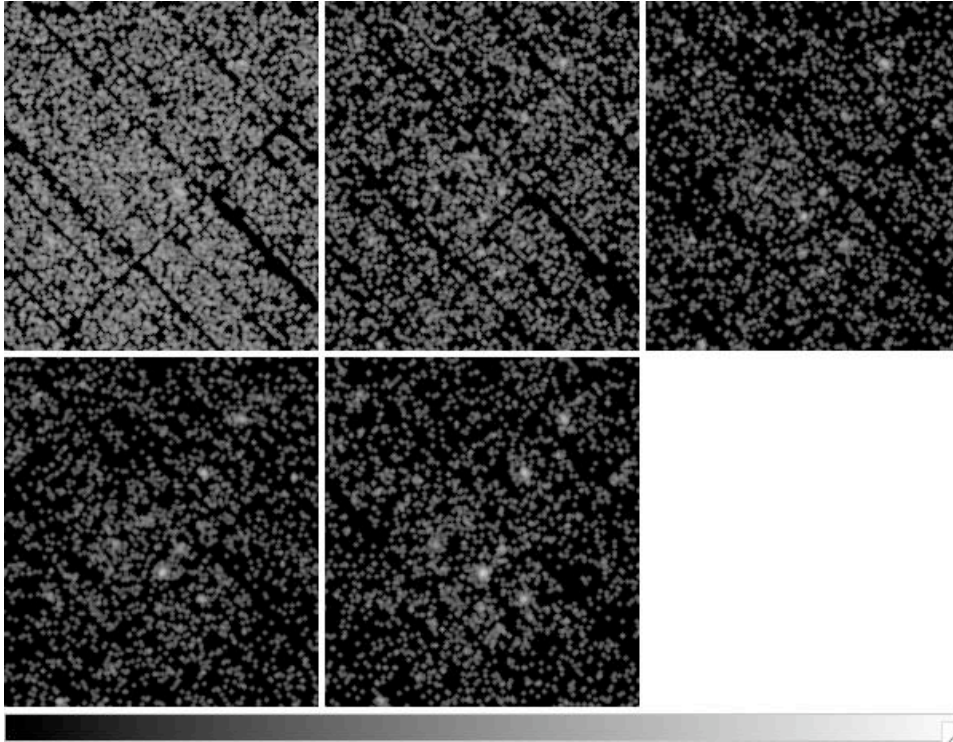
Figure 31. Image produced from the filtered (pattern up to 12 and flag=0) PN event list using the energy interval $500eV$ to $1000eV$ divided into five intervals. The image binning was 600x600 bins. The image is smoothed using a Gaussian kernel. There are no clear features to see here.

containing lists of number of counts and the respective θ values connected. Using IDL I then subtracted the background counts from the halo counts. From this the halo counts could then be plotted in a histogram of counts versus θ. This background correction did not yield any striking improvements in the plots from just using an average modelled background. Other means of improvement had to be explored.

Instead of just using the SAS task *evselect* to produce histograms a slightly different approach was attempted. The X and Y coordinates of all events in each of the ten halo time slots were, using *fdump*, written into 10 data files, each thereby containing a list of coordinates. These data files were then used in an IDL procedure that I made to bin the events and produce a plot of radius vs counts, my IDL code for this procedure is shown in Appendix A.1. In the procedure the event coordinates were converted from sky coordinates into arcseconds (one
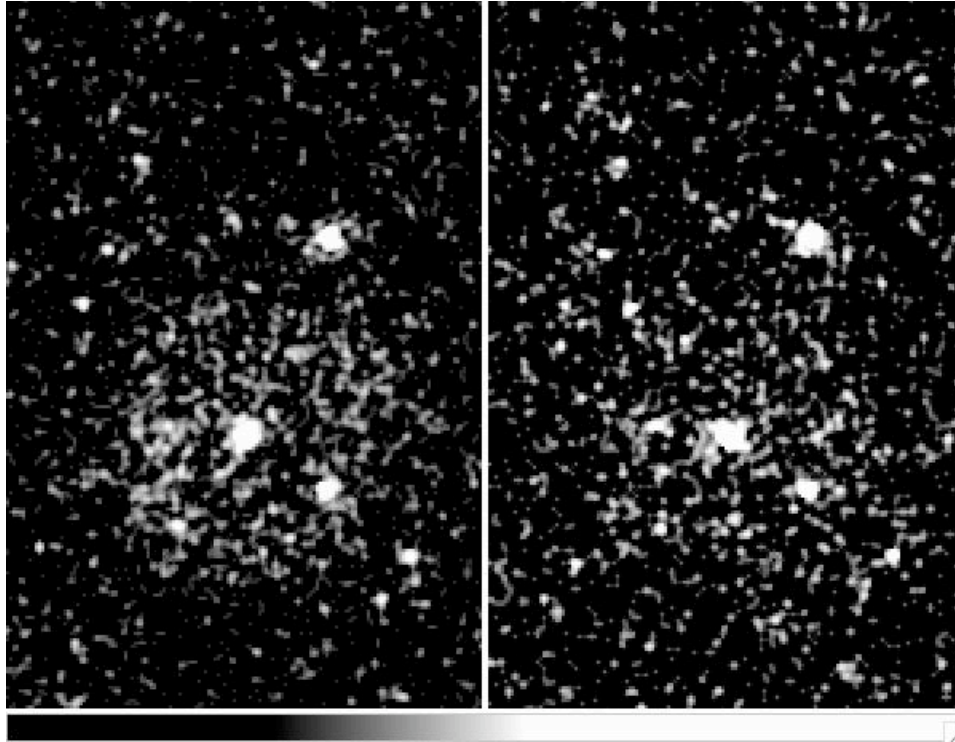
Figure 32. Image produced from filtered (pattern up to 12 and flag=0) and merged MOS1 and 2 event lists using the energy interval $500eV$ to $1000eV$ divided into five intervals. The image binning was 600x600 bins. The image is smoothed using a Gaussian kernel. There are no clear features to see here.

sky coordinate step is 0.05" across) and from each X and Y coordinate set the radial distance across the sky, from the event to the centre of the GRB was calculated from Equation 14.

In order to get a plot of $\theta(arcsec)$ vs counts the data must be binned. The events were placed in bins of 4" width but with only 1" between each bin causing the bins to overlap. The overlapping was done in order to get a clearer picture in the end. In this way I get more data points.

The background event files were converted and binned in the same way as the halo event file. An average background was modelled by fitting the θ vs counts to a linear profile. This was done by use of the standard IDL procedure *curvefit*, which uses a least square fit. This procedure required that I wrote a small script defining the linear function, see Appendix A.2. The resulting linearly fitted background had to be divided by ten, since the background eventlist was gathered from
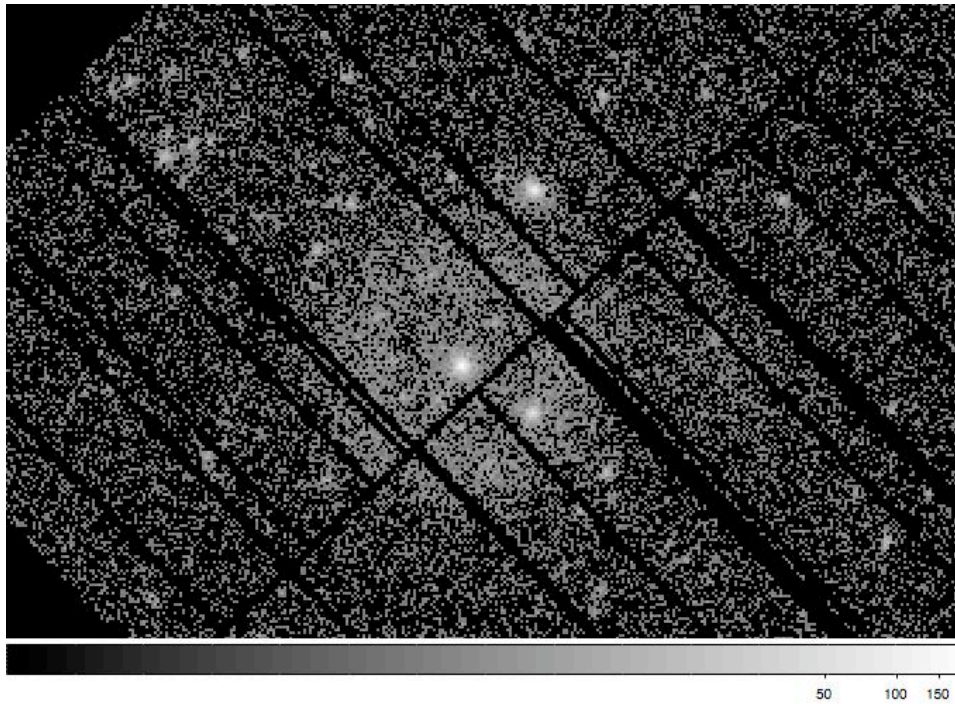
Figure 33. Image produced from the filtered (pattern up to 12 and flag=0) PN eventlist covering only the energy range $1000eV - 2500eV$. The image binning was 600x600 bins. Three bright sources can be seen close to the halo; the afterglow and two other point sources.

the entire exposure time and not divided into 10 intervals as the halo. The background could have been prepared separately for each of the ten time intervals, but since there did not seem to be any time dependent changes in the background, an average over the entire observation time should be better.

The resulting linear fit, representing the modelled average background, was then subtracted from the binned halo events in order to make background corrections and get the pure halo counts. The results are shown in plots of counts vs θ, see Figures 37 and 38. From plots like these we see that the halo actually consists of two rings. These plots were clearer than the ones made using the SAS task to create histograms. The peaks were more well defined and the whereabouts of the two maxima were less unclear, as expected, since the overlap meant that a larger bin size (giving taller peaks) could be used while still not having to few data points.
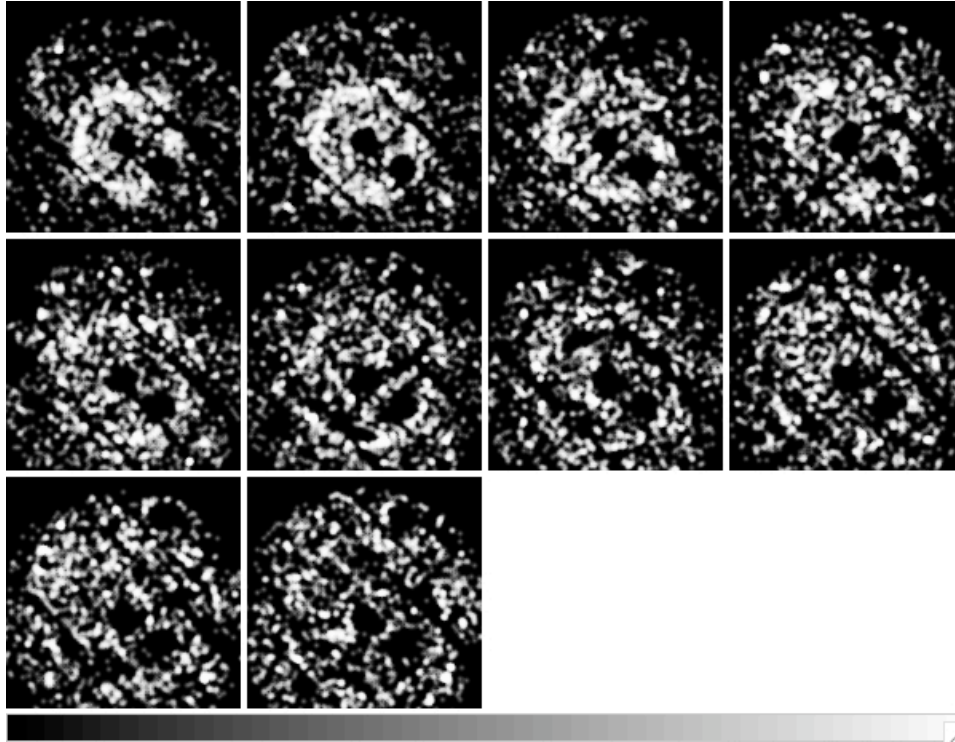
Figure 34. images produced from the filtered (pattern up to 12 and flag=0) PN eventlist covering only the energy range $1000eV - 2500eV$ divided into ten time slots. The image binning was 600x600 bins. The image is smoothed using a Gaussian kernel. It is clearly seen how the halo expands during the ten time intervals.

From the θ vs counts profile for each time slot it was then possible to find two maxima, corresponding to the location of the inner and outer halo in each time slot. In the plots the maxima locations were represented by a red line (I implemented the search for maxima in the IDL procedure (Appendix A.1), producing the count versus θ plots described above). These maxima were written into a data file containing columns with the two ring-locations, the corresponding time[12] and the error estimates for each ring-location. The error was not estimated from the instrumental error of the x- and y-coordinate of each event[13], instead it was estimated from how sharp or flat the peaks were; if a few counts were removed from the peak how far would the maximum

---

[12]   being the mid time of each time interval

[13]   This would give an error estimate too low, since it would not include the effects of erroneous counts from unfiltered background.
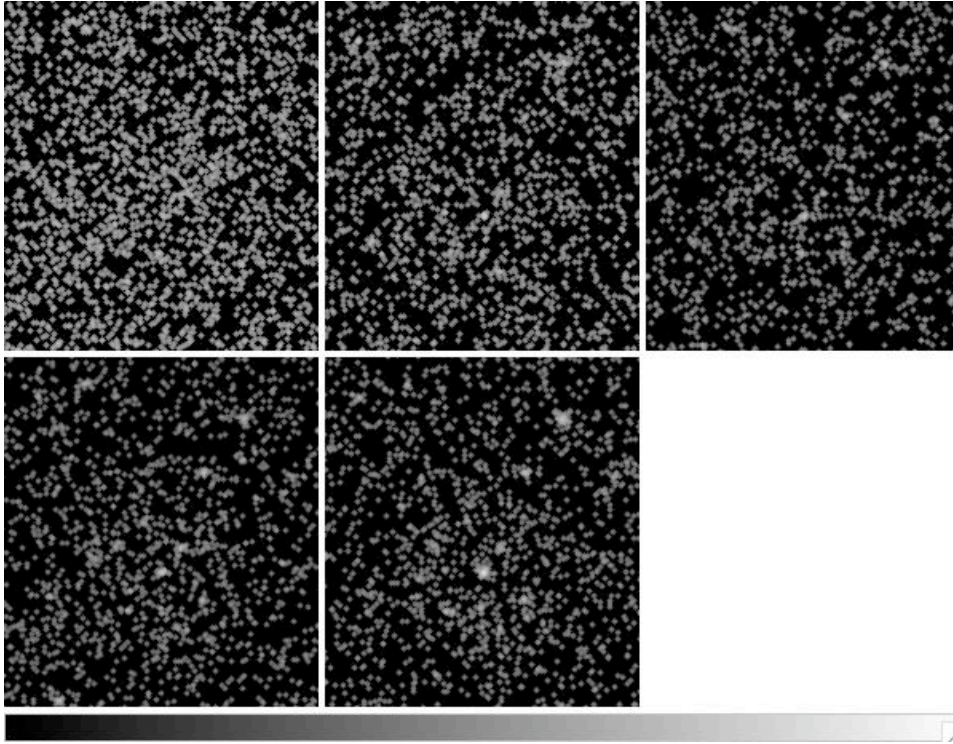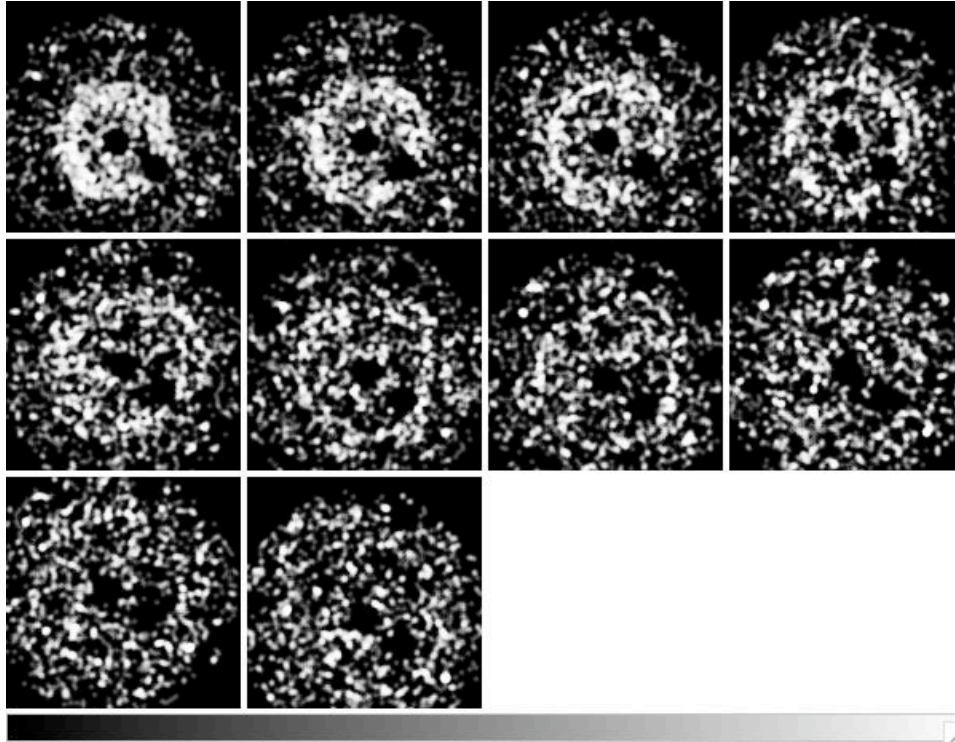
Figure 35. Images produced from filtered (pattern up to 12 and flag=0) and merged MOS1 and 2 event lists covering only the energy range $1000eV - 2500eV$ divided into ten time slots. The image binning was 600x600 bins. The image is smoothed using a Gaussian kernel. It is clearly seen how the halo expands during the ten time intervals.

move? In this way the errors also take into account the effect of erroneous counts from the background. The maxima locations with time and errors can be seen in Tables 1 and 2. We see that through the ten time intervals, the inner halo grows from approximately 120" to 215", while the outer halo grows from approximately 150" to 270".

The halo locations could then plotted as a function of time since the burst, thereby showing how the halo grows with time. According to the derivations in Section 2.3.2 the halo grows as a power-law in time. I therefore made another IDL procedure (shown in Appendix A.3) which plotted the halo evolution and fitted it to a power-law profile;

$$\theta = const \cdot (t - t_0)^{\alpha} \tag{15}$$

For the plot and the fitting, the size of the time slots were used as error estimates for the time values. The fitting was performed by *curvefit*,
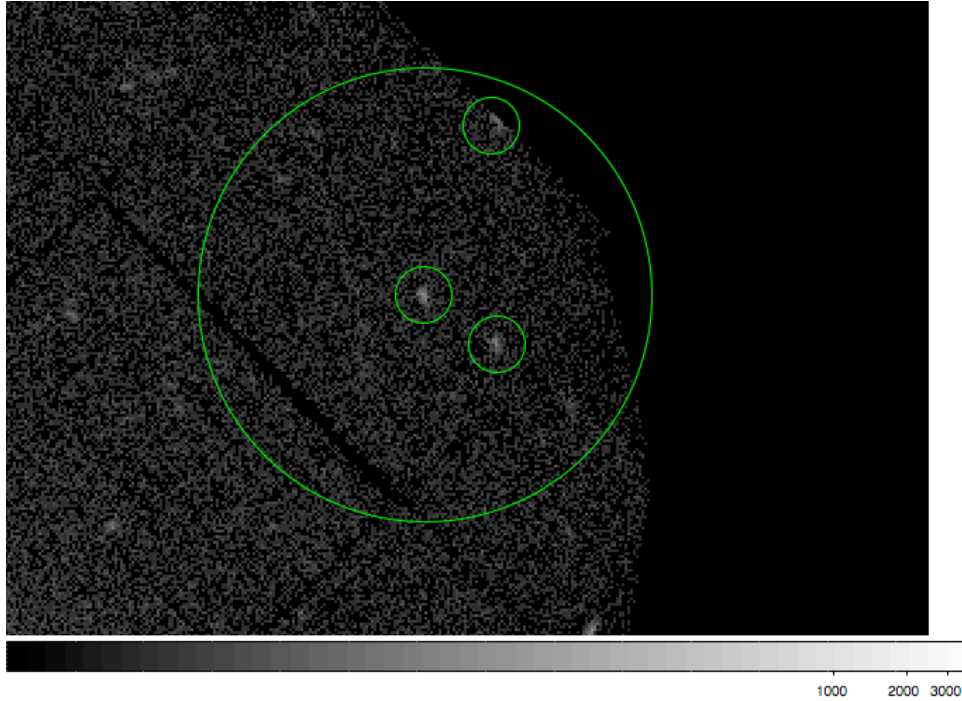
Figure 36. Image made from the merged and filtered (pattern up to 12 and flag=0) MOS1 and 2 event files from the second observation of the area around GRB 031203. The image covers the energy range 1keV to 2.5keV. The large circle represents the area used for background. The small circles enclose the afterglow and the two other sources, all left out of the background event file.

and the weights were set to Gaussian weighing based on the above mentioned errors. The error estimates for the resulting parameters were estimated, by *curve fit*, based on the chosen weights. As before, a function had to be defined through a small script. My script for the power-law can be seen in Appendix A.4.

With t(0) fixed to 0, the parameter α was found to be 0.51 ± 0.03 for the inner halo from both MOS and PN data and for the outer halo found to be 0.50 ± 0.02 from the MOS data and 0.50 ± 0.03 from the PN data. The fitted parameters can be seen in Table 3 and the fitted function are plotted in the Figures 39 and 40. As wee see, the results from the two sets of data were perfectly consistent, thereby confirming their validity.
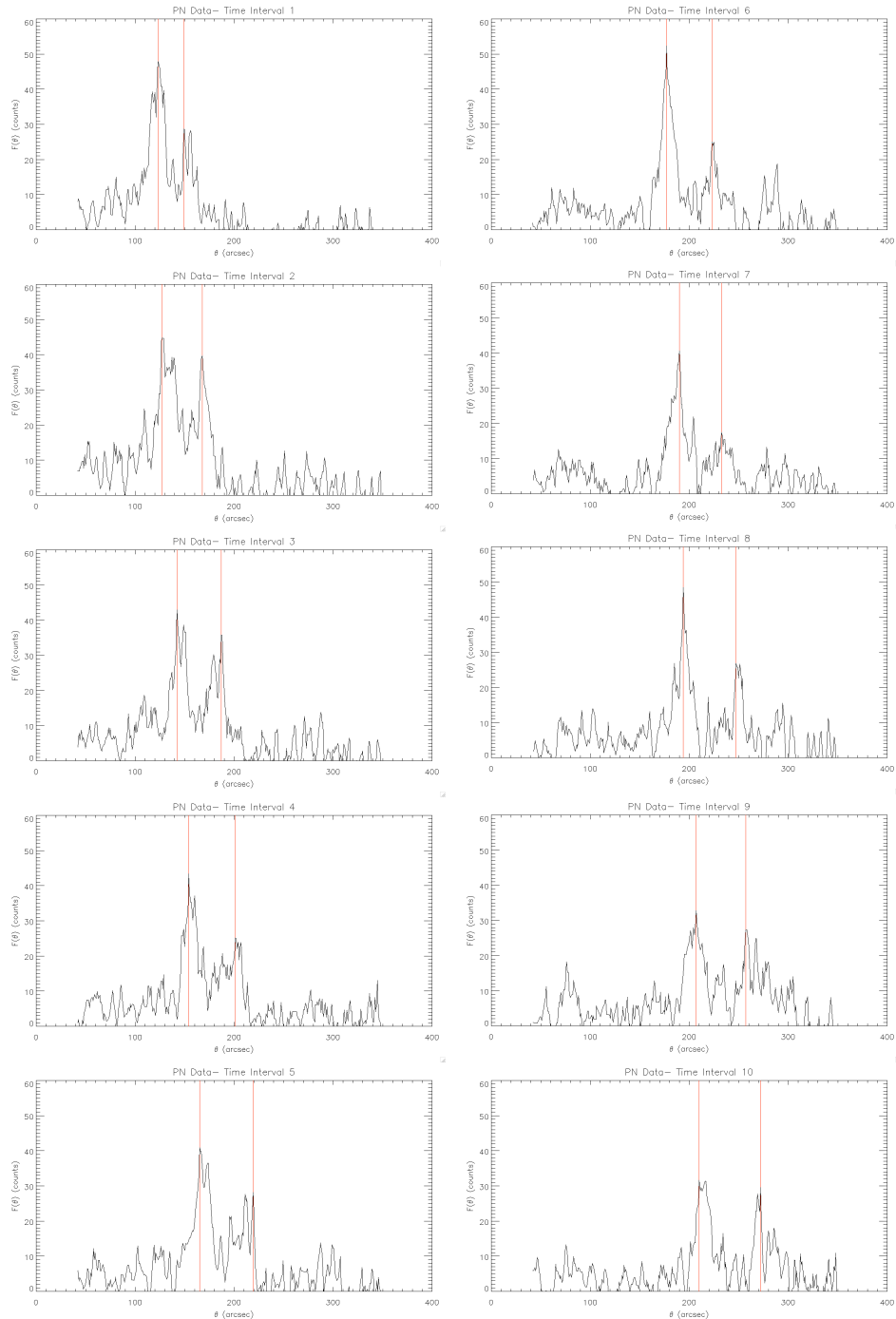
**Figure 37.** Plots of counts versus θ and the two maxima (marked by the red lines), produced from the filtered (pattern up to 12 and flag=0) PN event file covering only the energy range 1 keV to 2.5 keV, divided into ten subsequent time intervals. We clearly see how the two peaks are moving outward through the time plots, indicating that the rings are expanding. The plots are produced by the IDL procedure shown in Appendix A.1.
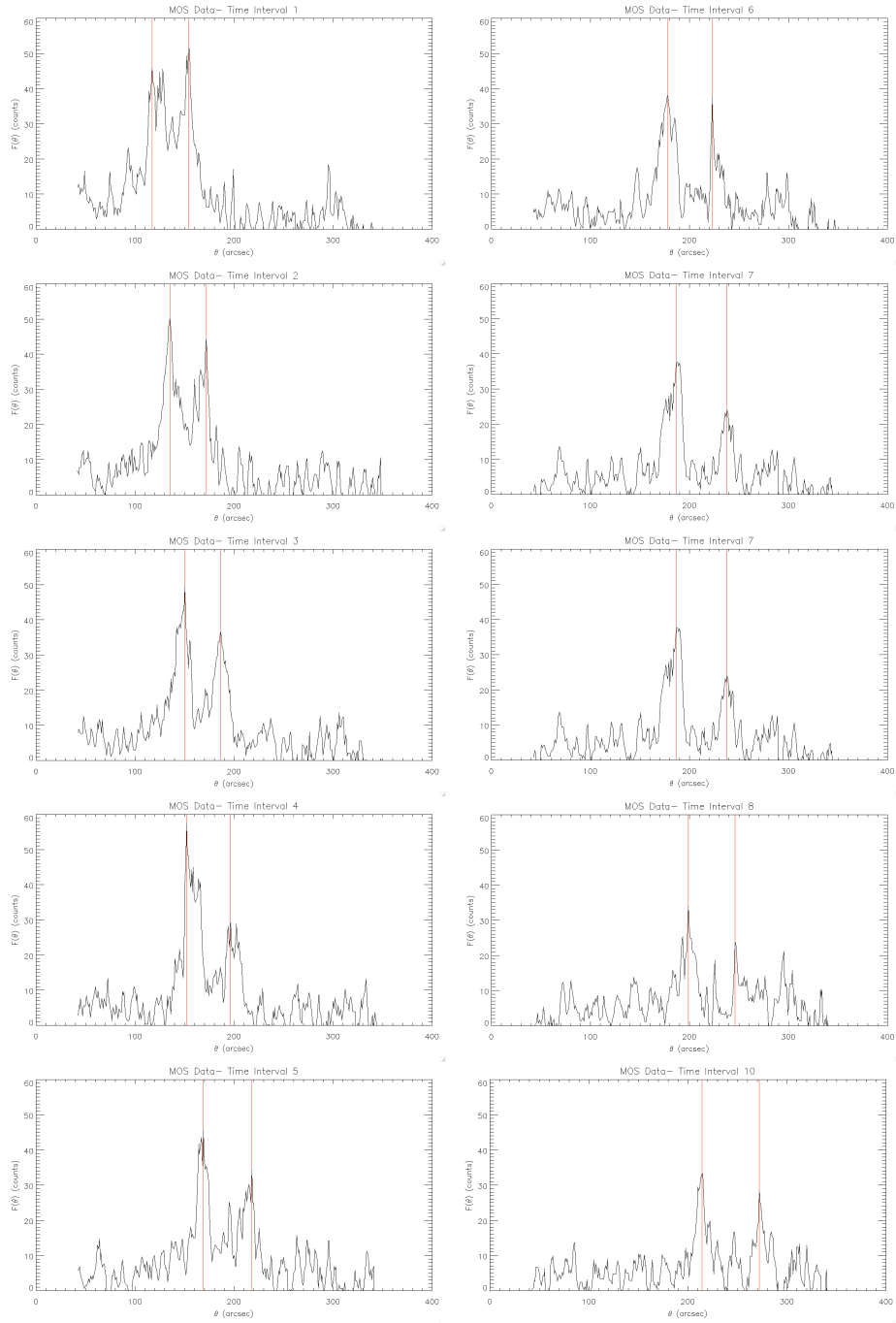
**Figure 38.** Plots of counts versus θ and the two maxima (marked by the red lines), produced from the filtered (pattern up to 12 and flag=0) and merged MOS1 and 2 event files covering only the energy range 1 keV to 2.5 keV, divided into ten subsequent time intervals. We clearly see how the two peaks are moving outward through the time plots, indicating that the rings are expanding. The plots are produced by the IDL procedure shown in Appendix A.1.

	time (s)	Halo 1	Halo 2
1	24971	123" ± 5"	149" ± 7"
2	30751	127" ± 7"	168" ± 4"
3	36531	142" ± 10"	187" ± 7"
4	42311	154" ± 5"	201" ± 7"
5	48091	165" ± 7"	219" ± 10"
6	53871	177" ± 3"	223" ± 4"
7	59651	190" ± 3"	233" ± 7"
8	65431	194" ± 3"	247" ± 7"
9	71211	207" ± 7"	257" ± 10"
10	76991	210" ± 10"	272" ± 7"

Table 1. The whereabouts of the two maxima for each of the ten time intervals, found from the plot in figure 37, are shown together with the estimated errors and the midpoint of the corresponding time interval. Here from the filtered (pattern up to 12 and flag=0) PN data covering the energy range $1 - 2.5keV$. Halo 1 signifies the inner ring and Halo 2 the outer.

	time (s)	Halo 1	Halo 2
1	24971	117" ± 12"	154" ± 5"
2	30751	135" ± 4"	172" ± 3"
3	36531	150" ± 4"	186" ± 4"
4	42311	152" ± 3"	196" ± 7"
5	48091	169" ± 7"	218" ± 7"
6	53871	178" ± 5"	223" ± 3"
7	59651	187" ± 7"	238" ± 5"
8	65431	199" ± 5"	246" ± 5"
9	71211	202" ± 10"	268" ± 10"
10	76991	214" ± 5"	272" ± 3"

Table 2. The whereabouts of the two maxima for each of the ten time intervals, found from the plot in figure 38, are shown together with the estimated errors and the midpoint of the corresponding time interval. Here from the filtered (pattern up to 12 and flag=0) and merged MOS1 and 2 data covering the energy range $1 - 2.5keV$. Halo 1 signifies the inner ring and Halo 2 the outer.

If α is fixed to be 0.5, as required by Equation 10 and agreeing well with my fitted α-values, the distance to the dust slabs responsible for the two haloes can be found from Equation 10 to be;

$$d_d = \frac{2c}{const^2} \tag{16}$$

The constants resulting from this fit yielded distances to the dust slabs of 1416 ± 23 pc for the inner and 883 ± 16 pc for the outer halo from the PN data and 1414 ± 26 pc for the inner and 872 ± 11 pc for the outer halo from the MOS data. The fitting results from the two sets of
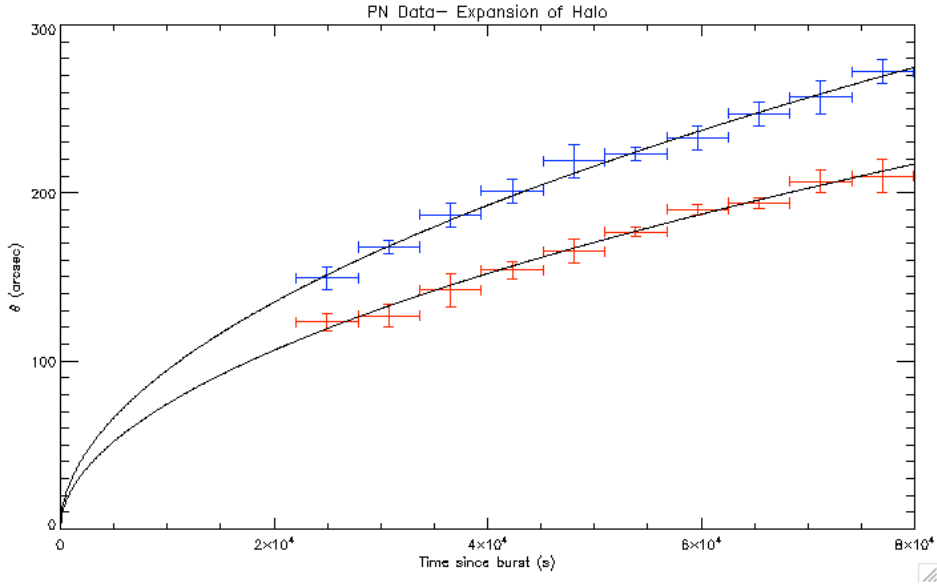
Figure 39. Plot from the filtered (pattern up to 12 and flag=0) PN data covering the energy range 1keV to 2.5 keV, showing the evolution of the halos as a function of time, with the fitted power-law profile. Here α was kept free and t_0 was kept locked to 0 (see Table 3 for fitted parameters). Here the red represents the inner halo and the blue represents the outer halo. The plot is produced by the IDL procedure shown in Appendix A.3.

data were again consistent. The fitted parameters can again be seen in Table 3. The resulting new plots did not look very different from the previous plots, see Figures B.1 and B.2 in Appendix.

As a consistency check, a fit where t_0 was kept as a free parameter, was made. The parameter α was again fixed to 0.5 and the constant was again kept free. From this the values for t_0 were found to be $966s \pm 1586s$ for the inner and $76s \pm 460s$ for the outer halo from the MOS data and $982s \pm 1566s$ for the inner and $406s \pm 675s$ for the outer halo from the PN data. These values are perfectly consistent with $t_0 = 0$, as was assumed above, see Table 3. The resulting new plots did not look very different from the previous plots, see Figures B.3 and B.4. All the distances derived from the fits in this section are gathered in Table B.1 in Appendix.
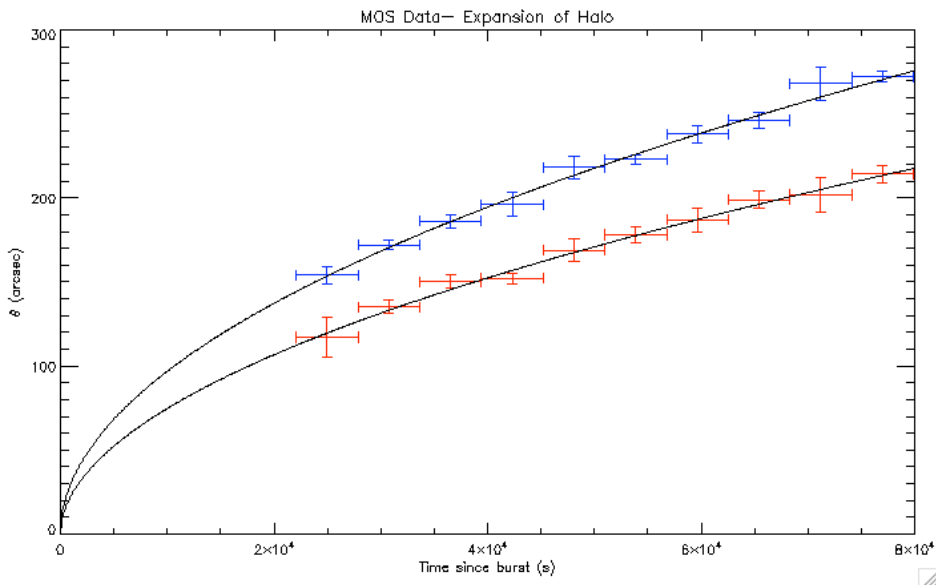
Figure 40. Plot from the filtered (pattern up to 12 and flag=0) and merged MOS1 and 2 data covering the energy range 1keV to 2.5 keV, showing the evolution of the halos as a function of time, with the fitted power-law profile. Here α was kept free and t_0 was kept locked to 0 (see Table 3 for fitted parameters). Here the red represents the inner halo and the blue represents the outer halo. The plot is produced by the IDL procedure shown in Appendix A.3.

3.2.3. Counts Versus Distance to the Dust

Another way to illustrate the growth of the halo is to make a dynamical image; a two dimensional histogram, where each event is binned according to the squared distance from burst centre and the time since the beginning of the burst, as explained in Section 2.3.1. Using the FTOOLS task $fcalc$, I performed the following two mathematical calculations, to give two new columns in the filtered event files.

$$\theta^2(arcsec) = ((X - X_B)^2 + (Y - Y_B)^2) \cdot 0.05^2 \tag{17}$$

$$T_{new} = T_e - T_0 + (T_{XMM} - T_B) \tag{18}$$

Giving respectively, the squared distance across the sky from the event to the GRB centre in arcseconds and the time passed since the GRB was detected to the event occurred. Here X and Y are the coordinates of each event, X_B and Y_B are the coordinates for the burst centre and the factor 0.05^2 is present in order to convert θ from sky-coordinates into arcseconds.

	α	$const$	t_0		α	$const$	t_0
MOS				PN			
Halo 1				Halo 1			
t_0 locked	0.51	0.7	0	t_0 locked	0.51	0.7	0
	±0.03	±0.2			±0.03	±0.2	
α and t_0 locked	0.5	0.765	0	α and t_0 locked	0.5	0.764	0
		±0.007				±0.006	
α locked	0.5	0.772	966	α locked	0.5	0.771	982
		±0.014	±1586			±0.012	±1566
Halo 2				Halo 2			
t_0 locked	0.503	0.94	0	t_0 locked	0.51	0.8	0
	±0.018	±0.18			±0.03	±0.3	
α and t_0 locked	0.5	0.974	0	α and t_0 locked	0.5	0.966	0
		±0.006				±0.009	
α locked	0.5	0.975	76	α locked	0.5	0.978	1159
		±0.005	±461			±0.007	±2322

Table 3. The resulting parameters from fitting the filtered PN and the merged and filtered MOS data (pattern up to 12 and flag=0), covering the interval from $1 - 2.5 keV$. Halo 1 signifies the inner peaks and Halo 2 the outer. Different parameters are locked and kept free, for three different fits.

The original time column in the event file starts at some number of seconds and counts from there, so the T_0 represents the time coordinate that the first event in the observation has, the T_e represents the time that an event has in this time line, T_{XMM} represents the real time that the XMM observation was started and the T_B represents the real time at which the GRB was detected. From Section 3.1 we have that the difference between the GRB detection time and the XMM-observation start time is $22081s$. In the event files the time starts at $186898000s$. So our new time column will therefore be,

$$T_{new} = T_e - 186898000s + 22081s \tag{19}$$

With these new columns it was possible to make a two dimensional histogram, with T on the x-axis, θ^2 on the y-axis and number of counts giving the level of each bin in the histogram. In such an image any luminous object not changing in time will appear as a horizontal line. A ring that expands with time and is centred on the GRB position will be seen as an inclined line. The angular coefficient of the inclined

line will then be inversely proportional to the distance of the dust, see Equation 10.

Looking at the images produced we clearly see an inclined line representing the growing halo around the GRB afterglow, see Figures 41 and 42. At the bottom of the image we also clearly see the very dark horizontal line representing the GRB afterglow itself.
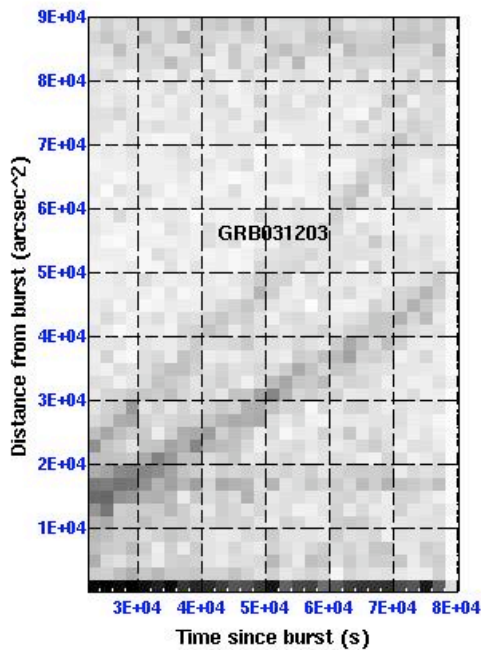
Figure 41. Dynamical image or two dimensional histogram, of T_{new} versus $\theta(arcsec)^2$, made from the filtered PN event list (pattern up to 12 and flag=0), representing only the events lying in the energy range $1000eV - 2500eV$. The image binning was set to 3000x3000 bins. We clearly see the inclined lines representing the growing halos.

From these two new columns it was also possible to calculate an additional column representing the distance from the observer to where the photon causing the event was scattered, assuming that the photon in question does come from the GRB afterglow originally. From this we can thereby infer the distance to the dust slabs responsible for the haloes, as explained in Section 2.3.3. From Equation 9 the expression
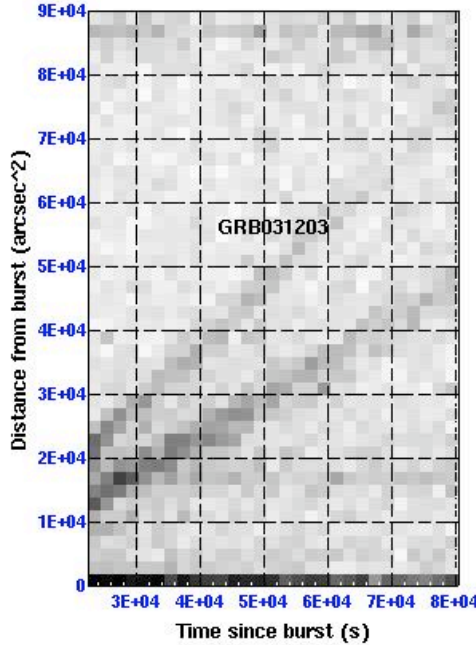
Figure 42. Dynamical image or two dimensional histogram, of T_{new} versus $\theta(arcsec)^2$, made from the filtered and merged MOS1 and 2 event lists (pattern up to 12 and flag=0), representing only the events lying in the energy range $1000eV - 2500eV$. The image binning was set to 3000x3000 bins. We clearly see the inclined lines representing the growing halos.

for the new column becomes;

$$d_i(pc) = 2c[pc/s]\frac{T_{new}}{\theta(arcsec)^2} = 827\frac{T_{new}}{\theta(arcsec)^2} \tag{20}$$

Here $c[pc/s]$ is the speed of light given in parsecs per second. My aim was to make a plot of this distance vs counts/pc. In order to do this I had to choose a binning for the counts. In this case the counts where binned so that each bin contained 100 counts. I did this by writing a procedure in IDL, see Appendix A.5. The FTOOLS task $fsort$ was used in order to get the events sorted according to the new $d_i(pc)$ column and the task $fdump$ was used to write the new sorted column into a data file. This file was read into the IDL procedure which then binned the events so that each bin contained 100 counts. The procedure then calculated for each bin the number of counts per pc. From this a plot was made of D(pc) versus counts/pc. The D(pc) value here

represents the average distance for the counts in the relevant bin. The plot showed points following a declining line with two peaks in the middle representing the two dust slabs. The data was then fitted to a power-law plus two Lorentzians, as discussed in Section 2.3.3, only using the events with distance between 200 pc and 5000 pc. Outside this range the power-law is not fulfilled since these areas correspond to the edges of the CCD. The function fitted to was:

$$f(x) = cx^a + L_1 + L_2 = cx^a + \left(\frac{I_1 \cdot \gamma_1^2}{(x-x_{01})+\gamma_1^2}\right) + \left(\frac{I_2 \cdot \gamma_2^2}{(x-x_{02})+\gamma_2^2}\right) \qquad (21)$$

the locations of the Lorentzians (x_{01} and x_{02}) then represent the whereabouts of the dust slabs. For the plot and the fitting, the error estimates for number of counts per pc and distance in pc are described in the paragraph about error estimates below. The fitting in my procedure was performed by $curvefit$, and my script, defining the function for fitting, can be seen in Appendix A.6. The weights were set to Gaussian weighing based on the errors described below. The error estimates for the resulting fitted parameters were estimated, by $curvefit$, based on the chosen weights. The plotted data with the model can be seen in Figures 43 and 44 and the fitted parameters can be seen in Table 4. The results are discussed below in the last paragraph in this section.

3.2.3.1. Error Estimates

The error estimate for D(pc), the average distance for a given bin, can from the law of error propagation be derived to be;

$$\sigma_D = \frac{\sqrt{\sigma_{d_1}^2 + \sigma_{d_2}^2 + \sigma_{d_3}^2 .... + \sigma_{d_{100}}^2}}{100} \qquad (22)$$

Here σ_{d_1} represents the error on the distance to the first count in the bin, σ_{d_2} the second and so on. The error would be less than the average of the errors and it would differ for each bin. A check was made of what order of magnitude the σ_{d_n}'s (n being 1,2,3...,100) would give. From the law of error propagation the error estimate for the distance, in Equation 20, of a specific event taking place at (x, y), at the time t

would be;

$$\sigma_{D_i} = 827 \cdot t \cdot xysize \cdot 2(x^2 + y^2)^{-3/2} \tag{23}$$

the $xysize$ enters as the error estimate of the x- and y-coordinate. For the MOS this is 1.1", and for the PN this is 3.3", see Section 1.5. For any event, I found that the error on the distance had an order of magnitude $\approx 10^{-1}$. This is an insignificant number compared to the size of the distances calculated which have magnitudes of the order $10^2 - 10^3$, and the actual error on the distance to a bin, Equation 22, would be even less. Therefore I chose to disregard the errors for the distance to the bins.

The number of counts per pc is given by the number of counts in a bin, divided by the average distance to the counts in that bin. In finding the error for counts per pc, the law of error propagation was again used giving the following expression.

$$\sigma_{c/pc} = \sqrt{\left(\frac{1}{binsize}\sigma_c\right)^2 + \left(\frac{counts}{binsize^2}\sigma_{binsize}\right)^2} \tag{24}$$

Here σ_c is the error estimate on the number of counts in a bin which from counting statistics is $\sqrt{100}$, since there are 100 counts in a bin. The binsize is the difference between first and last count in a bin given in pc. From looking at the data the binsize goes from $\approx 1pc$ at 200 pc, $\approx 3pc$ at 300 pc and $\approx 6pc$ at 500 pc to $\approx 400pc$ at 5000 pc. $\sigma_{binsize}$ is the error estimate for the width of the bin, which can be estimated as the sum of the errors on the distance to the first and last count in a bin. The error on the distance to one event was above evaluated to be of the order 10^{-1}, so the binsize error will be approximately of this order. The error on the counts/pc then becomes;

$$\sigma_{c/pc} = \frac{\sqrt{100}}{binsize} \cdot \sqrt{1 + \frac{10}{binsize^2}} \tag{25}$$

At 200 pc, the square root will yield $\sqrt{1 + 10}$, at 300 pc it will yield $\sqrt{1 + 1.11}$, at 500 pc it will yield $\sqrt{1 + 0.28}$ and at 5000 pc $\sqrt{1 + 0.6 \cdot 10^{-4}}$. I chose to neglect the last term in the square root,

when estimating the errors through the fitted interval. Neglecting the last term will mean a lack in error of $\approx 230\%$ at 200 pc, $\approx 40\%$ at 300 pc, $\approx 13\%$ at 500 pc, and $\approx 10^{-5}\%$ at 5000 pc. Since the Lorentz peaks are located around a 1000 pc it is not that important if the error bars are too low around a few hundred pc. We see that neglecting the last term is acceptable above 500 pc. If the full errors were to be included, they would have to be calculated individually for each bin, a lot of work to do when taking into account that the actual effect on the x_0 values, the parameter of most interest, would be insignificant. The error to be used, in the analysis, for the number of counts per pc was thereby;

$$\sigma_{c/pc} = \frac{\sqrt{100}}{binsize} \qquad (26)$$

3.2.3.2. Fitting results

The values for the distance to the dust slabs, resulting from the above fitting, was from the PN data; $1353 \pm 5pc$ for the inner and $839 \pm 3pc$ for the outer halo, and from the MOS data; $1392 \pm 5pc$ for the inner and $870 \pm 3pc$ for the outer halo. The values between the two cameras are not consistent. In hope of getting better result the same procedure was followed for event lists, where instead of only excluding events with pattern above a value of 12, events with pattern value above 4 was excluded. Pattern values up to 4 include only single and double events, this might provide less noisy data, thereby improving the results. The rest of the treatment was equivalent. This gave results for the distance from the PN data $1403 \pm 5pc$ for the inner and $871 \pm 3pc$ for the outer halo and for the MOS data $1390 \pm 5pc$ for the inner and $870 \pm 3pc$ for the outer halo, the plotted data with the model can be seen in Figures 45 and 46, the fitted parameters can be seen in Table 5. The effect of changing the allowed pattern values is very noticeable with the PN data results but for the MOS data the results are almost the same. The consistency between the results for the two cameras are clearly better, it is now only the results from the inner halo which do not agree but comes very close.

	PN	MOS
c	516923 ± 35035	606090 ± 41075
α	-1.694 ± 0.011	-1.711 ± 0.011
I_1	7.3 ± 0.7	8.8 ± 0.7
I_2	5.7 ± 0.3	5.7 ± 0.3
γ_1	37 ± 4	35 ± 3
γ_2	108 ± 7	108 ± 7
x_{01}	839 ± 3	870 ± 3
x_{02}	1353 ± 5	1392 ± 5
red χ^2	1.302	1.691
$\mathcal{L}_1$	844 ± 101	962 ± 121
$\mathcal{L}_2$	1893 ± 160	1891 ± 136

Table 4. Fitted parameters for counts/pc versus distance. Here c is the power-law constant, α is the power-law index. For the two Lorentzians I_1 and I_2 are the intensity or the height of peak, γ_1 and γ_2 are the half width half maxima and x_{01} and x_{02} are the locations of the peaks, i.e. the distance to he dust slabs. $\mathcal{L}_1$ and $\mathcal{L}_2$ are the integrated Lorentzians. For the PN data the number of points used in the fitting was 196 and for the MOS data it was 207. The reduced chi-squared is also given. The data was filtered including pattern values up to 12, energies in the range $1 - 2.5 keV$ and flag=0. Subscript 1 parameters belongs to the outer ring and subscript 2 to the inner ring.
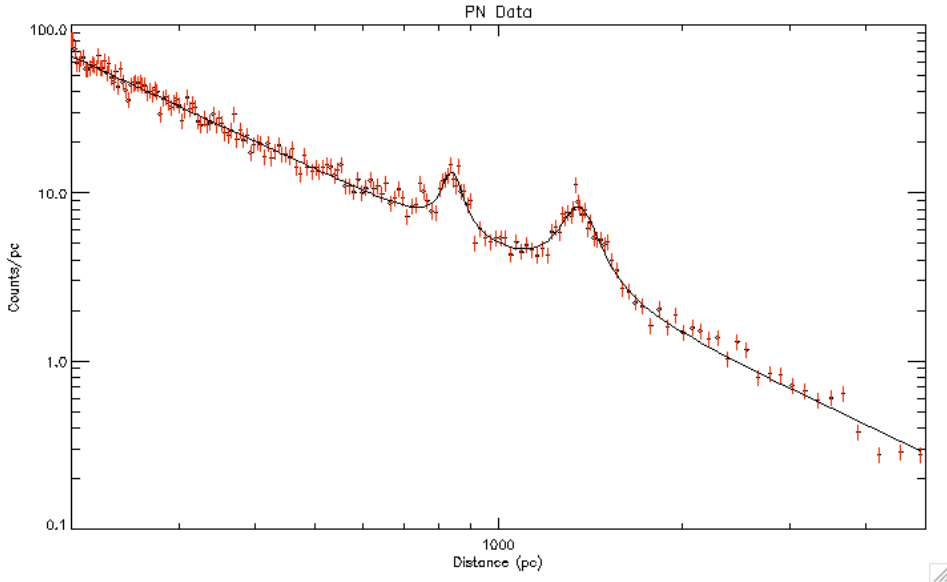
Figure 43. The filtered PN data, covering the energy range $1 - 2.5 keV$, with pattern values up to 12, presented in a plot of counts/pc as a function of the distance to where the photons were scattered, with the fitted power-law plus two Lorentzians. The fitted parameter values can be seen in Table 4. The plot is produced by the IDL procedure seen in Appendix A.5.

Comparing these distances to the ones derived from the θ vs time plots, see Table B.1, we see that with the pattern values running up to 12, the MOS data yields distances that are consistent with the earlier
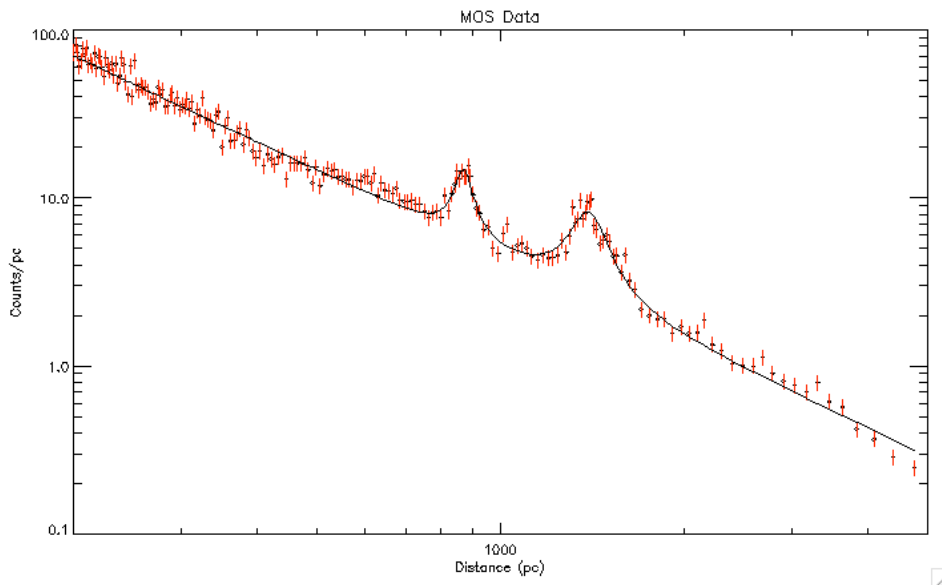
Figure 44. The filtered and merged MOS1 and 2 data, covering the energy range $1-2.5keV$, with pattern values up to 12, presented in a plot of counts/pc as a function of the distance to where the photons were scattered, with the fitted power-law plus two Lorentzians. The fitted parameter values can be seen in Table 4. The plot is produced by the IDL procedure seen in Appendix A.5.

results but the PN data does not. With the new filtering where we only allowed pattern values up to 4, the results are consistent for both the PN and the MOS data.

In Table 5 we also see the fitted parameter γ which corresponds to the half-width-half-maximum of the Lorentzian. The FWHM are, from the MOS data for the inner halo $218 \pm 16pc$ and for the outer halo $70 \pm 8pc$ and from the PN data for the inner halo $224 \pm 16pc$ and for the outer halo $78 \pm 10pc$. These values are compatible with the expected values of 100 pc and 200 pc caused by the instrumental point spread function of 6" for the PN (Tiengo & Mereghetti 2006). For the MOS cameras the point spread function is 5", so we should expect a slightly smaller peak width for the MOS. Looking at the FWHM we see that this is the case here. The fact that the FWHM are of approximately the size expected from the point spread function alone indicates that the two dust slabs are quite thin.

By integrating the two Lorentzians I could also find the net number of halo counts in each halo/peak. The integrated Lorentzian evaluated

	PN	MOS
c	495607 ± 34010	602912 ± 41621
α	-1.687 ± 0.011	-1.714 ± 0.011
I_1	6.8 ± 0.6	8.5 ± 0.7
I_2	5.4 ± 0.3	5.6 ± 0.3
γ_1	39 ± 5	35 ± 4
γ_2	112 ± 8	109 ± 8
x_{01}	871 ± 3	870 ± 3
x_{02}	1403 ± 5	1390 ± 5
$red\ \chi^2$	1.302	1.620
$\mathcal{L}_1$	819 ± 118	930 ± 120
$\mathcal{L}_2$	1837 ± 156	1857 ± 159

Table 5. Fitted parameters for counts/pc versus the distance. Here c is the power-law constant, α is the power-law index. For the Lorentzians I_1 and I_2 are the intensity or the height of peak, γ_1 and γ_2 are the half width half maxima and x_{01} and x_{02} are the locations of the peaks, i.e. the distance to the dust slabs. $\mathcal{L}_1$ and $\mathcal{L}_2$ are the integrated Lorentzians. For the PN data the number of points used in the fitting was 195 and for the MOS data it was 202. The reduced chi-squared is also given. The data was filtered to only include events with pattern values up to 4, energies in the range $1 - 2.5 keV$ and flag=0. Subscript 1 parameters belongs to the outer ring and subscript 2 to the inner ring.

from 0 to infinity becomes;

$$\mathcal{L} = \frac{(\gamma \cdot tan^{-1}(\frac{X_0}{\gamma}) + \gamma\pi)}{2} \tag{27}$$

Using this expression the pattern 4 restricted MOS data yielded 1857 ± 160 counts for the inner halo and 930 ± 120 counts for the outer halo. The pattern 4 restricted PN data yielded 1837 ± 156 counts for the inner halo and 819 ± 118 counts for the outer halo[14]. The high number of counts in the peaks verify that the peaks are more than just noise.

3.3. Spectral Analysis

The filtered PN event file and the filtered MOS2 event file, filtering described in Section 3.1.1, were used. The files where area filtered to make a halo event file, a background event file and an afterglow event file. In the halo event file I only included the area where the halo was visible; an annulus within inner radius of 110" and outer radius of 220"

---

[14] The error estimates were found from the law of error propagation

Figure 45. Plot from the filtered PN data, excluding events with pattern values above 4, covering the energy range $1 - 2.5keV$ of counts/pc as a function of the distance to where the photons were scattered, together with the fitted power-law plus two Lorentzians. The plot is produced by the IDL procedure seen in Appendix A.5.

centred at the GRB position. The background event file contained a sample background area taken from an off-axis region at the point (28493,36149), with a radius of 325″ . In the afterglow event file I only included a small area centred at the GRB position, with a radius of 40″.

In order to avoid the times where the halo becomes more faint and distorted (here it can be difficult to distinguish from background objects), the later half of the total observation was excluded from the halo event file by doing a time filtering with the SAS task *evselect*.

The spectra was then extracted from the different event files: the background event files (both half time background sample and full time background sample to be used for the halo spectrum and the afterglow spectrum respectively), the halo event files and the afterglow event files. A redistribution matrix file and an ancillary response file for all halo spectra and all afterglow spectra were made using the SAS tasks *rmfgen* and *arfgen*.

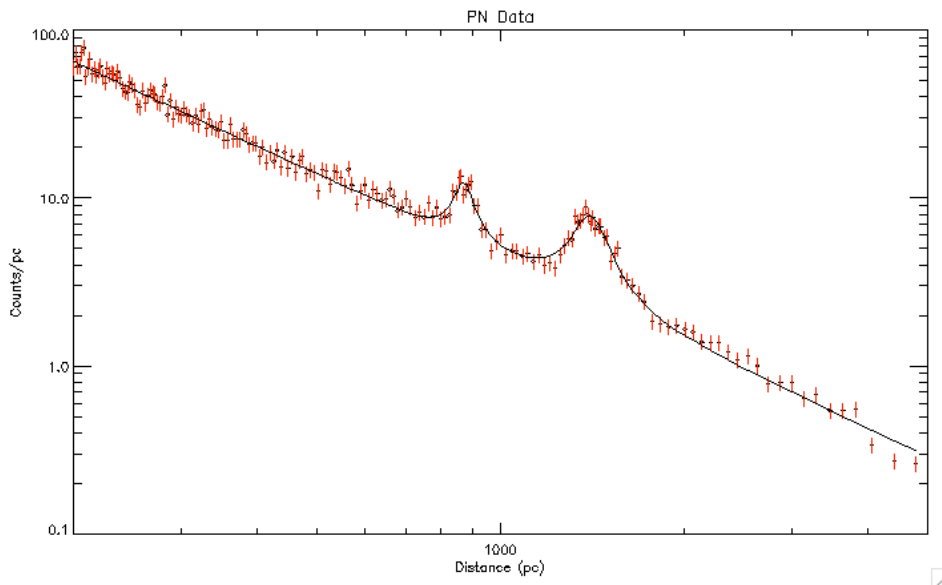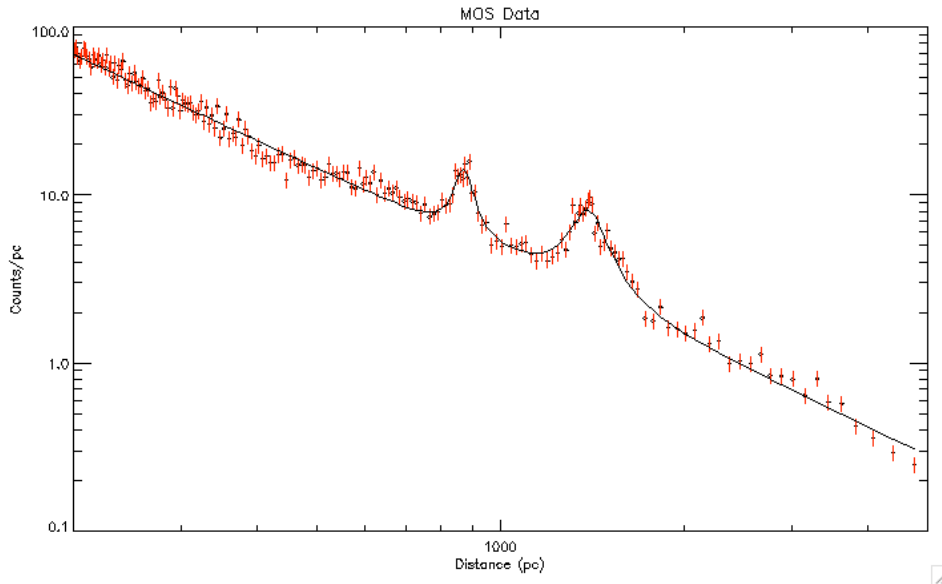**Figure 46.** Plot from the filtered and merged MOS1 and 2 data, excluding events with pattern values above 4, covering the energy range $1 - 2.5keV$ of counts/pc as a function of the distance to where the photons were scattered, together with the fitted power-law plus two Lorentzians. The plot is produced by the IDL procedure seen in Appendix A.5.

Finally the halo and afterglow spectra were grouped with their respective background spectra, RMF-files and ARF-files, to prepare them for fitting with XSPEC. This I did by using the FTOOLS task *grppha*. When using *grppha* the spectra is also binned; it is possible to choose how many counts per bin you wish to use. The bin sizes are responsible for how large the error bars for each bin become. For small bin sizes the x- error bars will be small, but the y- error bars will be large, and vice versa. Through the analysis, several different sizes for the bins were tested in order to find the best binning. Since the halo is not as bright compared to the background as the afterglow is, larger bins should be appropriate for the halo than for the afterglow[15]. Also the afterglow is extracted from a much smaller area and smaller bin sizes will make sure that there are not too few data points in the spectrum.

---

[15] Diffuse sources will have greater uncertainties connected to their intensities when they are corrected for background counts, than more bright sources. This is because the intensity is not much greater than the background. Making the bin sizes greater means that more data goes into calculating the value of the bin, thereby reducing the uncertainty

When analysing spectra in XSPEC it is not necessary to manually make background subtraction and calibrations to the data. By supplying the spectrum as a file grouped together with background spectrum, RMF-file and ARF-file, the corrections of the spectra are done automatically by XSPEC. The background subtracted spectra were fitted to an absorbed power-law;

$$F = e^{-n_H \sigma E} \cdot E^{-\Gamma} \cdot k_n \tag{28}$$

In XSPEC this model is represented by the expression; *phabs(pow)*. The fitting parameters are: n_H, which is the absorbing column, Γ, which is the photon index, and a normalisation constant, k_n. The cross-section, $\sigma(E)$, for photo-electric absorption has a default setting which should suffice according to XSPEC.

3.3.0.3. Scaling the spectra

At first the data could not be fitted to the model. The reason turned out to be that the corrected data-points had negative flux values. To check if this was because the background spectra were extracted from a much larger area, without proper calibration of the halo and the afterglow spectra, I tried applying background spectra which had the same geometrical shape as the halo and afterglow areas. With these new background spectra the spectra seemed to be properly corrected and could then be fitted. This method is not the best way to correct for background. Taking the average of a larger region without point sources is better than just cutting out a region that has the same size as the source spectrum. A way to scale a large background sampling area is using the SAS task *backscale*. This task adds a scaling keyword to the input spectrum according to the size of the area from which it is extracted. This task has to be performed on both background and source spectra. When the *backscale* keyword is set, the spectra will be background corrected in accordance with the scaling supplied. This task was performed on all spectra.

3.3.0.4. Extended sources

Since the halo is not a point source it might have a significant effect that the default setting, when doing the RMF- and the ARF-files for the spectra, is most suitable for point sources. When doing the RMF and ARF for the halo spectra, the keyword *detmaptype*, specifying the type of detector-map, should therefore be set to flat and the keyword *extendedsource* should be set to true (The XMM-Newton ABC Guide 2008). If the generation of these files are done on an extended source without taking this into account *rmfgen* will give a warning. The RMF- and ARF-files were redone in this way. Now the spectra were ready for fitting in XSPEC.

In the first attempt the halo and afterglow spectra were fitted separately, and different bin sizes were explored. The binning for the afterglow spectra that I found most appropriate was 25 counts per bin for both camera types. For the halo the most suitable binning was different for the two cameras. For the MOS data 150 counts per bin gave the best fitting results, and for the PN a binning of 250 counts per bin gave the best fitting results. This is in accordance with the fact that the MOS camera receives only 44% of the light and the PN camera receives the full beam from the respective telescopes, as stated in Section 1.5. As an example, the PN data results for the halo and afterglow spectra fitted independently to an absorbed power-law model with a spectral binning of 25 counts per bin for the afterglow and 250 counts per bin for, can be seen in Table 6.

Since the halo photons and the afterglow photons travel through the same dust medium the absorbing column for the halo and the afterglow should be the same. So instead of fitting the halo and the afterglow individually the two spectra were then fitted simultaneously, keeping the photon indices and normalisation constants different for the two but locking the absorbing column to be commonly fitted. For the PN data, the fitted parameters for the simultaneously fitted halo and afterglow can also be seen in Table 6.

individually fitted	halo spectrum	afterglow spectrum
n_H	8.27	7.65
Γ	3.07	1.84
k_n	$5.74 \cdot 10^{-4}$	$1.17 \cdot 10^{-4}$
$red\ \chi^2$	10.578	2.0425
$d.o.f.$	33	163
NHP	$1.89 \cdot 10^{-54}$	$9.91 \cdot 10^{-14}$
simultaneously fitted	halo spectrum	afterglow spectrum
n_H	0.78	
Γ	2.99	1.86
k_n	$5.20 \cdot 10^{-4}$	$1.22 \cdot 10^{-3}$
$red\ \chi^2$	3.4692	
$d.o.f.$	197	
NHP	$6.24 \cdot 10^{-55}$	

Table 6. The upper part is the individually fitted spectra, extracted from the filtered PN data including up to pattern 12 events, for both the halo and the afterglow. The lower part is the simultaneously fitted spectra, where n_H is locked to be the same, extracted from the PN data including up to pattern 12 events, for the halo and the afterglow events. The null hypothesis probability, NHP, and the number of degrees of freedom, $d.o.f.$, is given.

3.3.0.5. Fitting Statistics

Looking at the fitting results in Table 6 we see very low values for the null hypothesis probability (NHP)[16]. The same was the case for the MOS2 data fit. Very low NHP values mean that the fit is not good. The NHP should at least be above 0.1. Another parameter indicating the fitting statistics is χ^2. This value reveals how good the fit is; how well does the model follow the supplied data. For a good fit the reduced χ^2 should be close to one[17]. When delta chi squared for the different fits was plotted together with the spectrum, see Figure 47 for an example, it was revealed that some of the points located in the outer ranges of the spectra deviated significantly from the plot and had thereby caused the low NHP value. To get an acceptable NHP it was necessary to cut the interval down in order to avoid deviant points making an

---

[16]   The null hypothesis probability is the probability of getting a value of χ^2 as large or larger than observed if the model is correct

[17]   The reduced χ^2 is χ^2 divided by the number of degrees of freedom

acceptable fit impossible to obtain. This is done by using the XSPEC command *ignore* which controls which energy ranges are not included in the data to be fitted and plotted[18]. With the new energy ranges I re-fitted the data to the model, now showing acceptable values for the null hypothesis probability and χ^2.
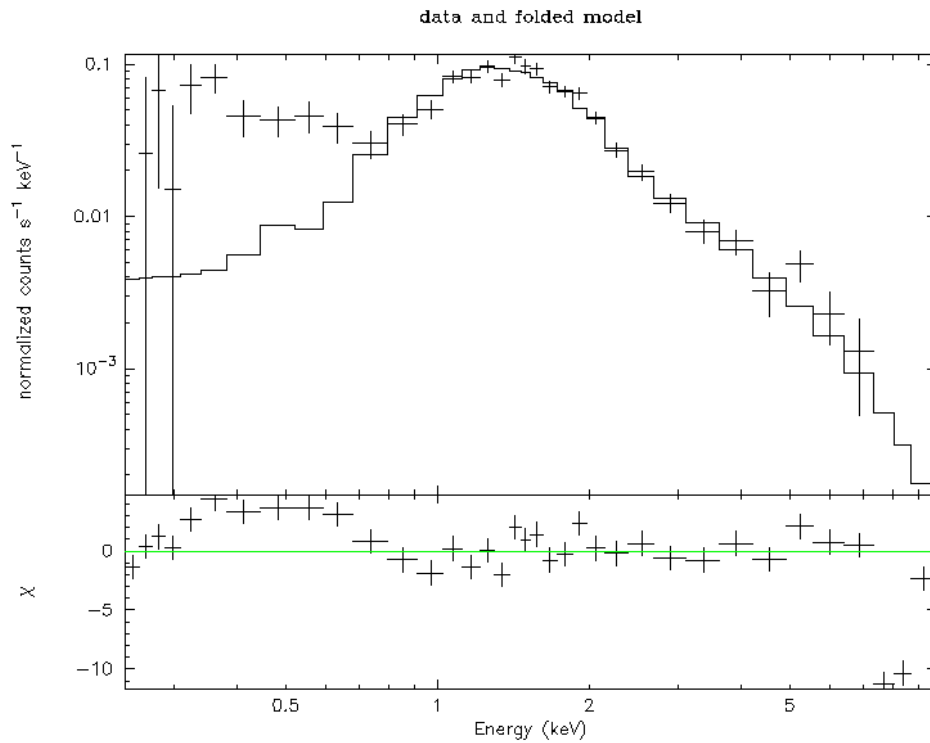
Figure 47. Plot showing the halo spectrum extracted from the PN data grouped to 250 counts per bin. The fit statistics for this plot are: a reduced chi-squared of 10.578 for 33 degrees of freedom and a null hypothesis probability of $1.89 \cdot 10^{-54}$. Clearly not a very good fit. Both to the right and the left we see the deviant points that have caused the fit to be bad.

3.3.0.6. Error bars

The independently fitted absorbing columns for the afterglow and the halo should be the same within error bars, since (as explained in Section 2.3.4) we expect the photons observed from the two to have travelled the same space. If they are not the same within errors, it is an indication

---

[18]   This command was also used before in order to exclude the, for the instruments, invalid energy ranges. That is below 200 eV and above 10 keV.

that something is wrong and it is therefore not suitable to fit them together.

The error bars provided immediately with the fit by XSPEC are not representable. These confidence intervals are calculated from the second derivatives of the fit statistic with respect to the model parameters at the best-fit. These are not reliable and should only be used as indications[19]. Instead the more relevant error bars are obtained by using the XSPEC command *error* on the parameter of choice. The default setting for the delta fit statistics is 2.706, equivalent to a 90% confidence region, but other confidence ranges can be chosen. The default of 90% was the setting I used. This was done on the absorbing columns and photon indices for the independent fits of both afterglow and halo. The fitted parameters, with the fitting statistics, what energy ranges they cover and the resulting error bars can be seen in the upper part of Table 7 for the PN data and in the upper part of Table 8 for the MOS2 data. For the MOS2 data the values for the absorbing column are consistent. A common fit; locking the absorbing column to be the same for both halo and afterglow, was thereby acceptable. This common fit is shown in the lower part of Table 8. The PN data absorbing columns for the afterglow and the halo are not consistent within error bars. As mentioned above they should be in order for the simultaneous fit to be relevant. Before discussing the MOS2 results, the problems with the PN results are investigated.

3.3.0.7. Quadruple, double or single events

When filtering the event files, pattern values up to 12 were included. These pattern values include events occupying up to 4 pixels. This might include some inappropriate events (although it should be all right to use pattern 12). In Section 3.2.3, fitting the counts/pc vs. distance to a power-law plus two Lorentzians, there was significant improvement to obtain, when the allowed pattern values were cut to only include 0-4 instead of 0-12. This, restricting the pattern values,

---

[19] Therefore they are not presented in the thesis.

pattern $<=12$	halo spectrum	afterglow spectrum
energy range	$0.7 - 7.0 keV$	$0.4 - 8.0 keV$
n_h	$9.10^{+1.12}_{-1.09}$	$7.3^{+0.5}_{0.7}$
Γ	$3.1^{+0.3}_{-0.2}$	$1.76^{+0.07}_{-0.10}$
k_n	$5.66 \cdot 10^{-3}$	$1.09 \cdot 10^{-4}$
red χ^2	1.368	1.0022
d.o.f.	19	152
NHP	0.130	0.410
pattern $=0$	halo spectrum	afterglow spectrum
energy range	$0.6 - 7.0 keV$	$0.2 - 8.0 keV$
n_h	$1.0^{+1.6}_{-1.4}$	$7.9^{+0.7}_{-0.6}$
Γ	$3.3^{+0.4}_{-0.3}$	2.27 ± 0.11
k_n	$7.46 \cdot 10^{-4}$	$0.11 \cdot 10^{-3}$
red χ^2	0.9116	1.0519
d.o.f.	15	106
NHP	0.550	0.338

Table 7. The upper part is the individually fitted spectra extracted from the filtered PN data including up to pattern 12 events using both halo events and afterglow events. The lower part is the individually fitted spectra extracted from the PN data including only pattern 0 events using both halo events and afterglow events. The error bars included are obtained by using the XSPEC command *error* on the parameter of choice. The errors are 90% confidence regions.

might also yield improvements to the results for the PN data spectra, causing the afterglow and halo to have better consistency. I therefore performed the above described spectral analysis on filtered PN data including only double and single events (pattern$\leq$ 4) and including only single events (pattern$=$ 0).

For the pattern 4 restricted events, It turned out that it was virtually impossible to get a good fit with the spectral data. When doing the spectral fitting, NHP stayed very low and any attempts to improve NHP by cutting down the energy ranges were unsuccessful. Some of the deviant points were located in the middle of the energy range. Several different groupings were explored. The highest value obtained

individually fitted	halo spectrum	afterglow spectrum
energy range	$0.5 - 7.0 keV$	$0.2 - 10 keV$
n_h	$9.8^{+2.1}_{-1.3}$	$8.5^{+1.4}_{-1.2}$
Γ	$3.4^{+0.5}_{-0.3}$	$1.97^{+0.19}_{-0.18}$
k_n	$8.55 \cdot 10^{-4}$	$1.35 \cdot 10^{-4}$
$red\ \chi^2$	1.481	0.949
$d.o.f.$	15	54
NHP	0.102	0.581
simultaneously fitted	halo spectrum	afterglow spectrum
energy range	$0.5 - 7.0 keV$	$0.2 - 10 keV$
n_h	$9.1^{+1.1}_{-0.9}$	
Γ	$3.3^{+0.3}_{-0.2}$	$2.04^{+0.17}_{-0.08}$
k_n	$7.51 \cdot 10^{-4}$	$1.47 \cdot 10^{-4}$
$red\ \chi^2$	1.066	
$d.o.f.$	70	
NHP	0.330	

Table 8. The upper part is the individually fitted spectra extracted from the filtered MOS2 data including up to pattern 12 events using both halo events and afterglow events. The lower part is the simultaneously fitted spectra, locking the absorbing column, n_H, to be the same for halo and afterglow. The error bars included are obtained by using the XSPEC command *error* on the parameter of in question. The errors are 90% confidence regions.

for the NHP was of the order 10^{-3}. So it was not possible to use the data, with pattern values only up to four, to get a good spectral fit.[20]

For the single event restricted data the outcome was more successful; the NHP values obtained were more reasonable, although the energy ranges still had to be cut down a bit. Here the grouping for the halo was set to 200 counts per bin instead of 250 counts per bin, since this filtering obviously decreases the number of data points. Using only single events the absorbing columns for the halo and afterglow still were not consistent within error bars, see the lower part of Table 7.

---

[20]   The reason for this is discussed in Section 4.1.

3.3.0.8. Pile-up

When a source is very bright it is possible that the events are affected by photon pile-up, see Figure 48 for an example. The afterglow is a very bright source so the afterglow events should actually be checked for pile-up. SAS has a task, *epatplot* that checks for pile-up, by making two plots from which it is possible to deduce whether there is pile-up. This task was run, but the results were inconclusive and unclear. For any source the central area will usually be the area with the highest number of counts, so when a source has pile-up it will start from the central area. If you want to exclude the piled up events the central region should be left out. So a way to correct piled-up data is to cut out the central region.
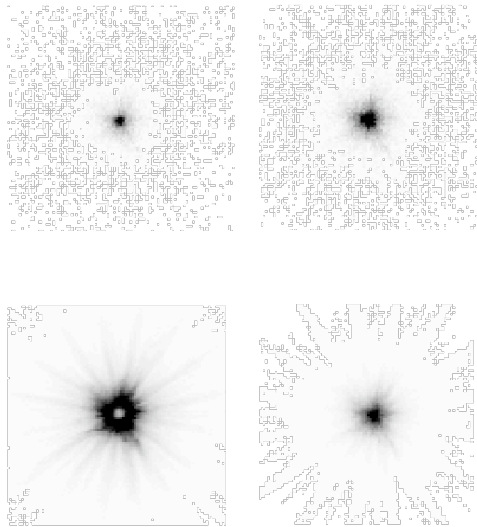
Figure 48. image displaying the visual effects of photon pile-up on a bright source. Moving through the four images from upper left to lower left we see more and more pile-up, from XMM-Newton Users' Handbook (2003)

Since the PN data showed inconsistencies, pile-up was an effect worth taking into consideration. To check if the pile-up was present, instead of using the circular region of 40" to extract the PN afterglow spectrum from, I used an annulus with an outer radius of 30" and an inner radius of 4". Also an afterglow spectrum from an annulus of outer radius 15" and inner radius of 4", was made. The smaller outer radius assumed in an attempt to avoid too much background. Extracting a new afterglow spectrum from the above annuli and then performing the above men-

tioned preparations (*backscale*, ancillary region files and grouping), a new fit with associated 90% confidence range error bars, was made for the afterglow. This was done for both the data set using only single events (Pattern=0) and the data set containing events covering up to 4 pixels (pattern $\leq$12). For the single event afterglow spectrum extracted from an annulus of 15"-4", the NHP stayed below 0.1. A narrower energy interval giving suitable null hypothesis probability could not be found. The reason for this problem could be that there are too few points to fit since the filtering is very restricting in this particular case. So for the single event restricted data, only the larger afterglow annulus gave usable fits. All the new PN afterglow fits with error bars can be seen in Table 9, together with the halo fits from earlier. Here the absorbing columns for the halo and afterglow were consistent within uncertainties. This implies that the PN afterglow events were actually affected by pile-up, and the PN data was improved by the use of an annulus for the afterglow spectrum extraction. For the MOS2 data the above described pile-up corrections were not applied since the spectra extracted from this data had no inconsistency problems.[21]

Now with the new annuli afterglow spectra the afterglow and the halo absorbing columns for the PN data could be fitted simultaneously, the fitted parameters can be seen in Table 10. From the Table we see that according to the null hypothesis probability and chi-squared values the best fit is obtained with an annulus of 30"-4" using events with pattern 0-12. With this we get a fitted absorbing column of $n_H = 7.8^{+0.6}_{-0.5} \cdot 10^{21}cm^{-2}$ and photon indices of $\Gamma =2 .87^{+0.14}_{-0.13}$ and $\Gamma =1 .79^{+0.09}_{-0.05}$ for the halo and afterglow respectively. From the MOS2 data the common absorbing column was found to be $n_H = 9.1^{+1.1}_{-0.9} \cdot 10^{21}cm^{-2}$ and the photon indices were found to be $\Gamma = 3.3^{+0.3}_{-0.2}$ and $\Gamma = 2.04^{+0.17}_{-0.08}$ for the halo and afterglow respectively (shown in Table 8). The n_H values from the MOS2 spectra and the PN spectra are consistent, although the PN data confidence range is a bit lower than the MOS2 data confidence range. The photon indices from the PN and MOS2 data respectively

---

[21] This will be discussed in 4.1

do not match. The fitted PN spectra for pattern values up to 12 can be seen in Figure 49 and for the smaller afterglow annulus in Figure 50. The fitted PN spectrum from single event filtered spectra, using the larger afterglow annulus, can be seen in Figure 51. The MOS2 spectral fit including both halo and afterglow spectra can be seen in Figure 52. Looking at all these spectra we clearly see that the halo spectra is significantly steeper than the afterglow spectra, as would be expected if the halo light is in fact the scattered light from the afterglow, as explained in Section 2.3.4.

Figure 49. Spectra from the PN data, using events with pattern values up to 12, of the afterglow (red) and the halo (black) with the fitted model. The afterglow is extracted from an annulus of 30"-4" and the halo is extracted from an annulus of 220"-110". The afterglow-counts are from an energy range of 0.3-8 keV and the halo-counts are from an energy range of 0.6-7.5 keV. The fitted parameters are shown in Table 10.

Since the fitting results from the two sets of data were not consistent, I suspected that the PN spectra might not have been corrected enough for pile-up. I therefore decided to try and re-extract the PN spectra from an annulus were a larger region would be cut out from the centre.
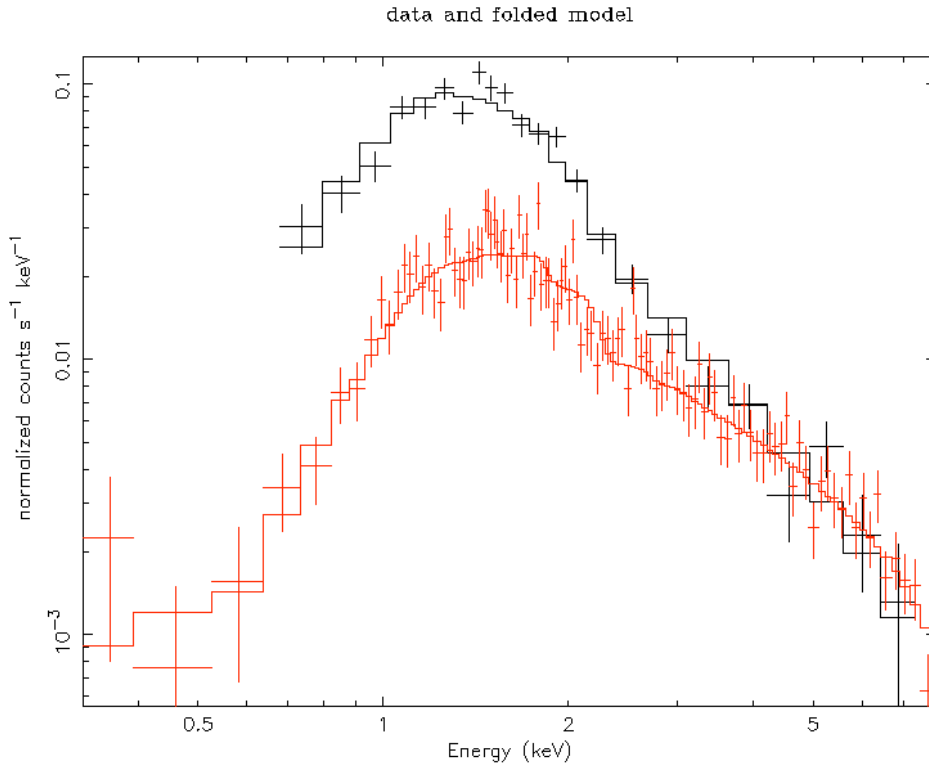
data and folded model

Figure 50. Spectra from the PN data, using events with pattern values up to 12, of the afterglow (red) and the halo (black) with the fitted model. The afterglow is extracted from an annulus of 15"-4" and the halo is extracted from an annulus of 220"-110". The afterglow-counts are from an energy range of 0.3-8.0 keV and the halo-counts are from an energy range of 0.6-7.5 keV. The fitted parameters are shown in Table 10.

I therefore prepared spectra from an annulus of outer radius 30" and inner radius 8". The data was filtered to only contain events with pattern values up to 12. The spectra was grouped as before and a new fit was performed in XSPEC. The fitted parameters can be seen in Table 11, the upper panel showing individual fits and the lower panel showing a simultaneous fit. A plot of the spectrum together with the fitted model can be seen in Figure 53. The values found from this filtering was an absorbing column $n_H = 8.2 \pm 0.7 \cdot 10^{21} cm^{-2}$ and photon indices $\Gamma = 2.96^{+0.18}_{-0.16}$ and $\Gamma = 1.86^{+0.12}_{-0.09}$ for the halo and afterglow respectively. These values are all consistent within uncertainties with those found from the MOS2 data.

Looking at the fitting statistics for these new PN results they not as good (although good enough) as those obtained before with an annulus
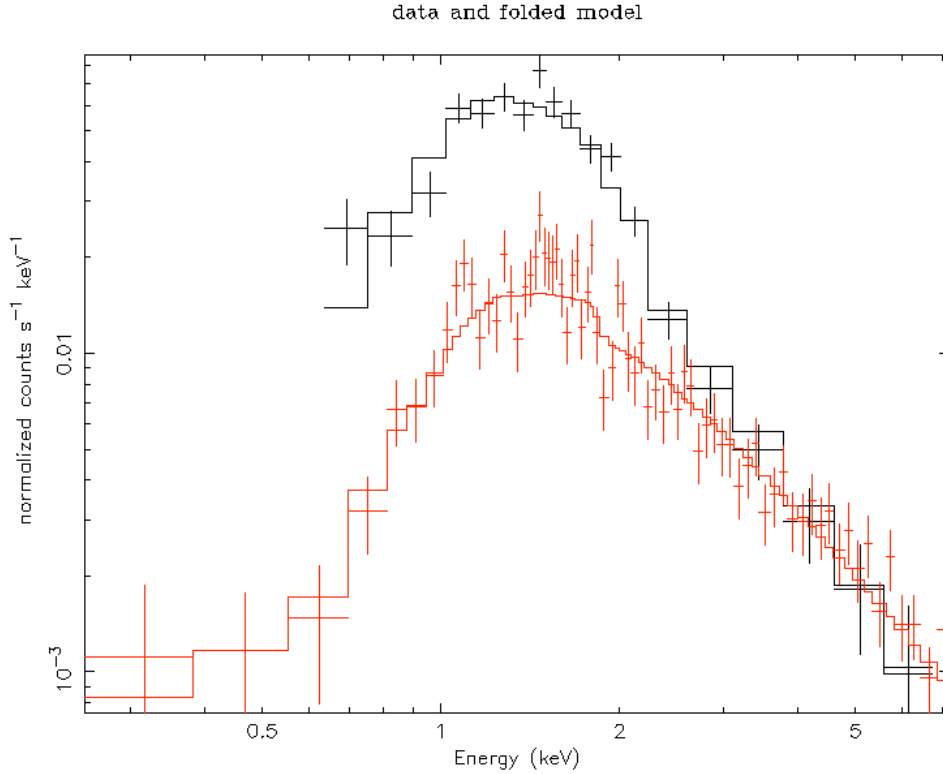
Figure 51. Spectrum from the PN data, using only single events, of the afterglow (red) and the halo (black) with the fitted model. The afterglow is extracted from an annulus of 30"-4" and the halo is extracted from an annulus of 220"-110". The afterglow-counts are from an energy range of 0.2-7.5 keV and the halo-counts are from an energy range of 0.6-7 keV. The fitted parameters are shown in Table 10.

of 30"-4" and pattern values up to 12. Earlier discussing at the results in Table 10, I chose to emphasise the results from this filtering since this had better fitting statistics than the results obtained from the smaller annulus data (15"-4") and obtained from the single event only data. In cases of pile-up, this is actually not a suitable way to evaluate the best results. The reason for this is that if some of the spectras are still affected by pile-up this will not be shown in the fitting statistics. The fitting statistics only show how good the provided data fits the model, but with pile-up the spectral data will not follow the true behaviour of the spectrum. Pile-up will not, as for example unfiltered background events, cause singular bad points, but an overall change in the spectrum. This means that even though the model is a very good fit it has been fitted to erroneous data.
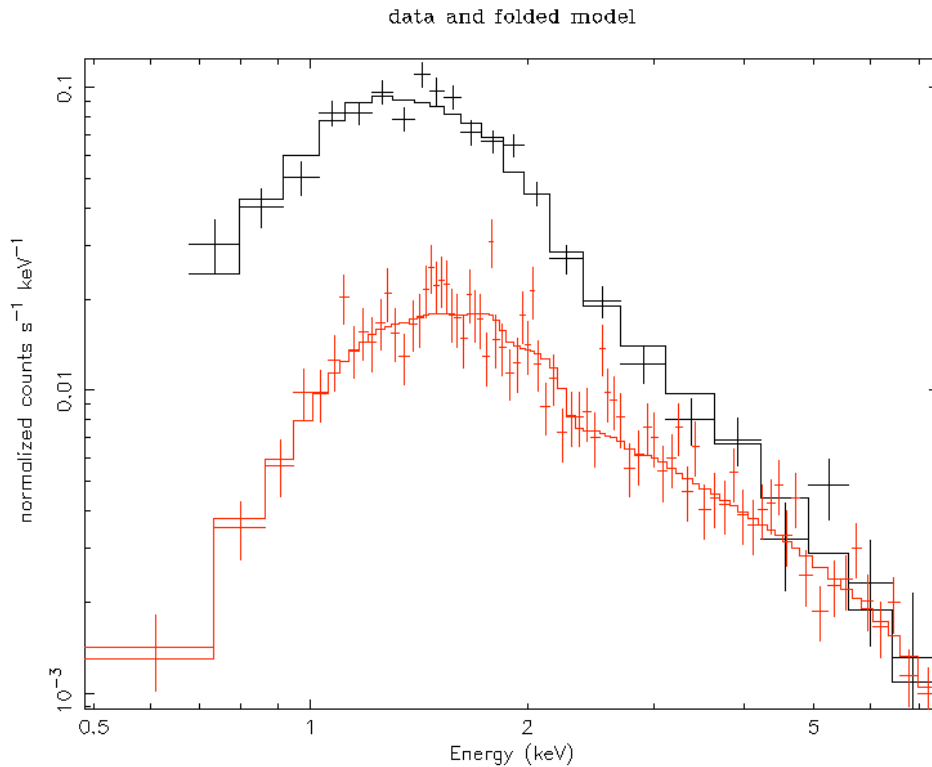
Figure 52. Spectrum from the MOS2 data, using events with pattern values up to 12, of the afterglow (red) and the halo (black) with the fitted model. The afterglow is extracted from a circle of 40" and the halo is extracted from an annulus of 220"-110". The afterglow-counts are from an energy range of 0.2-10 keV and the halo-counts are from an energy range of 0.5-7 keV. The parameter values can be seen in Table 8.

When evaluating the PN results we therefore cannot use the fitting statistics to choose the best representation of the observed spectra. Since we know the afterglow is affected by pile-up, the best spectral data would be that filtered to contain as many afterglow events as possible, while avoiding as much pile-up as possible. So a not too restrictive filtering combined with cutting out much of the central area is probably best. This would make the spectral data from the annulus 30"-8" with pattern values up to 12 most suitable to use, giving the results represented in Table 11. As mentioned, these are consistent with the MOS2 results, thereby also supporting this filtering to be the most suitable.
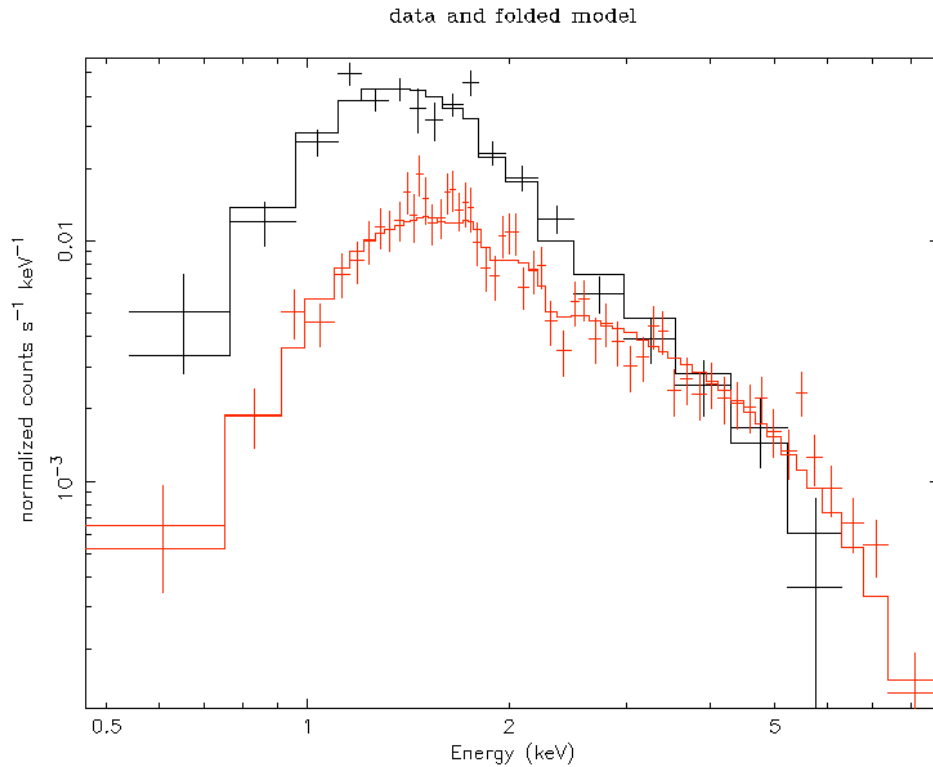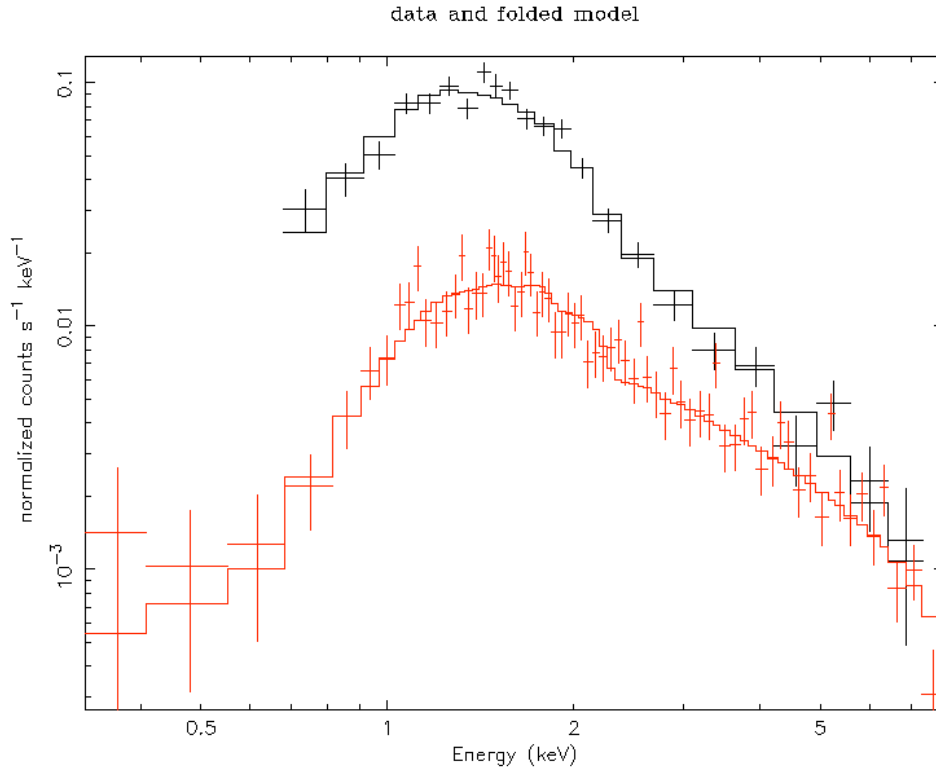
Figure 53. Spectrum from the PN data, using events with pattern values up to 12, of the afterglow (red) and the halo (black) with the fitted model. The afterglow is extracted from an annulus of 30"-8" and the halo is extracted from an annulus of 220"-110". The afterglow-counts are from an energy range of 0.2-10 keV and the halo-counts are from an energy range of 0.5-7 keV. The parameter values can be seen in Table 11.

3.3.0.9. Stepping parameter values

During the estimation of error bars XSPEC gave some warnings on the validity of the final fitted values for the photon indices for the PN halo spectra. This was in the fitting of the halo spectra simultaneous with the afterglow spectra extracted from the annulus of 30" and of 15" allowing up to pattern 12 events. A warning also turned up when checking the error for the absorbing column fitted from the PN single event halo- and afterglow-spectrum (from the 30"-4" annulus) simultaneously. To check if the results were valid or not I used the XSPEC command *steppar* to check different values for the photon indices. The *steppar* command performs a fit while stepping the parameter of choice, thereby generating a statistics surface for one or more parameters. In

this way it becomes evident whether there is more than one fit with low chi-squared value. The result were plotted using the command *plot contour* which plots chi-squared versus the parameter in question. The three plots resulting from this can be seen in Figures C.1, C.2 and C.3. It was clear from the plots that there were no ambiguity in the fitted parameter values presented in Table 10.

Table 9. Parameters for the individually fitted halo and afterglow from the filtered PN data. Using different area and pattern filtering specified in the table. NHP is the null hypothesis probability and d.o.f. is the number of degrees of freedom.

pattern $<=12$	halo spectrum	afterglow spectrum
annulus	$30" - 4"$	$220" - 110"$
Energy range	$0.7 - 7.5 keV$	$0.3 - 8 keV$
n_h	$9.10^{+1.12}_{-1.09}$	$7.5^{+0.6}_{0.8}$
Γ	$3.1^{+0.3}_{-0.2}$	$1.76^{+0.08}_{-0.11}$
k_n	$5.66 \cdot 10^{-3}$	$1.08 \cdot 10^{-4}$
red χ^2	1.368	1.0035
d.o.f.	19	107
NHP	0.130	0.472
annulus	$15" - 4"$	$220" - 110"$
Energy range	$0.7 - 7.5 keV$	$0.2 - 10 keV$
n_h	$9.10^{+1.12}_{-1.09}$	$8.0^{+0.9}_{-0.7}$
Γ	$3.1^{+0.3}_{-0.2}$	$1.79^{+0.11}_{-0.10}$
k_n	$5.66 \cdot 10^{-3}$	$1.13 \cdot 10^{-4}$
red χ^2	1.368	1.176
d.o.f.	19	77
NHP	0.130	0.139
pattern $=0$	halo spectrum	afterglow spectrum
annulus	$30" - 4"$	$220" - 110"$
Energy range	$0.6 - 7 keV$	$0.2 - 7.5 keV$
n_h	$9.4^{+1.6}_{-1.2}$	$7.6^{+0.8}_{-0.7}$
Γ	$3.2^{+0.4}_{-0.3}$	2.19 ± 0.14
k_n	$6.67 \cdot 10^{-4}$	$7.18 \cdot 10^{-2}$
red χ^2	1.270	1.105
d.o.f.	16	70
NHP	0.206	0.255

Table 10. Parameters for the simultaneously fitted halo and afterglow from the filtered PN data. Using different area and pattern filtering specified in the table. NHP is the null hypothesis probability and d.o.f. is the number of degrees of freedom.

pattern $<=12$	$halo$ $spectrum$	$afterglow$ $spectrum$
$annulus$	$30" - 4"$	$220" - 110"$
$Energy\ range$	$0.6 - 7.5 keV$	$0.3 - 8 keV$
n_h	$7.8^{+0.6}_{-0.5}$	
Γ	$2.87^{+0.13}_{-0.14}$	$1.79^{+0.09}_{-0.05}$
k_n	$4.98 \cdot 10^{-4}$	$1.13 \cdot 10^{-4}$
$red\ \chi^2$	1.0836	
$d.o.f.$	128	
NHP	0.244	
$annulus$	$15" - 4"$	$220" - 110"$
$Energy\ range$	$0.6 - 7.5 keV$	$0.3 - 8 keV$
n_h	$8.2^{+0.7}_{-0.6}$	
Γ	2.96 ± 0.16	$1.79^{+0.10}_{-0.07}$
k_n	$5.35 \cdot 10^{-4}$	$1.14 \cdot 10^{-4}$
$red\ \chi^2$	1.1475	
$d.o.f.$	96	
NHP	0.153	
pattern $=0$	$halo$ $spectrum$	$afterglow$ $spectrum$
$annulus$	$30" - 4"$	$220" - 110"$
$Energy\ range$	$0.6 - 7 keV$	$0.2 - 7.5 keV$
n_h	$8.2^{+0.4}_{-0.7}$	
Γ	$2.98^{+0.20}_{0.19}$	$2.28^{+0.12}_{-0.13}$
k_n	$5.18 \cdot 10^{-4}$	$7.96 \cdot 10^{-4}$
$red\ \chi^2$	1.1704	
$d.o.f.$	87	
NHP	0.132	

individually *fitted*	*halo* *spectrum*	*afterglow* *spectrum*
energy range	$0.7 - 7.5 keV$	$0.3 - 8 keV$
n_h	$9.1^{+1.2}_{-1.1}$	$7.8^{+0.9}_{-1.1}$
Γ	$3.1^{+0.3}_{-0.2}$	$1.83^{+0.11}_{-0.15}$
k_n	$5.66 \cdot 10^{-3}$	$1.20 \cdot 10^{-4}$
$red\ \chi^2$	1.304	1.096
$d.o.f.$	19	69
NHP	0.130	0.272
simultaneously *fitted*	*halo* *spectrum*	*afterglow* *spectrum*
energy range	$0.6 - 7.5 keV$	$0.3 - 8 keV$
n_h	8.2 ± 0.7	
Γ	$2.96^{+0.18}_{-0.16}$	$1.85^{+0.12}_{-0.09}$
k_n	$5.36 \cdot 10^{-4}$	$1.26 \cdot 10^{-4}$
$red\ \chi^2$	1.1687	
$d.o.f.$	90	
NHP	0.131	

Table 11. The upper part is the individually fitted spectra extracted from the PN data including up to pattern 12 events using both halo events and afterglow events. The afterglow is extracted from an annulus of 30"-8" and the halo is extracted from an annulus of 220"-110". The lower part is the simultaneously fitted spectra. The error bars included are obtained by using the XSPEC command *error* on the parameter of in question. The errors are 90% confidence regions.

4. Discussion and Conclusion

Through the analysis performed in this thesis it was demonstrated how efficient a tool, these X-ray halos around afterglows, in fact are in obtaining information on the dust in our Galaxy. They can reveal distances and characteristics of the dust, otherwise unknown to us. In this thesis, through the use of different methods, the existence of two dust slabs in the line of sight to the GRB 031203 was firmly substantiated, and the distances to these were derived. Through my work I encountered quite a few problems, whereof most, through several trial and error attempts, were eventually resolved. Below, in Section 4.1, these different problems and the solutions are discussed and summarised. In Section 4.2, my results are compared to those existing in literature as a check for consistency and in Section 4.3 my results are summarised and discussed.

A by-product of the analysis performed here was that I became accustomed to using the software, SAS, FTOOLS and XSPEC, which were earlier unfamiliar to me. This required some time spent on just getting to know these packages before a useful analysis could be performed.

4.1. Problems and Solutions

In the first part of the analysis I produced SAS-histogram plots of the counts versus θ profile, see Section 3.2.2. These where despite of testing several different binnings and types of filtering not very clear. The peaks derived from these plots would have been a bit suggestive. I instead thought of using IDL to bin and plot the counts, thereby giving me more control of the specifics on how the counts would be binned. This allowed me to make the bins overlap, giving me more data points and consequently greater resolution of the plots. The problems with the SAS histogram plots were that the peaks were either too low (requiring greater bins) or contained to few data points (requiring smaller bins).

The overlapping resolved this problem, since the overlapping meant that the size of the bins did not restrict how many bins there would be. This approach was successful and meant that the peaks found were not suggestive but quite unambiguous.

In the fitting of the counts per pc versus distance profile, in Section 3.2.3, the results derived from the two cameras were not quite compatible. Also the distances were not completely consistent with those found earlier, in Section 3.2.2. I decided to try and use only single and double events (pattern$\leq$ 4), since this might remove some unwanted noise. This clearly improved the results, mainly it was the PN data results that changed. Because the MOS data set was merged from two cameras, noise will have a less significant effect on the results from the data. The results from the two different cameras were now more compatible and the distances were now consistent with those derived earlier.

When doing the spectroscopic analysis the extracted spectra could at first not be fitted to the expected model. When plotting the data I discovered that the spectra showed negative flux values. I realised that this was probably because the background correction was not done correctly. To check if this was the case, smaller background areas, corresponding to the extraction areas of the spectra, were used instead of the large sample regions. This resulted in background corrected spectra that matched the expectations, allowing them to be fitted to the model. This made it clear to me that if the large sample regions were to be used they needed to be scaled. I later discovered a way to do this, as described in Section 3.3.0.3.

When the data finally could be fitted there were still problems. The spectral data included a few deviant points, causing the fitting statistics to be bad. To avoid getting bad fits these points were cut out by narrowing the energy range used for the fitting. This greatly improved the fitting statistics.

From theory it was expected that the halo spectrum and the afterglow spectrum should have the same absorbing column. For the PN

data, this was not the case to begin with, suggesting that the found spectra were in some way flawed.

The first idea I had for improvements was to use a more restricting filtering. I extracted spectra, only using single and double events, and spectra only using single events. This did not improve the consistency between halo and afterglow values for the absorbing column.

The data set including both single and double events (pattern$\leq$ 4) where not useful all, since it was impossible to get good fitting statistics. Meanwhile the data set only including single events (pattern=0) did provide acceptable fitting statistics (Although still not providing consistency between afterglow and halo). Bad fitting statistics can be caused both by to few points to fit and by singular bad points not following the norm. At first glance it might seem odd that the data set with pattern$\leq$ 4 could not yield a good fit while both the data sets with pattern=0 and pattern$\leq$ 12 could. This is in fact quite reasonable, since a pattern$\leq$ 4 filtered data set will have less points than a pattern$\leq$ 12 filtered data set but potentially more of the deviant points than a pattern=0 filtered data set.

The different pattern restrictions not having resolved my problem (of the afterglow and halo absorbing column not being consistent), I realised that since the afterglow is a very bright source it could be affected by photon pile-up. To correct for this, the afterglow spectra was extracted from an annulus instead of a circle, since pile-up starts from the centre of a source, as explained in Section 3.3.0.8. From this change the afterglow and halo values for the absorbing column were consistent. So the afterglow must have been affected by pile-up and the exclusion of the central area did improve my results.

The fact that the MOS2 data did not have any consistency problems between afterglow and halo, thereby indicating no pile-up in the afterglow seems reasonable. The MOS cameras only receives 44% of the light from the telescopes, while the PN camera receives all the light coming from the telescope. This means that it is less likely for data from a MOS camera to be affected by pile-up.

The various PN data results, involving different pattern restrictions and annuli sizes, showed that the data set with the afterglow spectrum from an annulus of 30"-4" and pattern values up to 12, gave the best fitting statistics. Meanwhile, since pile-up seemed to be present, the fitting statistics could not be used to evaluate the best filtering[22]. Other reasoning had to be used. I evaluated that the least restrictive filtering, thereby giving as many data points to fit as possible, combined with correcting for as much pile-up as possible, by cutting out much of the central area, was best. This being the afterglow spectrum extracted from the annulus of 30"-8" allowing up to pattern 12.

With the spectra extracted from the MOS1 data, there seemed to be a scaling problem. The count levels were in some cases[23] too low to be fitted to the model, the curve looking very flat. When the spectra could actually be fitted the afterglow spectra gave much lower values for the absorbing columns from the afterglow spectrum than from the halo spectrum. This made it unfit to fit the afterglow and halo spectra simultaneously. This could perhaps be caused by corrupted response files (RMF and ARF) or by problems with the background subtraction. It was also evident that something was wrong with the scaling of the MOS1 afterglow spectrum since the spectrum clearly had overall lower normalised counts/s/keV and generally looked much flatter than the afterglow spectrum from the PN data and the MOS2 data (which did show consistency between halo and afterglow spectra). Since the MOS1 spectral data was problematic and I on the other hand had two good data sets to work with, the results in my spectral analysis only include PN and MOS2 data.

---

[22] As explained in Section 3.3.0.8, this is because pile up can change the overall shape of the spectrum.

[23] Depending on what energy ranges and sizes of bins chosen.

Table 12. Comparison of the results from this thesis, with those from literature, by Vaughan et al. (2004) and Tiengo & Mereghetti (2006). Halo 1 denotes the values for the inner halo, while Halo 2 denotes the values from the outer halo.

Photometric Analysis				
Halo1	MOS	PN	Vaughan	T & M
Distance, section 3.2.2	$1414pc$	$1416pc$	$1388pc$	
	$\pm 26pc$	$\pm 22pc$	$\pm 32pc$	
Distance, section 3.2.3	$1390pc$	$1403pc$		$1384pc$
	$\pm 5pc$	$\pm 5pc$		$\pm 9pc$
$FWHM$	$218 \pm 16pc$	$224 \pm 16pc$		$240 \pm 30pc$
$\mathcal{L}(counts)$	1857 ± 159	1837 ± 156		1740^{+270}_{-240}
Halo2				
Distance, section 3.2.2	$872pc$	$883pc$	$882pc$	
	$\pm 11pc$	$\pm 16pc$	$\pm 20pc$	
Distance, section 3.2.3	$870pc$	$871pc$		$870pc$
	$\pm 3pc$	$\pm 3pc$		$\pm 5pc$
$FWHM$	$70 \pm 8pc$	$78 \pm 10pc$		$82^{+17}_{-14}pc$
$\mathcal{L}(counts)$	930 ± 120	819 ± 118		$840^{+210}_{-180}pc$
Spectral Analysis				
	MOS2	PN	Vaughan	
$n_H[10^{21}\,\mathrm{cm}^{-2}]$	$9.1^{+1.1}_{-0.9}$	8.2 ± 0.7	8.8 ± 0.5	
Γ_{halo}	$3.3^{+0.3}_{-0.2}$	$2.96^{+0.18}_{-0.16}$	3.03 ± 0.14	
$\Gamma_{afterglow}$	$2.04^{+0.17}_{-0.08}$	$1.85^{+0.12}_{-0.09}$	1.98 ± 0.05	

4.2. Comparison With Literature

In Table 12 the results from this thesis are shown together with equivalent results from literature. The papers referred to in this section and in the table are also mentioned in Section 1.7.

In the paper by Vaughan et al. (2004), the counts versus θ relationship was found, leading to a relationship of θ versus time. Fitting this to a power-law, he found power-law indices of 0.53 ± 0.04 and 0.51 ± 0.05 for the inner and outer halo respectively. Locking the power-law indices he found distances of 1388 ± 32pc and 882 ± 20pc for the inner and outer halo respectively.

In my similar analysis I found photon indices of 0.51 ± 0.03 and 0.503 ± 0.018 for the inner and outer halo respectively for the MOS data. For the PN data I found 0.51 ± 0.03 and 0.51 ± 0.03 for the inner and outer halo respectively. The power-law indices derived in this thesis are in perfect agreement with the results derived by Vaughan et al. (2004), although my power-law indices are closer to the, from theory, expected value of 0.5. The distances I derived from the constants, resulting from locking the power-law index to 0.5, were 1414 ± 26pc and 872 ± 11pc for the inner and outer halo respectively for the MOS data. For the PN data the distances were 1416 ± 22pc and 883 ± 16pc for the inner and outer halo respectively. These distances are all consistent with those derived by Vaughan et al. (2004) though my results have slightly smaller uncertainties. The smaller uncertainties on the results from the inner halo are caused by the fact that I have 10 maxima points, for fitting the halo expansion, while Vaughan et al. (2004) only uses eight.

In the paper by Tiengo & Mereghetti (2006), a counts per pc versus distance given in pc is found, and fitted to a power-law plus two Lorentzians. From this they find distances to the two dust slabs of 1384 ± 9pc and 870 ± 5pc for the inner and outer halo respectively. They also find FWHM for the two peaks of 240 ± 30pc and 82^{+17}_{-14}pc for the inner and outer halo respectively. From the integrated Lorentzians they find 1740^{+270}_{-240} counts and 840^{+210}_{-180} counts in the inner and outer halo respectively.

In my similar analysis I find distances to the two dust slabs of $1390 \pm 5pc$ and 870 ± 3pc for the inner and outer halo respectively from the MOS data. From the PN data I find 1403 ± 5pc and 871 ± 3pc for the inner and outer halo respectively. All these distances are consistent with those derived in Tiengo & Mereghetti (2006) except the one derived by use of PN inner halo data, which comes very close. Here my derived distances again have slightly smaller uncertainties. The smaller uncertainties, in my results can be ascribed to my use of a slightly larger energy range (I use 1-2.5 keV while they use 1-2 keV), since this gives me more data. More data will most often diminish uncertainties, since

it can improves the basis of the derived results. All these distances are also consistent with the Vaughan et al. (2004) distance results listed above.

My distances from the count versus θ plots are also consistent with the distances derived by Tiengo & Mereghetti (2006). Here the results from Tiengo & Mereghetti (2006) have smaller uncertainties, but since they are derived by use of a different method this is not unexpected. The small discrepancies between my results (the PN data inner halo) and the ones in Tiengo & Mereghetti (2006) can also be ascribed to the slightly different filtering criteria used. In my first attempt allowing up to pattern 12 the differences between our results were larger, but using the same patterns values (0-4) the discrepancies diminished.

I also found a FWHM of the halo peaks; for the MOS data i find 218 ± 16pc and 70 ± 8pc for the inner and outer halo respectively. For the PN data I find 224 ± 16pc and 78 ± 10pc for the inner and outer halo respectively. These are also all consistent with the results derived by Tiengo & Mereghetti (2006).

The number of halo counts i find by integrating the Lorentzians are 1740^{+270}_{-240} counts and 840^{+210}_{-180} counts in the inner and outer halo respectively for the MOS data. For the PN data 1740^{+270}_{-240} counts and 840^{+210}_{-180} counts in the inner and outer halo respectively. These results show slightly smaller uncertainties[24], but are consistent with those by Tiengo & Mereghetti (2006).

In the paper by Vaughan et al. (2004), the spectra of the halo and afterglow are also simultaneously fitted to an absorbed power-law. Here he finds a common absorbing column for both the halo and afterglow of $8.8 \pm 0.5 \cdot 10^{21}\,\mathrm{cm}^{-2}$. He also finds photon indices for the afterglow and halo respectively of $\Gamma = 1.98 \pm 0.05$ and $\Gamma = 3.03 \pm 0.14$.

In my analysis of the halo and afterglow spectra the values derived for the absorbing column and with the MOS2 and the PN data respectively were $9.1^{+1.1}_{-0.9} \cdot 10^{21}\,\mathrm{cm}^{-2}$ and $8.2 \pm 0.7 \cdot 10^{21}\,\mathrm{cm}^{-2}$. This is consistent with that found by Vaughan et al. (2004). My MOS2 results for the photon

---

[24] As before the smaller uncertainties can be attributed to the different filtering criteria.

indices were for the afterglow and halo respectively $\Gamma = 2.04^{+0.17}_{-0.08}$ and $\Gamma = 3.3^{+0.3}_{-0.2}$. My PN results for the photon indices were for the afterglow and halo respectively $\Gamma = 1.85^{+0.12}_{-0.09}$ and $\Gamma = 2.96^{+0.18}_{-0.16}$. These are also all consistent with the results in Vaughan et al. (2004).

The results from the PN data, although consistent within uncertainties, are a bit low compared to both the results from Vaughan et al. (2004) and my own results from the MOS2 data. This could imply that there is still a little bit of pile-up in effect and a slight correction is still needed. This could be done by making the inner radius in the annulus larger, thereby excluding more of the central events.

In order to get acceptable fitting statistics for my spectra, I had to narrow down the energy intervals used for the fitting. Looking at the spectral fit from Vaughan et al. (2004), see Figure 22, we see that the same has been done here. The red curve representing the fitted model for the halo spectrum starts at ≈ 0.65 keV and ends at ≈ 7 keV. So we see that deviant points, causing bad fitting statistics, were not an issue present only in my data set.

The absorbing column in our Galaxy is mapped for most lines of sight. If you wish to know the absorption in some specific direction there are estimates from several sources. In the $HEASoft$ package (NASA 2008) a programme exists, that calculates the absorbing column in any specified direction, based on current estimates. For the area around the direction of the GRB the value found by this programme is $5.95 \cdot 10^{21} cm^{-2}$. The absorbing column, for the GRB 031203 afterglow, derived in this thesis is significantly larger than this galactic value. The excess, of $\approx 2 - 3 \cdot 10^{21} cm^{-2}$ probably stems from the absorption in the host galaxy and can be used as an estimate thereof. The galactic coordinates for the GRB are 255.733 -04.800 (SIMBAD 2009) which means that the line of sight to the GRB is in the plane of the galactic disk. For sources with lines of sight going through the disk it is very likely for the light to travel through dust. The line of sight to the GRB passes through the GUM Nebula (Vaughan et al. 2004), which these explored dust slabs may very well be part of.

4.3. Conclusion

In this thesis the afterglow of GRB 031203 and the surrounding expanding dust scattered halo was studied.

During this study it was determined how the X-ray halo around GRB 031203 grows. The halo was shown to expand with a power-law dependency on time. The power-law index for the inner halo was found from both the PN and the MOS data to be 0.51 ± 0.03. For the outer halo the PN data yielded an index of 0.51 ± 0.03 while the MOS data yielded 0.503 ± 0.018. These power-law indices all agree with the theoretically predicted value of 0.5.

Locking the power-law index to 0.5 I found the power-law proportionality constants yielding estimates of the distance to the dust slabs causing the scattering. From the PN data the distance to the dust causing the inner halo was 1416 ± 22pc and the outer halo was 883 ± 16pc. For the MOS data the results were 1414 ± 26pc for the inner and 872 ± 11pc for the outer. We see that the results from the MOS and the PN data agree very well, thereby supporting the validity of my results.

Distances to the dust slabs were also obtained from fitting the $counts/pc$ versus $distance(pc)$ profile, to a power-law plus two Lorentzians. The resulting distances derived from the PN data were 1403 ± 5pc for the inner halo and 871 ± 3pc for the outer halo. From the MOS data the distances were 1390 ± 5pc for the inner halo and 870 ± 3pc for the outer halo. The results from the MOS and PN agree perfectly within uncertainties for the outer halo. For the inner halo the PN and MOS results do not agree within uncertainties but are still compatible.

From these two methods of estimating distances to the dust slabs, the results are in perfect agreement. Since the results rely on very different strategies this strongly supports their validity.

Another quantity found from the $counts/pc$ versus $distance(pc)$ profile, was the FWHM. From the PN data the inner halo peak had a width of 224 ± 16pc and the outer halo peak had a width of 78 ± 10pc. From

the MOS data the inner peak value was 218 ± 16pc while the outer
was 70 ± 8pc. These values are compatible with the width expected
from the point spread function alone, implying that the two dust slabs
are probably two thin sheets of dust placed at ≈ 870pc and ≈ 1400pc.
The values for the FWHM derived from the two cameras are in perfect
agreement, although they only need to be in slight agreement, since
the MOS and the PN respectively have slightly different point spread
functions.

The last important parameter found from the *counts/pc* versus
distance(pc) profile was the integrated Lorentzians. For the PN data
the integrated Lorentzian for the inner peak was 1837 ± 156 counts and
for the outer peak, 819 ± 118 counts. For the MOS data the value for
the inner peak is 1857 ± 159 counts while the value for the outer is
930 ± 120. These values clearly show that the results derived are valid
and that the peaks are significant enough to assume the presence of
dust slabs at the above mentioned distances.

From the spectra extracted from the PN and MOS2 data, the ab-
sorbing column, n_H, was found. First fitted independently, the halo
and afterglow spectra from the PN data yielded $9.1^{+1.2}_{-1.1} \cdot 10^{21} \, \mathrm{cm}^{-2}$ and
$7.8^{+0.9}_{-1.1} \cdot 10^{21} \, \mathrm{cm}^{-2}$ respectively. For the MOS2 data the values were
$9.8^{+2.1}_{-1.3} \cdot 10^{21} \, \mathrm{cm}^{-2}$ and $8.5^{+1.4}_{-1.2} \cdot 10^{21} \, \mathrm{cm}^{-2}$ for the halo and afterglow re-
spectively. The values agree between halo and afterglow spectra within
uncertainties and support the notion that the halo emission and the
afterglow emission should originally come from the same source, mean-
ing that they travelled through the same space. This means that the
halo light must have been caused by scattering, as expected.

The absorbing column derived from the common fit of the halo and
afterglow emission was $7.8^{+0.6}_{-0.5} \cdot 10^{21} \, \mathrm{cm}^{-2}$ for the PN data and $9.1^{+1.1}_{-0.9} \cdot$
$10^{21} \, \mathrm{cm}^{-2}$ for the MOS2 data. The values agree for the two data sets
and are significantly above the galactic value ($\approx 6 \cdot 10^{21} \, \mathrm{cm}^{-2}$). The
residual, of $\approx 2 - 3 \cdot 10^{21} \, \mathrm{cm}^{-2}$, can be assumed to be contributed by

the host galaxy of the GRB, since it is not very likely that the photons have encountered dust in intergalactic space.[25]

From the common fit of the halo and afterglow spectra, photon indices were also found. From the PN data; for the halo the derived photon index was $2.96^{+0.18}_{-0.16}$ and the for the afterglow the photon index was $1.85^{+0.12}_{-0.09}$. From the MOS2 data; for the halo the derived photon index was $3.3^{+0.3}_{-0.2}$ and the afterglow the photon index was $2.03^{+0.17}_{-0.08}$. The photon indices from the two data sets agree and show that the halo emission has a spectrum significantly steeper than the afterglow. This supports the idea that the halo emission could be light from the afterglow scattered by dust, since this type of scattered light is expected to have a steeper spectrum than the original emission, as explained in Section 2.3.4.

In all, through this study, I have found results firmly substantiating the claim that the X-ray halo around GRB 031203 should be scattered light from the afterglow, and that this scattering is caused by two thin sheets of dust placed at $\approx$ 1400pc and $\approx$ 870pc.

With more analyses, like this, of other GRB afterglow halo phenomena, the dust in our Galaxy can be efficiently mapped.

4.4. Extensions of the Analysis

There are still more to explore in the subject treated in this thesis. An extension of my analysis could be done in modelling the dust to find a grain size, as explained in Section 2.3.5.

My fellow master thesis student, Mike Alexandersen, has been performing a survey on GRB afterglows observed by Swift, searching for traces of halos around them. I was planning on performing a quick analysis on one of the potential halos that he found. Unfortunately, of the 10 potential dust scattered halos he found, none where observed by

---

[25] This is because the dust formation process is believed to take place in stellar winds or SNe; i.e. in galaxies.

XMM. Since this is the telescope supplying the data that my analysis methods are based on, a quick analysis could not be done.

Through my analysis I have discovered what a valuable tool these X-ray halos around GRB afterglows are. They reveal information which is otherwise unobtainable to us. Generally it would be of great advantage, to those interested in investigating the dust in our Galaxy, if there were XMM data on more GRB afterglows, since XMM data has adequate resolution capabilities to make thorough analysis of the afterglow halos. More GRB observations would increase the likelihood of stumbling upon the traces of halos. Right now there only exist two XMM data sets known to have traces of halos. A good strategy would be to quickly analyse the data products each time the Swift telescope observes a GRB, and if traces of a halo seem to be present, an XMM observation of the afterglow should immediately be started.

5. Bibliography

References

Astronomyonline. 2009, `http://astronomyonline.org/Stars/SupernovaRemnant.asp?Cate=Stars&SubCate=ST04&SubCate2=SupernovaRemnant`

Attwood, D. 2007, Soft X-Ray And Extreme Ultraviolet Radiation - Principles And Applications (Cambridge University Press)

Chandra's home page. 2009, `http://chandra.harvard.edu/xray_astro/absorption.html`

COSMOS. 2009, COSMOS - The SAO Encyclopedia of Astronomy, `http://astronomy.swin.edu.au/cms/astro/cosmos/S/Spiral+Galaxy+Formation`

G. W. Fraser. 1989, X-ray detectors in astronomy (Cambridge Astrophysics Series)

Greiner, J., Voges, W., Boller, T., & Hartmann, D. 1999, A&AS, 138, 441

Guenther, R. D. 1990, Modern Optics (Wiley)

Hjorth, J., Andersen, A., Fynbo, J. P. U., et al. 2005, Naturens Verden, 55

Mauche, C. W. & Gorenstein, P. 1986, ApJ, 302, 371

Mészáros, P. 2002, ARA&A, 40, 137

Moretti, A., Margutti, R., Pasotti, F., et al. 2008, A&A, 478, 409

NASA. 2008, HEASoft, `http://heasarc.nasa.gov/lheasoft/`

NASA. 2009, `http://imagine.gsfc.nasa.gov/docs/science/how_l2/xray_generation_el.html`

NASA's home page. 2009a, `http://www.nasa.gov/centers/marshall/multimedia/photogallery/photos/photogallery/chandra/chandra5test.html`

NASA's home page. 2009b, `http://heasarc.gsfc.nasa.gov/docs/xmm/about_satellite.html`

Newscientist. 2009, `http://www.newscientist.com/articleimages/dn12238/0-sharpest-infrared-sky-map-takes-galaxy-census.html`

Piran, T. 2004, Reviews of Modern Physics, 76, 1143

SIMBAD. 2009, `http://simbad.u-strasbg.fr/simbad/`

Tanvir, N., Levan, A., Wiersema, K., et al. 2009, GRB Coordinates Network, 9219, 1

The XMM Home Page. 2009, `http://xmm.esac.esa.int/external/xmm_user_support/documentation/technical/`

The XMM-Newton ABC Guide. 2008, An Introduction to XMM-Newton Data Analysis, `ftp://legacy.gsfc.nasa.gov/xmm/doc/xmm_abc_guide.pdf`

Tiengo, A. & Mereghetti, S. 2006, A&A, 449, 203

Tinney, C., Stathakis, R., Cannon, R., & Galama, T. 1998, IAU Circ., 6896, 3

van Paradijs, J., Kouveliotou, C., & Wijers, R. A. M. J. 2000, ARA&A, 38, 379

van Paradijs, J. and Bleeker, J. A. M. 1999, X-Ray Spectroscopy in Astrophysics (Springer)

Vaughan, S., Willingale, R., O'Brien, P. T., et al. 2004, ApJ, 603, L5

Vaughan, S., Willingale, R., Romano, P., et al. 2006, ApJ, 639, 323

Vianello, G., Tiengo, A., & Mereghetti, S. 2007, A&A, 473, 423

Watson, D., Vaughan, S. A., Willingale, R., et al. 2006, ApJ, 636, 967

Whittet, D. C. B. 1992, Dust In The Galactic Environment (Institute of Physics Publishing)

XMM-Newton Users' Handbook. 2003, `http://xmm.esac.esa.int/external/xmm_user_support/documentation/uhb_2.1/index.html`

Appendix A: My IDL code

A.1. nyevent

```
f = 'pn_time10.txt'    ; input table
readcol,f,nr,x,y

x=x*0.05          ;omregnes til buesekunder
y=y*0.05          ;omregnes til buesekunder


r=sqrt((x-1302.2810)^2+(y-1183.210)^2)


;Bin str: 4", men der er en bin for hvert 1",

rplace=fltarr(310)      ;mean af r værdier der kommer i hver bin
counts=fltarr(310)      ;counts i hver bin

;1" afstand mellem bins: i=0,310-1 do begin
for i=0,310-1 do begin
j=(where(r gt 40+(i/1.) and r lt 44+(i/1.),count))
if j ne [-1] then rplace(i)=MEAN(r(j)) else rplace(i)=42+(i/1.)
counts(i)=count
endfor

;beregn baggrund
g = 'pn_bkg.txt'    ; input table
readcol,g,n,u,v

u=u*0.05          ;omregnes til buesekunder
v=v*0.05          ;omregnes til buesekunder
```

```
b=sqrt((u−1302.2810)^2+(v−1183.210)^2)



bplace=fltarr(50)      ;mean af r værdier der kommer i hver bin
bcounts=fltarr(50)     ;counts i hver bin



for i=0,50−1 do begin
j=(where(b gt 350+i and b lt 354+i,count))
if j ne [−1] then bplace(i)=MEAN(b(j))else bplace=352+i
bcounts(i)=count
endfor

;fitting background
M=1
A=[0.5]
result=curvefit(bplace, bcounts, sqrt(bcounts), A$
, function_name='linear', /noderivative)


print, result, A

hcounts=counts−rplace∗(A(0)/10)

device, set_font='12x24'
window, xsize=1200, ysize=700
;plot, bplace, bcounts
plot, rplace, hcounts, yrange=[0,60], /ystyle$
, title='PN Data− Time Interval 10', xtitle='!4h!3 (arcsec)'$
, ytitle='F(!4h!3) (counts)', background='ffffff'x, col=0


C=0
D=0
E=0
F=0

read, "expected interval for first halo peak?", C, D
read, "expected interval for second halo peak?", E, F

m1=rplace(where(hcounts eq max(hcounts(where(rplace$
 ge C and rplace le D)))))
m2=rplace(where(hcounts eq max(hcounts(where(rplace$
 ge E and rplace le F)))))

print, 'first halo peak value=', max(hcounts(where(rplace$
 ge C and rplace le D)))
print, 'first halo peak place=', m1
```

```
print , 'second halo peak value=', max(hcounts(where(rplace$
 ge E and rplace le F)))
print , 'second halo peak place=', m2

oplot , [m1,m1],[0,70],col=255
oplot , [m2,m2],[0,70],col=255
oplot , rplace , hcounts , col=0
write_png , "pn10_plot.png", tvrd(/true)
end
```

A.2. linear

```
;FUNCTION linear , x, a
;F=a(0)*x
;RETURN, F

PRO linear , x, a, f
F=a(0)*x

end
```

A.3. haloexpansion

```
f = 'pn_halopeaks.txt'    ; input table
readcol ,f ,nr ,time ,max1 ,halo1 ,error1 ,max2 ,halo2 ,error2

errorx=make_array(10,value=2890.)

weights1=1./(error1^2)
weights2=1./(error2^2)

A=[0.5 ,1.]
result=curvefit(time , halo1 , weights1 , A, sigma1 ,$
 function_name='powerlaw', /noderivative)

B=[0.5 ,1.]
result=curvefit(time , halo2 , weights2 , B, sigma2 ,$
 function_name='powerlaw', /noderivative)

print , 'halo1 parameters=', A
print , 'error=', sigma1
print , 'halo2 parameters=', B
print , 'error=', sigma2

t=findgen(1000)*90
```

```
p1=a(1)*(t))^a(0)
p2=b(1)*(t)^b(0)

ploterror, time, halo1, errorx, error1, yrange=[0,300]$
, xrange=[0,8.*(10^4.)], /xstyle, psym=3, title=$
'PN Data- Expansion of Halo', xtitle='Time since burst (s)'$
, ytitle='!4h!3 (arcsec)', background='ffffff'x, col=0$
, errcol=255

oploterror, time, halo2, errorx, error2, psym=3, col=0$
, errcol='ff0000'x
oplot, t, p1, col=0
oplot, t, p2, col=0
write_png, "pn_haloexpansion_t0_free.png", tvrd(/true)


end
```

A.4. powerlaw

```
pro powerlaw, t, a, f
F=a(1)*(t-a(2))^a(0)
end
```

A.5. distcount

```
f='pn_4filt_distsort.txt'
readcol,f,nr,d


ncountpbin=100.                             ;counts pr bin
countsppc=dblarr(floor(max(nr)/ncountpbin)) ;array counts pr pc
distbin=dblarr(floor(max(nr)/ncountpbin))   ;array mean dist for bin
binstart=dblarr(floor(max(nr)/ncountpbin))  ;starten af bin på 100
binstop=dblarr(floor(max(nr)/ncountpbin))   ;slutning af bin på 100
binsize=dblarr(floor(max(nr)/ncountpbin))   ;størrelse af hver bin
error=dblarr(floor(max(nr)/ncountpbin))     ;standard afv. på pkt

FOR j=0,floor(max(nr)/ncountpbin)-1 DO BEGIN
;løkke, 0 til max antal bins ca. 551
jj=j*ncountpbin
;jj defineres, er nr event i rækken
binstart(j)=d(1+jj) & binstop(j)=d(ncountpbin+jj) ;regner hvor bin start og slut
distbin(j)=MEAN(d(1+jj:ncountpbin+jj))
;regner mean dist er for bin
countsppc(j)=ncountpbin/(d(ncountpbin+jj)-d(1+jj));regner antal counts pr. pc
binsize(j)=binstop(j)-binstart(j)
;regner st¿rrelse af bin
```

```
error(j)=sqrt(100)/binsize(j)                          ;regner errorbars

ENDFOR


distbin2=distbin(WHERE(distbin GE 200. and distbin le 5000))
countsppc2=countsppc(WHERE(distbin GE 200. and distbin le 5000))
error2=error(WHERE(distbin GE 200. and distbin le 5000))

;plotter på logaritmisk skala
ploterror, distbin, countsppc, error, psym=1, XRANGE=[200,5000],$
 /XSTYLE, /XLOG, /YLOG, XTITLE='Distance (pc)', YTITLE='Counts/pc', /nohat



WEIGHTS=1.0/(error2^2)

B=[600000.,-1.77,10.,40.,870.,5.,15.,1384.]



countfit=CURVEFIT(distbin2, countsppc2, WEIGHTS, B, SIGMA, CHISQ=chi$
, /DOUBLE, FUNCTION_NAME='lofunct', ITMAX=1000, /noderivativ, TOL=0.000000001)

;countfit=SVDFIT(distbin2, countsppc2, A=B, CHISQ=chi, /DOUBLE, FUNCTION_NAME$
='pn_lofunct', SIGMA=sig, TOL=0.000000001)


PRINT, 'Function parameters: ', B, 'chi squared=', chi, 'errors:', SIGMA

ploterror, distbin2, countsppc2, error2, /XLOG, /YLOG, xrange=[200,5000]$
, /xstyle, yrange=[0.1,100], /ystyle, psym=4, /nohat, XTITLE='Distance (pc)'$
, YTITLE='Counts/pc', title='PN Data', background='ffffff'x, col=0$
, errcol=255, symsize=0.4

oplot, distbin2, countfit, col=0
write_png, "pn_4dist_vs_count.png", tvrd(/true)
print, 'number of point used in fitting=', n_elements(distbin2)


End
```

A.6. lofunct

```
PRO lofunct, X, B, F

;the powerlaw and two physics type lorentz functions

F=B[0]*X^B[1]+(B[2]*B[3]^2/((X-B[4])^2+B[3]^2))+$
```

(B[5]*B[6]^2/((X–B[7])^2+B[6]^2))

;parameters: 1=powerlaw–index, 2=5=hight–of–peak/intensity
; 3=6=hwhm, 4=7=location

END

	Dist 1 (pc)	Dist 2 (pc)
MOS		
t_0 locked	1919	929
	±1280	±360
t_0 and α locked	1414	872
	±26	±11
PN		
t_0 locked	1959	1173
	±1467	±722
t_0 and α locked	1416	886
	±23	±16

Table B.1. Distances to the dust slabs responsible fro the inner (Dist 1) and outer (Dist 2) halo respectably. Derived from the fitted proportionality constants displayed in table 3

Appendix B: photometry
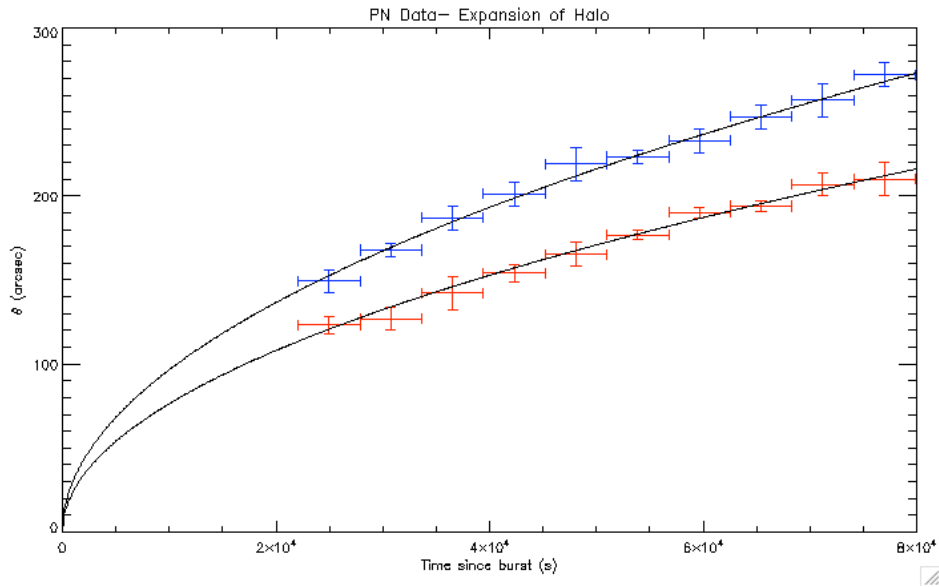
Figure B.1. Plot from the filtered PN data (pattern values up to 12 and flag=0) covering the energy range 1keV to 2.5 keV, showing the evolution of the halos as a function of time, with the fitted power-law profile. Here the parameter α was kept locked to 0.5, and t_0 locked to 0 (see Table 3 for fitted parameters). The plot is produce by the IDL procedure shown in Appendix A.3.
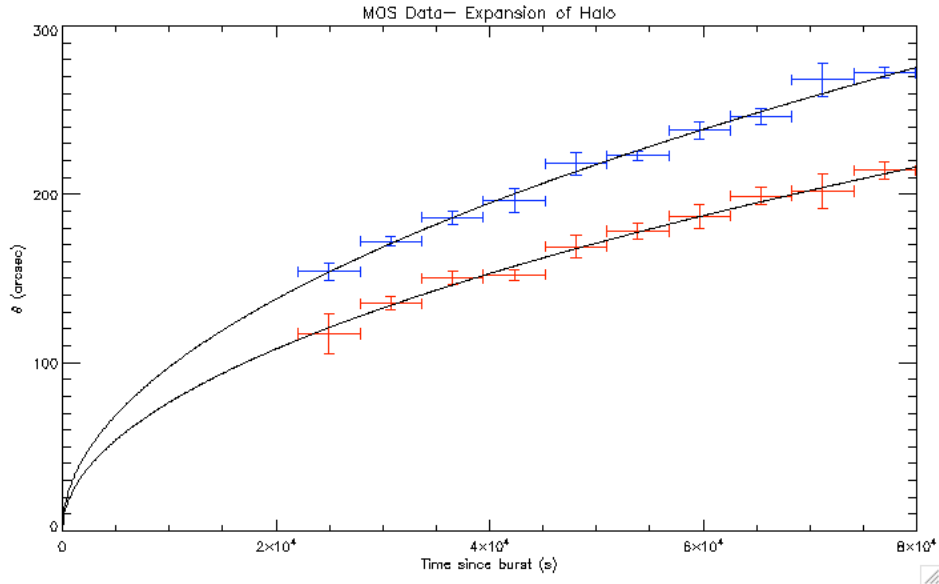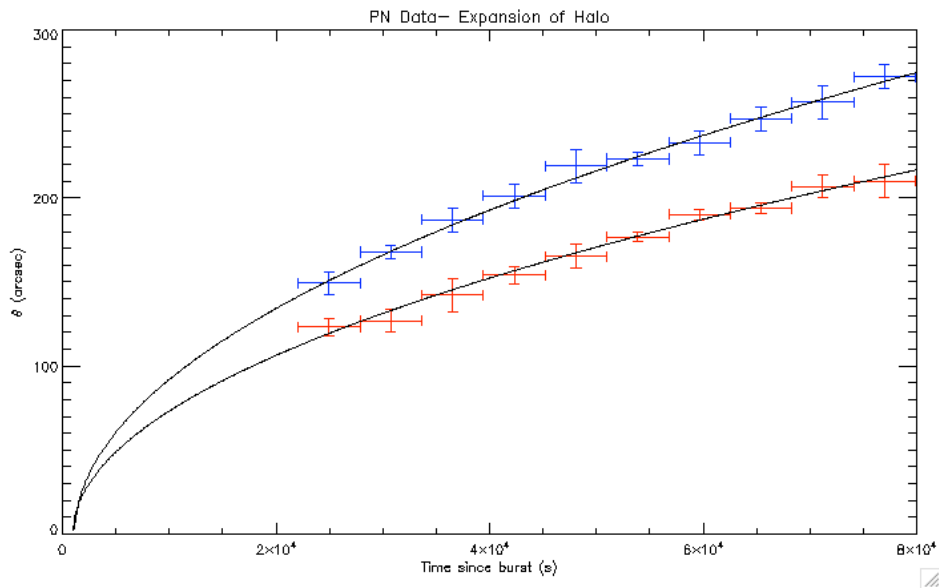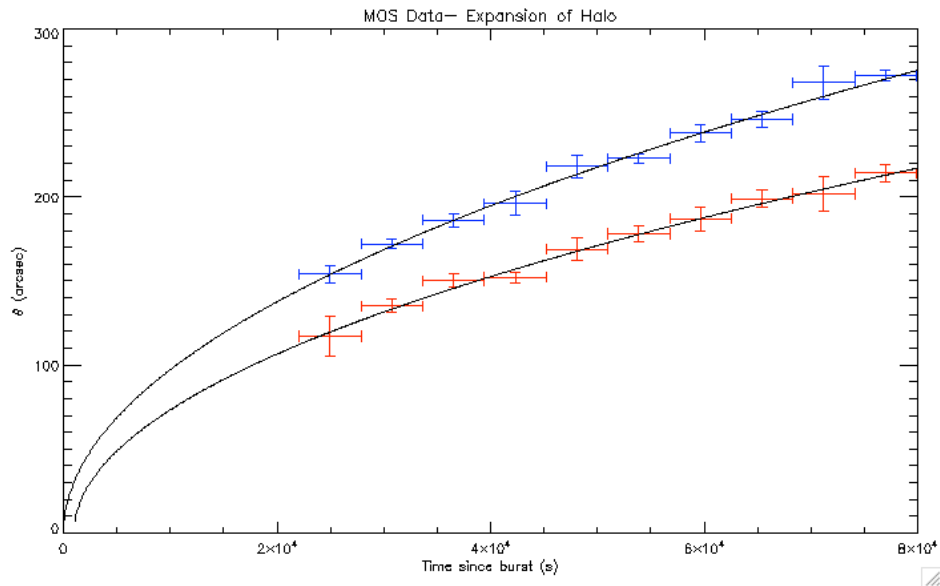
Figure B.2. Plot from the filtered and merged MOS1 and 2 data (pattern values up to 12 and flag=0) covering the energy range 1keV to 2.5 keV, showing the evolution of the halos as a function of time,with the fitted power-law profile. Here the parameter α was kept locked to 0.5 and t_0 locked to 0 (see Table 3 for fitted parameters). The plot is produce by the IDL procedure shown in Appendix A.3.

Figure B.3. Plot from the filtered PN data (pattern values up to 12 and flag=0) covering the energy range 1keV to 2.5 keV, showing the evolution of the halos as a function of time, with the fitted power-law profile. Here the parameter α was kept locked to 0.5 and t_0 was kept free (see Table 3 for fitted parameters). The plot is produce by the IDL procedure shown in Appendix A.3.

Figure B.4. Plot from the filtered and merged MOS1 and 2 data (pattern values up to 12 and flag=0) covering the energy range 1keV to 2.5 keV, showing the evolution of the halos as a function of time, with the fitted power-law profile. Here the parameter α was kept locked to 0.5 and t_0 was kept free (see Table 3 for fitted parameters). The plot is produce by the IDL procedure shown in Appendix A.3.
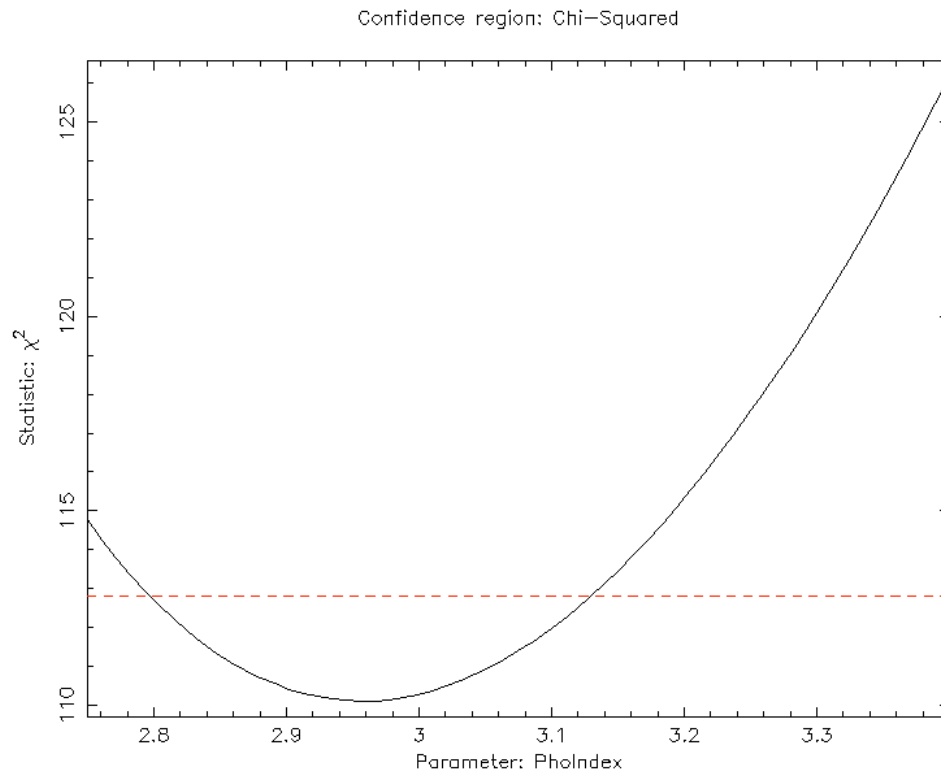
Appendix C: Spectroscopy
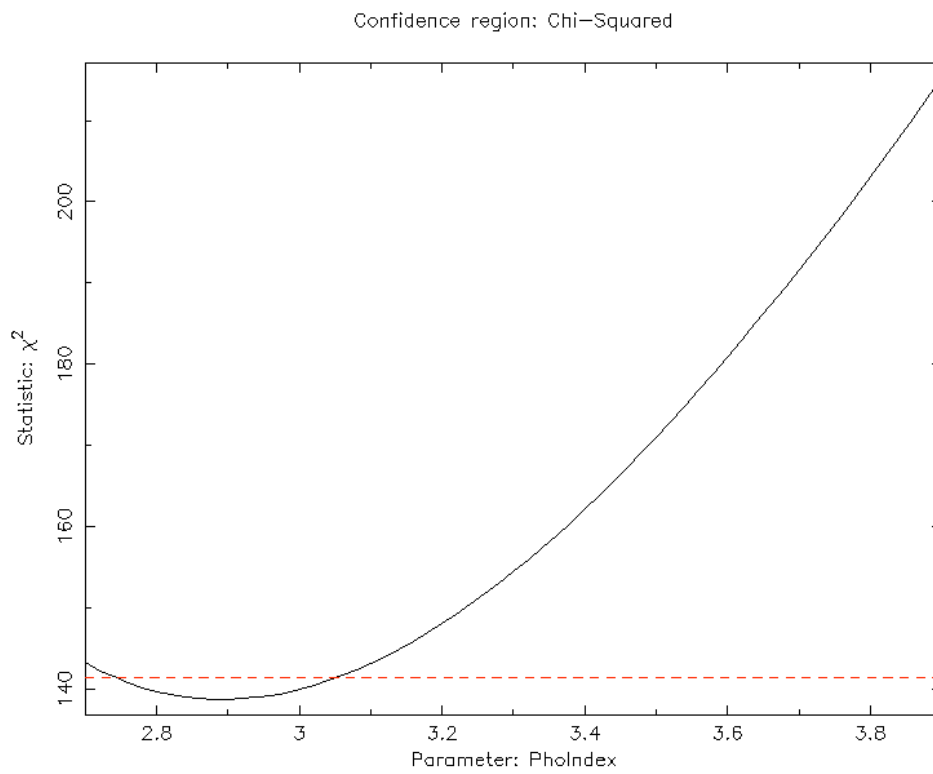
Confidence region: Chi—Squared

Figure C.1. Plot of chi-squared versus the photon index of the halo spectrum (derived from the simultaneous fit of halo and afterglow) from the PN data, collecting afterglow counts from an annulus of 15"-4". The plot shows that there are no inconsistencies for the fitted parameter value.

Figure C.2. Plot of chi-squared versus the photon index of the halo spectrum (derived from the simultaneous fit of halo and afterglow) from the PN data, collecting afterglow counts from an annulus of 30"-4". The plot shows that there are no inconsistencies for the fitted parameter value.
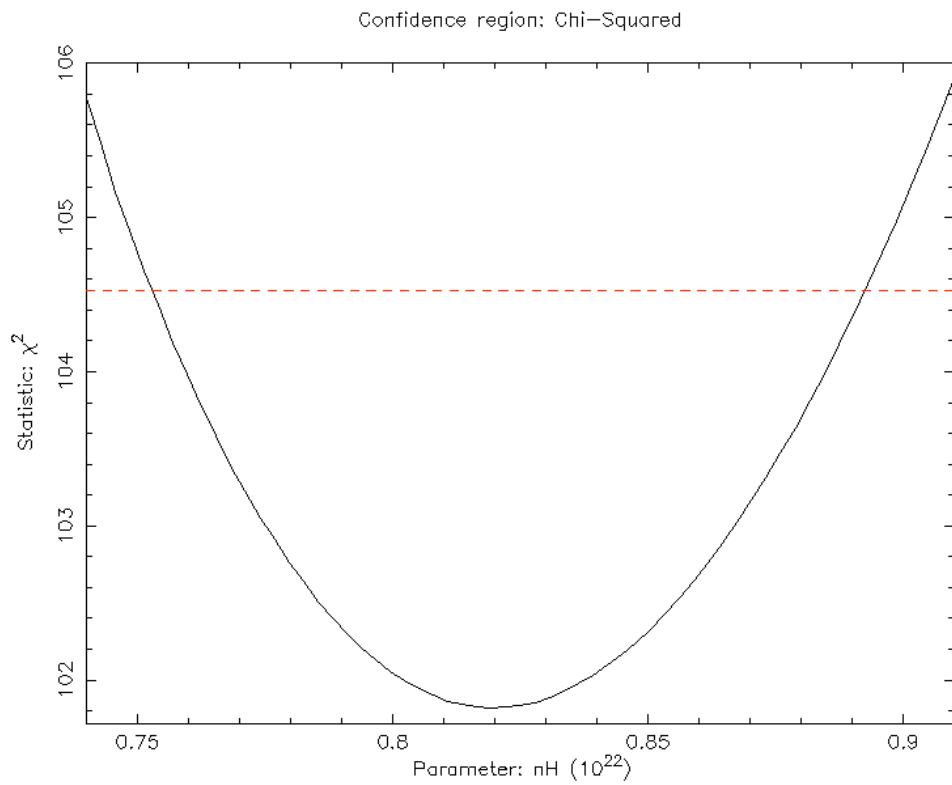
Figure C.3. Plot of chi-squared versus the absorbing column of the halo fitted simultaneously with the afterglow from an annulus of 30"-4", using only pattern 0 events. The plot shows that there are no inconsistencies for the fitted parameter value.